



Hochschule für Angewandte Wissenschaften Hamburg
Hamburg University of Applied Sciences

Diploma Thesis

Department of Automotive and Aeronautical Engineering

Flight test planning and data extraction

Stefan Velikov

September 17, 2008



Hochschule für Angewandte Wissenschaften Hamburg
Fakultät Technik und Informatik
Department Fahrzeugtechnik + Flugzeugbau
Berliner Tor 9
20099 Hamburg

in collaboration with:

Linköping University
Department of Mechanical Engineering
Linköping
Sweden

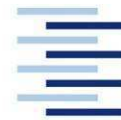
Author: Stefan Velikov
Date: 17.09.2008

1. Examiner: Prof. Dr.-Ing. Dieter Scholz, MSME
2. Examiner: Prof. Dr.-Ing. Hartmut Zingel

Supervisors: Dr. Christopher Jouannet
David Lundström

Abstract

A dynamically scaled model of a business jet design, the *Raven*, has been built at the Linköping University to investigate the possibilities of flight testing with subscale radio controlled aircraft models within a low-budget university project. This work comprises a theoretical approach of flight test planning and post-flight data handling to identify the aircraft's aerodynamic performance and dynamic behaviour. Calibration methods for pressure sensors are also presented with an emphasis on in-flight test procedures to determine position error and their corresponding data reduction. For drag predictions a basic thrust model of *Raven*'s engines is included, which consists of linear scaling of available thrust data. Its accuracy is however questionable and is to be further verified. Since determination of aerodynamic performance has high priority during the first tests, main part of this work deals with flight test procedures to determine lift and drag coefficients as a function of angle of attack from a steady level flight and series of steady glides. The corresponding data reduction sequences are adjusted in accordance with the available instrumentation of the *Raven*. In addition, techniques to investigate aircraft longitudinal and lateral-directional static stability from flight testing are presented with data reduction methods to identify important parameters like neutral point position, pitching moment coefficient and side-force stability derivatives. Furthermore, flight test methods to determine characteristic dynamic stability parameters like damping ratio and frequency for the individual modes of motion are given. This includes various piloting techniques and post-flight results evaluation.



Flight test planning and data extraction

Task definition of *Diplomarbeit* at HAW Hamburg

Background

A research project on subscale flight testing is being carried out at the Linköping University. The project is exploring the possibilities of using radio controlled scale models for aerodynamic evaluation and in particular for studying dynamic effects that can not be measured in a wind tunnel. For this purpose the *Raven*, a dynamically scaled model of a business jet design, has been built by the Department of Mechanical Engineering and is scheduled for flight testing during 2008.

Objective

The thesis work consists of planning the flight tests with the *Raven* aircraft and preparing the data extraction methods. In particular, the objective is to decide how to perform the test flights in order to identify essential aerodynamic and flight mechanical parameters. For each parameter a particular flight test technique shall be chosen and means to extract the useful data shall be prepared. This may imply that for some parameters accurate models of the aircraft or components of the aircraft, for example a thrust model of the turbine, need to be derived. Since during flight testing a huge amount of data is recorded, data reduction may be necessary. MATLAB has to be used for data reduction. Task breakdown:

- Investigation of various calibration methods for flight instruments and suggestions of their application in the *Raven* aircraft flight testing by taking into account available instrumentation.
- Determination of a suitable thrust model of the aircraft's turbines giving the thrust as a function of velocity for different altitudes and engine speeds.
- Selection of the appropriate flight test techniques to obtain lift, drag and pitching moment coefficients as a function of angle of attack. Furthermore, the static stability of the test aircraft shall be investigated.
- Selection of the appropriate flight test techniques to obtain side force coefficients as a function of sideslip angle.
- Selection of the appropriate flight test techniques to investigate the dynamic stability of the aircraft. Methods to obtain frequency and damping terms for short period, Dutch roll, spiral and roll mode from flight test data shall be presented.
- The candidate shall prepare MATLAB code for data handling and flight test evaluation.

The results have to be documented in a report. The report has to be written in a form up to internationally excepted scientific standards. The application of the German DIN standards is one excepted method to achieve the required scientific format.



The thesis is prepared at Linköping University, Department of Mechanical Engineering. Supervisors are Dr. Christopher Jouannet and PhD student David Lundström.

Declaration

I declare that this diploma thesis is entirely my work. Where use has been made of the work of others, it has been fully acknowledged and referenced.

.....

Date

Signature

Contents

	Page
List of figures	9
List of tables	11
Nomenclature	12
List of abbreviations.....	15
1 Introduction	16
1.1 Motivation.....	16
1.2 Objectives.....	16
1.3 Report structure.....	17
2 Aircraft data and properties	19
3 Theoretical background	23
3.1 Overview of flight testing	23
3.1.1 Purpose and types of flight tests	23
3.1.2 Flight test planning.....	24
3.2 International Standard Atmosphere	26
3.3 Pitot-static systems.....	29
3.4 Basic flight theory	34
3.4.1 Aerodynamic forces	34
3.4.2 Drag polar	39
3.4.3 Performance equations	42
4 Calibration methods	44
4.1 Calibration of temperature sensors	44
4.2 Instrument calibration of pressure sensors.....	46
4.3 Position error calibration methods	48
4.3.1 Background	48
4.3.2 Speed course method	50
4.3.3 GPS techniques	53
4.3.4 Calibration using GPS altitude data.....	54
4.3.5 Other commonly used methods.....	56
4.4 Calibration of vanes	57
5 Turbine thrust model and performance	59
6 Flight test methods to determine aerodynamic performance and static stability	67
6.1 Lift and drag determination.....	67

6.1.1	Steady level flight	67
6.1.2	Drag polar determination from a steady glide	70
6.1.3	Stall speed and maximum lift coefficient	81
6.2	Longitudinal static stability.....	85
6.2.1	Trim equation and static margin	86
6.2.2	Neutral point determination from flight tests.....	89
6.3	Lateral-directional static stability.....	93
6.3.1	Governing equations	94
6.3.2	Steady heading sideslip test procedure and data reduction.....	97
7	Dynamic stability flight tests	102
7.1	Longitudinal dynamic stability	103
7.1.1	Short period mode	104
7.1.2	Phugoid mode	108
7.2	Lateral-directional dynamic stability	112
7.2.1	Spiral mode	113
7.2.2	Dutch roll mode	115
7.2.3	Roll mode.....	118
7.2.4	Lateral-directional stability data reduction	119
8	Summary	122
	References	125
	Appendix A Charts and tables.....	127
	Appendix B Altitude and airspeed position error.....	130
	Appendix C FS-70 Typhoon manufacturer data	133
	Appendix D Example of total thrust calculation	135

List of figures

	Page
Fig. 2.1	<i>Raven</i> – a subscale business jet demonstrator 19
Fig. 3.1	Pressure measurement with a Pitot-static system..... 30
Fig. 3.2	Typical aircraft lift and drag functions with angle of attack 37
Fig. 3.3	Parabolic drag polar 40
Fig. 3.4	Variation of C_D with C_L for a typical aircraft configuration..... 41
Fig. 3.5	Forces acting on an aircraft in a straight, symmetric flight..... 42
Fig. 4.1	Pressure measurement in a U-shaped tube 46
Fig. 4.2	Speed course geometry..... 51
Fig. 4.3	Cloverleaf technique geometry / Ground speed relationships 53
Fig. 4.4	Pitot tube with vanes for α and β measurement 57
Fig. 5.1	FS-70 gas turbine for propulsion of remote controlled aircraft 59
Fig. 5.2	Static thrust versus engine speed – polynomial approximation 61
Fig. 5.3	Total thrust as a function of airspeed, altitude and engine speed..... 65
Fig. 6.1	Forces acting on an aircraft in a steady level flight..... 68
Fig. 6.2	Steady glide illustration (Sawtooth climb segment) 72
Fig. 6.3	Changes of altitude for measured ambient pressure difference 77
Fig. 6.4	$C_{M, c.g.}$ versus C_L for different centre of gravity positions..... 87
Fig. 6.5	Elevator angle to trim versus C_L for different centre of gravity positions 90
Fig. 6.6	Elevator angle to trim versus C_L for two CG positions flown 91
Fig. 6.7	Slope of elevator angle to trim with C_L plotted versus CG position..... 93
Fig. 6.8	Aircraft body axes system and standard sign convention 94
Fig. 6.9	Geometry of steady, straight sideslip at two different CG positions 99
Fig. 7.1	Types of control inputs for dynamic stability flight tests..... 103
Fig. 7.2	Qualitative example of Maximum Slope method for data reduction 106
Fig. 7.3	Chart for determining damping ratio and natural frequency 107
Fig. 7.4	Qualitative illustration of a damped phugoid oscillation 109
Fig. 7.5	Plot of measured and calculated airspeed versus time in a phugoid mode 112
Fig. 7.6	Aircraft behaviour in a spiral mode..... 113
Fig. 7.7	Example of spiral mode measured data and mathematical approximation..... 115
Fig. 7.8	Dutch roll oscillation 116
Fig. 7.9	Restoring rolling moment in a roll mode 118
Fig. A.1	Compressibility correction factor 128
Fig. A.2	Atmospheric temperature measurement 129

Fig. B.1	Ratio of altitude to airspeed position error correction.....	132
Fig. C.1	FS-70 Typhoon static thrust versus engine speed at MSL.....	133
Fig. C.2	FS-70 Typhoon – three-view drawing and main parameters	134

List of tables

	Page
Table 2.1 <i>Raven</i> demonstrator – technical data and specifications	21
Table 3.1 Risk Code Matrix	25
Table 4.1 Speed course data reduction sequence	52
Table 5.1 Engine specifications for FS-70 Typhoon and Olympus HP	60
Table 5.2 Engine speed and static thrust for one and both engines.....	61
Table 5.3 Total thrust variation with V and n for standard conditions at MSL.....	62
Table 5.4 Total thrust variation with V and n for standard conditions at 10 000 ft.....	63
Table 5.5 Total thrust variation with V and n for standard conditions at 16 000 ft.....	64
Table 6.1 Steady glide data reduction sequence.....	80
Table 7.1 Example data for measured and calculated airspeed.....	111
Table 7.2 <i>Solver</i> results for phugoid characteristics and parameters	111
Table 7.3 Example bank angle variation with time in a spiral mode	114
Table A.1 International Standard Atmosphere values.....	127
Table C.1 FS-70 Typhoon static thrust and engine speed.....	133
Table D.1 Total thrust values for an example engine speed of 75 %	135
Table D.2 Equations relating airspeed and total thrust at 75 % engine speed	136

Nomenclature

a	speed of sound
A	aspect ratio
a_x	acceleration along the aircraft's longitudinal axis
b	wing span
c	chord length
\bar{c}	wing mean aerodynamic chord
C_D	drag coefficient
C_{D_0}	drag coefficient at zero lift
C_L	lift coefficient
$C_{\mathcal{L}}, C_M, C_N$	rolling / pitching / yawing moment coefficient
C_{N_R}	yaw rate damping coefficient
C_Y	side force coefficient
D	drag
e	Oswald efficiency factor / base of the natural logarithm
E	lift-to-drag ratio
F_A	resultant aerodynamic force
F_T	thrust
g	acceleration due to gravity
h	geometric altitude
h_p	pressure altitude
H	geopotential altitude
H_{airfield}	airfield elevation from mean sea level
H_{GPS}	altitude data from the global positioning system
H_{MSL}	altitude above mean sea level
I_{xx}, I_{yy}, I_{zz}	moment of inertia in roll / pitch / yaw
K	constant in lateral-directional dynamic stability data evaluation
K_N	static margin
k_{rec}	temperature recovery factor
L	lift
\mathcal{L}, M, N	rolling / pitching / yawing moment
l	length / distance
m	mass
Ma	Mach number
n	engine speed in percentage of the maximum available speed
p	static pressure
P	roll rate

p_T	total pressure
q_c	impact pressure
R	specific gas constant
Re	Reynolds number
ROD	rate of descent
S	area
SF	scale factor
t	time
t_{double}	time-to-double
T	static temperature
T_P	period
T_T	total temperature
V	true airspeed
\bar{V}	tail volume coefficient
V_C	calibrated airspeed
V_E	equivalent airspeed
V_G	ground speed
V_S	stall speed
W	weight
x, y, z	coordinates along the aircraft's body axes

Greek symbols

α	angle of attack
β	angle of sideslip
δ	relative pressure
$\delta_a, \delta_e, \delta_r$	aileron / elevator / rudder deflection
γ	flight path angle
Δh_{pc}	altitude static position error correction
Δp_{ic}	static pressure instrument error correction
Δp_p	static position error
$\Delta p_{T,ic}$	total pressure instrument error correction
ΔT_{ISA}	temperature deviation from standard day conditions at mean sea level
ΔV_{pc}	airspeed static position error correction
$\Delta \vartheta_{ic}$	temperature instrument error correction in °C
θ	relative temperature
θ_E	pitch attitude
ϑ	temperature in °C

κ	isentropic exponent
λ	damping ratio
Λ	temperature lapse rate
μ	dynamic viscosity
ρ	density
σ	relative density
τ	time constant
ϕ	bank angle
ψ	heading, yaw angle
ψ_{phase}	phase angle
ω_d	damped frequency
ω_n	undamped natural frequency

Subscript

∞	free-stream flow
0	Standard Atmosphere values at mean sea level, except for C_{D_0}
<i>a.c.</i>	aerodynamic centre
acc	corrected for occurring acceleration
avg	average
<i>c.g.</i>	centre of gravity
cor	completely corrected test data
<i>i</i>	indicated
<i>ic</i>	instrument calibrated
max	maximum value
<i>MTOW</i>	at maximum take-off weight
<i>N</i>	neutral point
<i>p, sp</i>	phugoid / short period mode
<i>r, s, Dr</i>	roll / spiral / Dutch roll mode
ref	reference
stat	static
std	standard day conditions
<i>t</i>	test day conditions
tail	tailplane
temp	corrected for non-standard temperature variations
trim	at trimmed condition
<i>v</i>	vertical tail
β	due to sideslip
$\delta_a, \delta_e, \delta_r$	due to aileron / elevator / rudder deflection

List of abbreviations

AC	aerodynamic centre
AOA	angle of attack
ASI	airspeed indicator
CAD	Computer Aided Design
CG	centre of gravity
CPU	Central Processing Unit
DGPS	Differential Global Positioning System
FAA	Federal Aviation Administration
FAR	Federal Aviation Regulations
GPS	Global Positioning System
ICAO	International Civil Aviation Organization
ISA	International Standard Atmosphere
ISO	International Organization for Standardization
JAR	Joint Aviation Requirements
MAC	mean aerodynamic chord
MS	Microsoft
MSL	mean sea level
MTOW	maximum take-off weight
NACA	National Advisory Committee for Aeronautics
QNH	actual pressure at mean sea level
RAM	Random Access Memory
RPM	revolutions per minute
SI	International System of Units
TCU	Turbine Control Unit
TPR	Transient Peak Ratio
UAV	Unmanned Aerial Vehicle

1 Introduction

1.1 Motivation

Flight testing is a fundamental process during the detail design phase of an aircraft providing data to validate performance and safety aspects determined in earlier phases. In civil aviation its primary purpose is to support the development and improvement of modern air vehicles and their systems, as well as to certify that these meet all necessary regulations set by the respective aviation authorities. Flight test planning is driven by a complex array of factors including costs, safety and required time to perform tests, which affect the accuracy of the data produced. Since in all cases available funding is limited, ways to reduce costs are subject to major consideration from test engineers during the planning phase.

A possible solution, that is gaining increased interest throughout the aircraft industry, is the use of subscale, radio controlled models for flight tests, which offer significant advantages in terms of cost efficiency and safety. In the first place, subscale flight testing allows test engineers to identify important flight characteristics of an aircraft configuration at lower flight operational costs prior to building a full-scale prototype. This could also improve the funding efficiency of every development process exploring possible flaws or design faults in the early stages. On the other hand, often tests are performed to investigate the aircraft's behaviour in extreme portions of the flight envelope like stall and spin conditions which expose both the expensive aircraft prototype and its pilot to a certain amount of risk. The use of subscale, remote controlled models makes it possible important questions regarding the aircraft's stability and control qualities to be answered without endangering the safety of the flight test team or the aircraft full-scale model. This is especially true for research projects where unknown flight characteristics of unconventional aircraft configurations with innovative design are studied and possible hazards cannot be anticipated with the necessary precision.

1.2 Objectives

To gain knowledge in the field of subscale flight testing, a dynamically scaled demonstrator of a university in-house business jet concept, the *Raven*, has been manufactured at the Department of Mechanical Engineering of Linköping University. In general, the targeted approach is to investigate what can be achieved within a low-budget university project driven mainly by educational programmes. The initial flights will primarily focus on testing the data logging system of the *Raven* and simply gather experience in flying a dynamically scaled model. Since the accuracy of certain on-board instruments is affected by the motion of the aircraft, the first flight tests will also be devoted to calibrate these and verify their proper functionality. Furthermore, aspects concerning the aerodynamics and stability of the model

are to be investigated. It is obvious that due to the significantly lower Reynolds numbers to be flown compared to full-size model flights, the acquired data will not be representative. However, it is of particular interest to analyse the accuracy of the results obtained in such manner and draw conclusions for further investigations.

A main part of the project work requires basic theoretical research on flight test methods and how to implement these into practical application with the current aircraft model. In particular, this work is devoted to the investigation of various techniques to identify important aircraft characteristics and their adaptation in the *Raven* case by taking into account available equipment and instrumentation. The information given here can be further divided into three main categories:

- in-flight calibration of instruments
- methods to extract aerodynamic data including lift, drag, side force and pitching moment.
- techniques to obtain the stability and control qualities of the aircraft.

Methods and conclusions presented in this work are targeted to improve the flight test planning process and give pilot assistance during the actual test procedures. Most of them are variations of already existing flight test techniques described in detail by different authors of aviation literature, however, they are adjusted to consider available data to be recorded, as well as pilot positioning and remote controlling of the aircraft from the ground.

1.3 Report structure

Chapter 2 contains technical information on the *Raven* aircraft regarding its dimensions, overall design characteristics and data acquisition system. It also gives an overview on the available data that is to be recorded during flight tests.

Chapter 3 gives a brief overview of flight testing in general and contains basic information regarding Pitot-static systems and mathematical modelling of the atmosphere, as well as fundamental principles in aerodynamics and their application in performance equations.

Chapter 4 primarily describes the calibration of pressure sensors with its main focus on in-flight techniques for determination of altitude and airspeed position error. In addition, the calibration of temperature sensors and vanes is briefly discussed.

Chapter 5 includes a mathematical model of the *Raven* turbines giving available thrust as a function of airspeed at different engine speeds and altitudes for standard day conditions.

- Chapter 6** describes techniques to obtain lift and drag coefficients as a function of angle of attack from flight tests, as well as to determine the aircraft stall speed. The appropriate data reduction sequences are presented. Furthermore, aircraft static stability is investigated giving flight test methods to determine functions of pitching moment and side force coefficient with angle of attack.
- Chapter 7** deals with aircraft dynamic stability flight testing. Basic concepts of longitudinal and lateral-directional dynamic stability are presented, as well as flight test methods to determine characteristic parameters of short period, phugoid, spiral, Dutch roll and roll mode.
- Chapter 8** gives a short summary of all topics discussed in this work with final statements and conclusions on the conducted investigation of flight test methods.
- Appendix A** contains a tabulated version of the International Standard Atmosphere model for low altitudes and useful charts regarding temperature measurement and compressibility correction.
- Appendix B** presents a derivation of the approximation relating altitude and airspeed position error correction used in calibration methods and gives a plot of this for low airspeeds and altitudes.
- Appendix C** includes static thrust and engine speed data provided by the manufacturer of *Raven's* turbines.
- Appendix D** gives an example calculation sequence to obtain total thrust for random values of airspeed, altitude and engine speed.

2 Aircraft data and properties

Some of the information on the *Raven* aircraft provided in this chapter is taken from several so far unpublished documents and other sources, which are property of Linköping University. These are therefore not referenced in the course of the text. However, the main information presented here regarding dynamic scaling and the *Raven* acquisition system can be found in **Lundström 2008**, a paper published by the Department of Mechanical Engineering for the 26th International Congress of the Aeronautical Sciences 2008.

The *Raven* aircraft is the result of a design study within student projects for advanced Aeronautical Engineering students carried out at the Department of Mechanical Engineering. In general, it is a university in-house design of a business jet/medivac, for which a dynamically scaled demonstrator has been built. Different views of this aircraft model are presented below in **Fig. 2.1**. The first two are taken from real pictures made at the Linköping University outside the building of the Department of Mechanical Engineering. The bottom ones are computer generated illustrations of the *Raven* CAD model.



Fig. 2.1 *Raven* – a subscale business jet demonstrator

The original *Raven* was designed according to the FAR-23 regulations mainly to be a business jet aircraft with a secondary task as an ambulance/medivac aircraft. The design was conducted for rural operation in mind with relative short take-off and landing distances. To fulfil the requirements of both business jet and ambulance aircraft, several innovations were

incorporated in the *Raven* design, the most impressive of all being a rear bulkhead door allowing patients to be carried in and out quickly. The basic dimensions of the original business jet/ambulance aircraft include a wing span of 14,4 m, total aircraft length of 13,4 m, fuselage cross section of 1,6 m, and wing area of 21,8 m² resulting in an aspect ratio of approx. 10. A desired cruise Mach number at 40 000 ft cruise altitude was determined to be 0,55. The main design concepts of the *Raven* are summarised in the following points:

- Conventional tail aft aircraft configuration
- Forward sweep
- Low wing configuration with positive dihedral angle
- T-shaped tail section
- Engines mounted approximately at the centreline on the rear part of the fuselage

For subscale flight testing the original *Raven* design was dynamically scaled, meaning that not only its dimensions were scaled, but also its weight, inertia and control system response, so that the dynamic properties of the model correspond to the ones of the full-scaled design. The main purpose of this was to gain knowledge in building and flying a dynamically scaled model. To downsize the original *Raven* design, FROUDE scaling methods with a scale factor SF of 14 % were applied. Accordingly, the model aircraft weight can be determined from the full-size aircraft weight and altitude and the scale factor with the following equation

$$W_2 = SF^3 \frac{\rho_2}{\rho_1} W_1 \quad , \quad (2.1)$$

where the full-size aircraft weight and altitude are denoted with the index “1” and the subscale model ones with “2”. From equation (2.1) can be seen that the model aircraft weight represents different combinations of full-size weight and altitude. To achieve desired low values of landing speed without applying complex high-lift devices, the model was scaled so that dynamics could be simulated only at sea level. It is possible to simulate higher altitudes by adding weight to the model aircraft, however even at sea level the resulting wing loading is already near the limit of the maximum allowed one for radio controlled models in Sweden.

The main dimensions, design parameters and some performance data, which are the result of downsizing the original *Raven* design, are presented in **Table 2.1**. All performance parameters included in the end are taken from preliminary design calculations conducted by Aeronautical Engineering students at Linköping University. In particular, the moments of inertia given are the ones determined at the Department of Mechanical Engineering by means of inertia measurement tests in which the author was personally involved. The test procedure consists of fixing the model aircraft (w/o fuel) on a special cradle, then the complete configuration is put on a beam with a specially designed cross section shape, and finally a small oscillation motion is set while its time period is measured with a stopwatch. This is

performed several times in order to obtain an average value for the time period. The same procedure is repeated with the cradle alone. This is to be done with the aircraft oscillating in pitch and roll. Both inertia moments are then computed utilising measured cradle time periods with and without the aircraft in a MATLAB code, in which the equations of pendulum motion are implemented. The inertia moment in yaw is calculated using the other two values. All measured inertia moments are smaller than the targeted ones, calculated using the scale factor.

Table 2.1 *Raven* demonstrator – technical data and specifications

Parameter	Value	Unit	
Total length	1,737	m	
Fuselage length	1,624	m	
Fuselage diameter	0,235	m	
Total wetted area	1,773	m ²	
Weight (w/o fuel)	9,75	kg	
Wing span b	2,0	m	
Wing reference area S_{ref}	0,399	m ²	
Wing MAC \bar{c}	0,22	m	
Aspect ratio A	10,025	-	
Maximum wing loading	25	kg/m ²	
Tailplane reference area S_{tail}	0,078	m ²	
Tail volume coefficient \bar{V}	0,4987	-	
Moment of inertia	roll I_{xx}	0,24	kgm ²
	pitch I_{yy}	1,46	kgm ²
	yaw I_{zz}	1,59	kgm ²
Desired cruise speed	55,6	m/s	
Maximum speed	145	m/s	
Stall speed	17,7	m/s	
Endurance	20	min	

In the remaining paragraphs of this chapter the *Raven* data acquisition system and the parameters to be recorded during flight tests are briefly presented. The acquisition system consists of a main board with CPU and data logging capability, a GPS receiver, an Attitude and Heading Reference system, vanes for angle of attack and sideslip angle measurements, pressure and temperature sensors, potentiometers for control surface deflection measurements, turbine motor interface and a telemetry system with stall warning system for pilot assistance. This additional telemetry system is the only component not connected to the main board. One can further divide the data acquisition system components into *main board*, *high level* sensors and *low level* sensors. High level sensors is a term used to describe digital sensors with an own data processor. On the other hand, the low level sensors are analogue sensors with no built-in processor. The main board consists of a PC104 computer, “Athena”, equipped with a

400MHz Pentium III “Coppermine” processor and 128MB RAM capacity. A 64MB external flash memory is used to run the onboard operating system and the logging software. To the high level sensors belong the Attitude and Heading Reference system, the GPS receiver and the turbine Electronic Control Unit interface. The first one contains accelerometers, rate of turn sensors and magnetometers, which provide a drift-free 3D orientation, as well as calibrated axial accelerations, rates of turn and Earth’s magnetic field data. Both filtered and raw data can be collected from this unit, whereas filtered data can be retrieved for example as Euler angles or as a rotation matrix.

The low level sensors include all remaining measurement systems – pressure and temperature sensors, α and β vanes, control surface deflection potentiometers. The Raven is equipped with a small nose boom, where a Pitot tube with both total and static pressure sensors and the two vanes for angle of attack and sideslip angle measurements are mounted. This can be seen on the first two pictures in **Fig. 2.1**. For temperature measurements, the appropriate sensor is placed under the fuselage in the upcoming airflow.

To sum up, from the above described instrumentation the available data to be recorded during flight tests include:

- Ambient temperature T
- Static pressure p
- Total pressure p_T
- Angle of attack α and sideslip angle β
- Axial and rotational accelerations in all three axes
- GPS position, speed and altitude
- Control surface deflections ($\delta_a, \delta_e, \delta_r$) and flaps position
- Turbine data (engine speed, exhaust temperature)

In addition, the fuel flow rate will be recorded, which can be used for calculations of the *Raven*’s actual weight. Also, a supplementary telemetry system is available, which consists of an Eagletree Systems Pro recorder – a low cost data logger suitable for hobby or UAV applications. Since no other altitude or airspeed data is available during flight testing, it can be used as an auxiliary system for transmission of real-time indications for these parameters.

3 Theoretical background

3.1 Overview of flight testing

Aircraft design is a complex process involving the integration of multiple systems and elements for the purpose of optimum performance, stability and control of the resulting air vehicle. Therefore, the development of modern aircraft is a product of several more or less independent engineering disciplines each covering different aspects of the design like propulsion, structure, systems and performance. To investigate the aircraft's characteristics and flying qualities in flight tests one should take into account the technical skills needed for effective operation of all these aspects and also factors like man-machine interface, which contribute to the overall complexity of the process. In addition, flight tests require excellent management and control for their successful and cost efficient performance. For all the above given reasons flight testing can be regarded as a separate discipline devoted to support the development process of an aircraft and to eliminate previously undetected design flaws.

There are various matters to be considered prior to making the flight tests planning. One of the first things on the agenda is to clarify the exact purpose of the test programme and the regulations that must be met, which determine further planning of test methods, costs, safety and required equipment. These and other important aspects are briefly discussed in this section to give a basic overview of the essence of the flight testing process.

3.1.1 Purpose and types of flight tests

The actual flight qualities of an aircraft are not always the same as the ones determined from preliminary design calculations in the course of its development. Therefore, at the end of the aircraft's design process a practical verification is often needed to support these previously computed parameters and help discover and improve possible weaknesses of which engineers remained unaware during earlier phases. A common practice to perform such verification is during flight tests, where also characteristics of the aircraft can be investigated for which computer simulations cannot always provide valid results, for example stability derivatives. According to their purpose, **Kimberlin 2003** (p. 4) classifies flight tests into several categories. One of the first reasons to perform tests originated from the lust for exploring the boundaries of physical laws and push engineering sciences to their limits. The idea was developed already in the early stages of aviation in the beginning of the last century to expand human knowledge in aeronautics, which was later enhanced to space programmes with the advancement of new technology. An important reason to conduct flight tests is for product development by aircraft companies, where the main goal is to test the actual characteristics of new products and fix possible flaws in their design. Compared to the research flight tests,

these are intended for economical purposes rather than to expand the state of the art. Other types of flight testing include experiments to determine if the aircraft can accomplish its intended mission and if its design complies with the established aviation requirements for operational safety. In any case, the main goals and specific objectives of the planned test programme have to be precisely defined at the very beginning, so that further test planning is not affected by undesired changes requiring additional costs in terms of time delay, equipment and working hours.

3.1.2 Flight test planning

Since one of the purposes of flight testing is to validate and improve design, changes will be made as a result, thus required tests should be carefully planned to avoid as much as possible constant alteration in time schedule due to newly appointed tasks. During the flight test planning process there are various factors to be considered by the management team in order tests to be effective. The most important ones include safety, costs and time schedule, which are presented in general in the following paragraphs. These aspects are primarily based on information given by **Ward 2006a** and do not necessarily apply precisely for low-budget projects with educational purposes, especially in case of subscale flight testing with a UAV.

Safety considerations should be dominant in the process of flight test planning, since neglecting these could lead to significant increase of costs or even termination of the programme, in the worst case due to human casualties and loss of the aircraft ruining the company's marketing image. Besides hazards that could arise from unforeseen problems with the design of the aircraft, the nature of a certain flight test might also contain some risks that should be carefully examined from the test team to reduce their likelihood of occurrence. Therefore, procedures for risk mitigation and management are adopted, which have fairly similar basic structures, however, some details might vary slightly within the individual companies. This risk management process can be summarised in the following six steps:

- Hazard Definition
- Cause Identification
- Risk Assessment.
- Risk Mitigation
- Residual Risk Assessment and
- Emergency Response

As a first step, test specific hazards are defined. These are risks that are unique for the nature of a certain test, or expressed in another way, "test specific hazards are those that arise as a direct consequence of the test activity" (**Ward. 2006a**, p.8). Usually in the beginning brainstorming sessions are performed, where test team members are encouraged to propose every possible idea that occurs to them. These are later thoroughly discussed to identify the ones

that are test specific and determine the danger they represent. During the second step a risk matrix is made showing the hazards' likelihood of occurrence and possible consequences. Examples of these and their appropriate codes are given in the following table.

Table 3.1 Risk Code Matrix (**Ward 2006a**)

<i>Likelihood of Occurrence</i>	<i>Code</i>	<i>Severity of Consequence</i>	<i>Code</i>
Nearly certain – if the test is repeated multiple times over a lengthy test campaign, the specified event should occur at least once.	A	Catastrophic – death, serious injury, or destruction of an irreplaceable test asset	I
Probable	B	Severe – injury involving lost of work days, damage to test assets requiring major repair and loss of schedule	II
Possible	C	Moderate – injuries not involving lost work days, non-minor repair (multiple shifts)	III
Improbable	D	Minor – no personnel injury, easily repairable damage (less than 1 shift), cessation of testing that day	IV
Remote	E		

The above given codes are then turned into a matrix with the rows representing the consequence class (I-IV) and the columns giving the likelihood of occurrence (A-E). Consequently, major hazards that are to be dealt with high priority are positioned in the left upper corner. These are reduced during the risk mitigation process moving them down and right in the matrix by applying different system modifications or specific procedures. The hazard analysis is completed in the last two steps where accepted risks for the flight testing and procedural response in case of emergency situation or a catastrophic event are defined.

Cost of a flight tests is another important factor to be considered in the planning process. These could be reduced by keeping supporting equipment and instrumentation as simple as possible without neglecting the required safety or accuracy of data collected. On the other hand, flying time should also be used efficiently, for example by combining different tests.

Last but not least, meeting the time *schedule* is vital for the success of a flight test programme. Aircraft manufacturers have contractual obligations for their products with severe penalties in case of production delays, usually expressed in terms of enormous additional costs. For military aircraft projects time delays might even cause the basic structure of the project to be reconsidered requiring new approval from the government for the changes made.

3.2 International Standard Atmosphere

The atmosphere affects highly aircraft performance and handling qualities due to the fact that aerodynamic and thrust forces are influenced by the surrounding air conditions. Changes in air pressure and temperature occur constantly in the atmosphere causing aircraft performance to vary with the time of the day and the season of the year. Therefore to evaluate results from flight tests at different conditions, a common baseline is needed upon which performance comparisons could be made and meaningful conclusions could be drawn. Over the last century several standards have been published by different authorities, most recent of them being the U.S. Standard Atmosphere, the ICAO Standard Atmosphere and the International Standard Atmosphere (ISA) published by ISO. However, all three models are identical up to an altitude of 32 km, which exceeds far beyond the limit altitude planned for the *Raven* flight testing, reducing them to one standard that is applied in this work. The ISA model and the equations defining it, as described by **Ward 2006a**, are given in the following.

The ISA model approximates the conditions typical for North America and Europe at 40° latitude averaged over the year and divides the atmosphere into layers with constant temperature lapse rate. Up to 11 km (*Troposphere*) air temperature decreases linearly with altitude. At 11 km the Tropopause occurs and the *Stratosphere* begins, where the temperature remains constant up to 20 km and then increases in the ranges between 20-32 km and 32-47 km with different lapse rates. At 47 km the Stratopause occurs and the *Mesosphere* begins, where the temperature decreases again with different rates up to the Mesopause at 79 km.

The ISA model is based on the following assumptions:

- Air is dry and behaves as a perfect gas with $R = 287,052 \text{ m}^2/(\text{s}^2\text{K})$ and $\kappa = 1,4$.
- The Earth's gravitational field is uniform with a constant acceleration due to gravity of $g_0 = 9,80665 \text{ m/s}^2$.
- Temperature varies linearly with increasing altitude.
- Standard sea level conditions are $T_0 = 288,15 \text{ K}$ (15 °C) and $p_0 = 1013,25 \text{ hPa}$.

In the ISA model all atmospheric variables are a function of altitude and therefore to derive the appropriate equations describing them, first it is necessary to introduce the various altitude definitions used in the aviation literature. In this work only three of them are considered:

Geometric altitude, h

Geometric altitude or true altitude is defined as the vertical distance between a given point in the atmosphere and a certain datum level, usually MSL.

Geopotential altitude, H

As stated above, the ISA model assumes a constant acceleration due to gravity with increasing altitude, thus a uniform gravitational field. In reality this is not true, since g

decreases with increasing altitude. **Ward 2006a** (p. 16) describes the geopotential altitude to have the following quality:

$$g_0 dH = g dh \quad (3.1)$$

Thus, a change in geopotential altitude would produce the same change of potential energy per unit mass in a uniform gravitational field, as a geometric altitude change in the real gravitational field. The function of gravitational acceleration with distance from the Earth's surface is given by:

$$g(h) = g_0 \left(\frac{6373 \text{ km}}{6373 \text{ km} + h} \right)^2 \quad (3.2)$$

The value of 6373 km represents the average Earth radius. A relation between geopotential and geometric altitude is then obtained by substituting equation (3.2) in equation (3.1) and integrating:

$$H = h \cdot \frac{6373 \text{ km}}{6373 \text{ km} + h} \quad (3.3)$$

Using equation (3.3), a variation between the two altitudes can be calculated. At 1000 m, a reasonable limit altitude for the *Raven* flight testing, equalising these introduces an error less than 0,016 % (approx. 6 cm). On that account, the terms “geometric altitude”, “geopotential altitude” and “altitude” will be considered identical for the purpose of this work and will be used as synonyms describing the same physical quantity.

Pressure altitude, h_p

Pressure altitude has the following definition, taken from **Young 2001** (Chapter 1, p. 13):

„The pressure height at a point in any atmosphere (Standard or Off-Standard) is the height in the Standard Atmosphere giving the same pressure.”

An altimeter will show pressure altitude if its reference pressure is set to 1013 hPa, however, since the *Raven* is not equipped with such device, the altitude is to be calculated from the sensor indicated barometric pressure. For this reason an equation relating these two parameters is to be derived by taking into account the assumptions in the ISA model. A relationship between pressure and altitude variation is given by the hydrostatic equation:

$$dp = -\rho g_0 dH \quad (3.4)$$

As stated above, the gravitational acceleration is assumed to be constant, thus requiring the use of geopotential altitude in equation (3.4). The main advantage it offers is a straightforward approach when solving this differential equation by regarding g independent of H . Taking into account the assumption that air is a perfect gas, air temperature can be introduced into equation (3.4) by means of the Equation of State:

$$p = \rho RT \quad (3.5)$$

Hence,

$$\frac{dp}{p} = -g_0 \frac{dH}{RT} \quad (3.6)$$

Furthermore, the air temperature can be expressed as a function of altitude with a constant lapse rate. Up to 11 km the variation of T with H is given by equation (3.7):

$$T = T_0 + \Lambda H \quad , \quad (3.7)$$

where Λ is the temperature lapse rate with a value of -6,5 K/km. Substituting equation (3.7) in (3.6) and integrating, yields the following expression for the barometric pressure:

$$p = p_0 \left[1 + \frac{\Lambda}{T_0} H \right]^{\frac{-g_0}{\Lambda R}} \quad (3.8)$$

Using equation (3.5), the air density can also be expressed as a function of altitude:

$$\rho = \rho_0 \left[1 + \frac{\Lambda}{T_0} H \right]^{\frac{-g_0}{\Lambda R} - 1} \quad (3.9)$$

Equations (3.7) to (3.9) represent the mathematical model of the ISA in the Troposphere and are used to calculate atmospheric variables at a given altitude. In performance calculations it is often common to express these parameters as dimensionless numbers giving the ratio to the standard sea level values. This is shown in the following equations:

$$\text{Relative pressure:} \quad \delta = \frac{P}{P_0} \quad (3.10)$$

$$\text{Relative temperature:} \quad \theta = \frac{T}{T_0} \quad (3.11)$$

$$\text{Relative density:} \quad \sigma = \frac{\rho}{\rho_0} \quad (3.12)$$

For Mach number calculations, an expression for the speed of sound is needed. On that account the LAPLACE formula is utilised, which for small changes in the state variables, as is the case in pressure waves propagation, assumes an isentropic change of state and can be written as follows:

$$a^2 = \kappa RT \quad (3.13)$$

Equations (3.7) to (3.13) are tabulated in SI units for every 50 m up to an altitude of 1600 m in **Table A.1**, given in **Appendix A**. This altitude of 1600 m covers far more than the planned flight testing altitude limit for the *Raven*.

3.3 Pitot-static systems

Aircraft airspeed and altitude are determined in flight by measuring pressure from the upcoming airflow with a so-called Pitot tube. A classical Pitot tube, as the one showed in **Fig. 3.1**, has two types of ports – a total pressure port and a static pressure port placed in different locations on the tube's body. In fluid dynamics the total pressure is defined from the incompressible BERNOULLI equation as the sum of the dynamic and the static pressure, or the pressure of the fluid if brought down to rest. Consequently the orifice for the total pressure is positioned directly in the upcoming airflow on the tip of the Pitot tube head, where air is slowed down to zero velocity and its pressure measured by a built-in pressure sensor. Due to the geometric shape of the Pitot tube the airflow accelerates around its nose causing static pressure to decrease, but it eventually reaches the ambient pressure value further down the tube. For this reason static pressure ports are located at a certain distance from the tip pre-determined for every Pitot tube shape. Due to its location perpendicular to the airflow a pressure sensor measures only the static pressure whereas the kinetic part is left out. Usually, there are several orifices in the tube positioned symmetrically to minimise flow inclination effects taking place at larger angles of attack or in case of a sideslip.

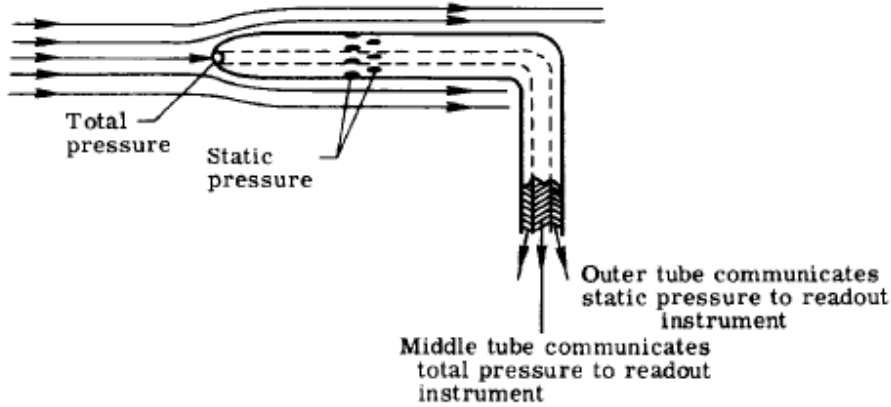


Fig. 3.1 Pressure measurement with a Pitot-static system (NASA 1975)

Classical Pitot systems obtain airspeed and altitude data by means of mechanical devices converting the measured pressure data and giving analogue indications in the cockpit. An airspeed indicator (ASI) uses both static and total pressure data to determine airspeed by measuring the differential pressure usually with a diaphragm. On the other hand, an altimeter uses absolute pressure to obtain the aircraft's altitude, thus applying only measured data from the static port. The *Raven* aircraft is not equipped with such instruments, however, it has a Pitot tube mounted on a short boom in front of its nose where pressure sensors will collect total and static pressure data. This raw information is then to be converted into altitude and airspeed data using the appropriate equations. For subsonic speeds the process of slowing down the air to rest in a Pitot tube can be assumed isentropic, thus the following relationships for pressure and temperature, taken from **Zingel 1999**, are valid:

$$\frac{p_T}{p} = \left(1 + \frac{\kappa - 1}{2} \cdot Ma^2\right)^{\frac{\kappa}{\kappa - 1}} \quad (3.14)$$

$$\frac{T_T}{T} = 1 + \frac{\kappa - 1}{2} \cdot Ma^2 \quad (3.15)$$

From equations (3.14) and (3.15) it is clear that the ratio of total to static value for a given fluid is a function of the dimensionless Mach number, defined as

$$Ma = \frac{V}{a} \quad (3.16)$$

Substituting equation (3.16) in (3.14) and solving for the airspeed yields:

$$V = a \cdot \sqrt{\frac{2}{(\kappa - 1)} \left[\left(\frac{p_T - p}{p} + 1 \right)^{\frac{\kappa - 1}{\kappa}} - 1 \right]} \quad (3.17)$$

Equation (3.17) gives the basic relationship between true airspeed and measured differential pressure for an isentropic process, where the values for pressure and speed of sound are functions of altitude. This means that calibrating an ASI in velocity units requires a different airspeed scale at each pressure altitude, which is not convenient for practical purposes. Therefore the calibration is based on standard day sea level values introducing several different airspeeds used in aircraft performance calculations. In the following these are briefly described and for every speed the definition given by **JAR-1 1996** is quoted.

Indicated airspeed, V_i

„‘Indicated airspeed’ means the speed of an aircraft as shown on its pitot static airspeed indicator calibrated to reflect standard atmosphere adiabatic compressible flow at sea level uncorrected for airspeed system errors.“

Since the *Raven* aircraft has no ASI, indicated airspeeds are not considered in this work. In the calibration methods described later the instrument corrected airspeed V_{ic} is taken into account instead. V_{ic} is calculated from the values for total and static pressure corrected for instrument error.

Calibrated airspeed, V_C

„‘Calibrated airspeed’ means indicated airspeed of an aircraft, corrected for position and instrument error. Calibrated airspeed is equal to true airspeed in standard atmosphere at sea level.“

By definition, substituting the values for static pressure and speed of sound with their equivalents for standard conditions at MSL in equation (3.17) yields the calibrated airspeed. The parameter $(p_T - p)$ is the actual differential pressure measured by the Pitot tube.

$$V_C = a_0 \cdot \sqrt{\frac{2}{(\kappa - 1)} \left[\left(\frac{p_T - p}{p_0} + 1 \right)^{\frac{\kappa - 1}{\kappa}} - 1 \right]} \quad (3.18)$$

Equivalent airspeed, V_E

„‘Equivalent airspeed’ means the calibrated airspeed of an aircraft corrected for adiabatic compressible flow for the particular altitude. Equivalent airspeed is equal to calibrated airspeed in standard atmosphere at sea level.“

The equivalent speed is also defined as the airspeed an aircraft would have at standard sea level conditions, if it produced the same dynamic pressure as it does while flying at the actual altitude with an airspeed V relative to the surrounding air (Young 2001, Chapter 1, p. 22). Hence, the factor relating both airspeeds equals to the square root of the relative density. Taking this into account in equation (3.17) yields the equivalent speed on the left hand side, as defined above:

$$V_E = V\sqrt{\sigma}$$

$$= \sqrt{\frac{2p}{(\kappa-1)\rho_0} \left[\left(\frac{p_T - p}{p} + 1 \right)^{\frac{\kappa-1}{\kappa}} - 1 \right]} \quad (3.19)$$

Equivalent speeds are commonly used in both structure and performance analyses, since their application eliminates the need for calculations at different altitudes. Operational safety limits and maximum loads are expressed as a function of equivalent speed in the so-called $V-n$ diagrams, where airspeed is plotted against load factor. At high altitudes and high speeds a compressibility correction factor is used to give the difference between equivalent and calibrated airspeed. According to Young 2001 (Chapter 1, p. 24), up to an altitude of 10 000 ft and calibrated speeds below 200 knots this factor is negligibly small and can be ignored. A chart giving the correction factor as a function of calibrated airspeed at different altitudes and Mach numbers is presented in Fig.A.1 from Appendix A. From there it is obvious that below 5000 ft (1524 m) and speeds of 300 kts (approx. 154 m/s) the correction factor is less than 0,5 % of the corresponding calibrated airspeed. Therefore, since no greater values of altitude or airspeed are planned for the *Raven* flight testing, the equivalent and the calibrated speed are considered equal in this work, both being further referred to as calibrated airspeed. Should performance calculations be negatively affected by this assumption in future flight testing where these limits are exceeded, Fig.A.1 can be used to obtain the correction factor.

True airspeed, V

„'True airspeed' means the airspeed of an aircraft relative to undisturbed air. True airspeed is equal to equivalent airspeed multiplied by $(\rho_0 / \rho)^{1/2}$ ”

True airspeed is an important parameter when calculating aerodynamic forces like lift and drag, since these are generated by the aircraft's motion relative to the surrounding air. Furthermore, true airspeed has an influence on the thrust forces produced by the engines and thus on the aircraft's performance, making it one of the basic variables to be determined accurately during flight testing. With the calibrated airspeed obtained from the Pitot tube measurements, V can be calculated from equation (3.19) using the actual relative density.

Ground speed, V_G

Ground speed is the actual speed of the aircraft relative to the ground, differing from the true airspeed due to the effects of wind. It can be obtained from the true airspeed by adding the wind component in flight direction (tailwinds regarded positive) or from GPS measurements.

For precise altitude and airspeed determination the Pitot-static system requires certain measurement errors to be carefully considered. These are primarily introduced by the practical measurement of total and static pressure in flight and by inaccuracies of the individual instruments. In the following several of the most common errors associated with Pitot-static measurements are briefly described, while later in Chapter 4 methods to obtain their corrections are presented in detail.

Instrument error

Like all measuring devices, altimeters and airspeed indicators may have a small error, the sources of which can be scale error, manufacturing deviations, magnetic fields, temperature fluctuations, friction, and the inertia of moving parts (**Ward 2006a**, p. 22). Usually this error is corrected using charts provided by the instrument's manufacturer. If no such charts are available, the instrument calibration is performed in the laboratory before the actual flight testing. In the *Raven* case the "instruments" for airspeed and altitude determination are simple pressure sensors, therefore in this work the term "instrument error" is used to describe the difference between sensor indicated value and true value obtained from static measurement in the laboratory (no influence of the airframe or any effects of motion considered).

Pressure lag error

Pressure sensing systems have a time delay in transmitting information from the pressure port to the sensor, which may result in pressure drop and thus introduce a measurement error. **Ward 2006a** (p. 23) describes two kinds of pressure lag error – an acoustic lag and a pressure drop due to the viscous effects of the airflow. Acoustic lag is caused by the propagation of pressure changes through the lines with the speed of sound, however since most Pitot-static systems have relative short pressure transmission lines, such effects are insignificant and can be safely ignored. The second type of pressure lag error occurs due to a pressure drop caused by viscous air flowing in the tubes. It is significant for a flight envelope with high rates of change of pressure, like rapid climb or descent (**Ward 2006a**, p. 23). For typical Pitot-static instrumentation pressure drop depends primarily on the tube length and internal diameter and the internal volume of the instruments. Compared to instrument and position errors, pressure lag errors are relative small for a normal flight envelope and are therefore disregarded in further calculations in this work.

Position error

The term "position error" describes a measurement error typical for Pitot-static systems caused by the inability of the total and static pressure pickups to sense the actual free-stream

pressure values (**Kimberlin 2003**, p. 32). There are two main sources for this error – the location of the Pitot tube in the pressure field of the aircraft and its positioning relative to the incident flow direction. In flight the presence of the airframe causes the surrounding static pressure to vary from point to point along the fuselage. This on the other hand varies with changes in airspeed and angle of attack, thus making it impossible for a single point to be located on the aircraft which remains at ambient pressure for all flight conditions (**Young 2001**, Chapter 1, p. 25). Total pressure measurements are less affected by the presence of the airframe, as long as the Pitot tube is not located in a boundary layer area, where kinetic energy is reduced. Hence, position error effects primarily the static pressure measurement, requiring a static port location where substantial deviations from the atmospheric pressure values would not occur with changing flight conditions and airflow inclinations. Generally, static position error is influenced by a range of variables and cannot be neglected in data evaluation, thus giving the need for an in-flight calibration performed during flight tests. This is the main subject of Chapter 4, where various calibration methods are described and their application in the *Raven* flight testing is discussed.

3.4 Basic flight theory

Apart from the above presented mathematical model describing the atmospheric features, performance analysis also requires an accurate modelling and calculation of the forces acting on an aircraft in flight. The following paragraphs give basic aerodynamic principles for defining lift, drag and pitching moment and the resulting equations used for performance calculations. Propulsive forces are only briefly mentioned as part of the laws of physics describing the aircraft's motion, however, their determination and particularly the thrust modelling of the *Raven* turbines are discussed thoroughly in Chapter 5. In performance analysis the aircraft is regarded as a mass point, therefore all forces act in its centre of gravity building a state of equilibrium, or in case of unbalanced forces, causing an increase or decrease of airspeed. Thrust exerted on the aircraft by the engines is assumed to act in flight direction, thus no angular deviation of the thrust vector from the flight path is taken into account. Furthermore, a simplification is made that there is no interaction between propulsive and aerodynamic forces, so that each can be considered independently.

3.4.1 Aerodynamic forces

In aviation literature several explanations can be found regarding the generation of lift on an aerofoil, each interpreting differently the laws of physics beyond this phenomenon. However, taking all these into account, one can draw the common conclusion that an aerofoil placed in a

moving stream of air will, depending on its shape, cause pressure differences on the upper and lower surface, thus will create a resultant aerodynamic force. **Anderson 1984** (p. 13) describes the generation of aerodynamic forces and moments to be due to two basic sources:

- Pressure distribution over the body surface
- Shear stress distribution over the body surface

By integrating these over the complete surface, one can obtain a resultant aerodynamic force F_A and a moment M acting on the body. Experiments show that F_A and M are a function of several independent variables as well as the shape of the body. These are shown below in equation (3.28), where the subscript „ ∞ ” indicates free-stream flow properties:

$$F_A = f(\rho_\infty, V_\infty, a_\infty, \mu_\infty, \alpha, S_{\text{ref}}) \quad (3.20)$$

With six dimensional variables and three fundamental units (length, mass, time), according to BUCKINGHAM’S π -theorem, three dimensionless parameters can be found. Applying this in further analysis results in the following relationship:

$$\frac{F_A}{0,5\rho_\infty V_\infty^2 S_{\text{ref}}} = f(Re, Ma_\infty, \alpha) \quad (3.21)$$

Equation (3.21) asserts that the ratio of the net aerodynamic force to the dynamic pressure multiplied by a characteristic reference area is a function of Reynolds number, Mach number and angle of attack. A detailed derivation of this statement can be found in **Anderson 1984** and **Roskam 1997**. These three parameters and their effects on lift and drag forces are explained later in this chapter.

In fluid dynamics, lift L is defined as the component of the resultant aerodynamic force perpendicular to the free-stream velocity and the drag D is the component parallel to V_∞ . In a two-dimensional flow field the angle of attack α is defined as the angle between the local airflow direction and the aerofoil chord line. In performance analysis however, this could lead to confusion, since on modern aircraft wings are often twisted in span direction to improve their aerodynamic characteristics, hence the angle of attack for different wing sections might vary according to their position. Therefore for an aircraft configuration AOA is usually given to a certain fixed datum line or reference plane. It is common to express aerodynamic forces and moments in terms of dimensionless coefficients, because they enable the application of the laws of mechanical similarity. For example, engineers often perform wind tunnel tests with subscaled models to determine aerodynamic coefficients which can then be carried over the full model if certain conditions are fulfilled. **Anderson 1984** (p. 27) describes these

conditions with the term “flow similarity”, where lift, drag and moment coefficients can be considered equal for two flows over geometrically similar bodies, if the similarity parameters, Re and Ma , are the same.

For an aircraft in a three-dimensional flow field, lift and drag coefficients are defined by

$$C_L = \frac{L}{0,5\rho_\infty V_\infty^2 S_{\text{ref}}} \quad (3.22)$$

$$C_D = \frac{D}{0,5\rho_\infty V_\infty^2 S_{\text{ref}}} \quad (3.23)$$

Since L and D are vector components of the resultant aerodynamic force, they can also be substituted in equation (3.21). Using the definitions for the dimensionless coefficients described above, it can be written as

$$C_L = f(Re, Ma, \alpha) \quad (3.24)$$

$$C_D = f(Re, Ma, \alpha) \quad (3.25)$$

Hence, for a given geometric shape, lift and drag coefficients are functions of Re , Ma and α only. The *Reynolds number* is an important dimensionless parameter in fluid dynamics defined as the ratio of inertia forces to viscous forces and is primarily used to describe flow characteristics. **Mair 1992** (p. 5) states that the effects of varying Reynolds number on C_L and C_D due to changes in speed and altitude are relatively small for the flight envelope of most aircraft and are therefore often neglected in preliminary performance calculations. As defined before in equation (3.16), the *Mach number* gives the ratio of flow velocity to the speed of sound and is often used to describe compressibility effects of flows at higher speeds. With increasing Ma the influence on lift and drag coefficients becomes more significant. For C_D this is especially the case in the so-called transonic speed range, where Ma approaches 1,0. However, for Mach numbers up to 0,3, air can be considered incompressible and C_L and C_D are assumed independent of Ma . Since values greater than 0,3 are not planned during the *Raven* flight testing, these effects will also be neglected in further analysis, thus lift and drag coefficients will be regarded as functions of angle of attack only. **Fig. 3.2** shows the variation of C_L and C_D with α for a typical aircraft in a clean configuration (high-lift devices and landing gear retracted).

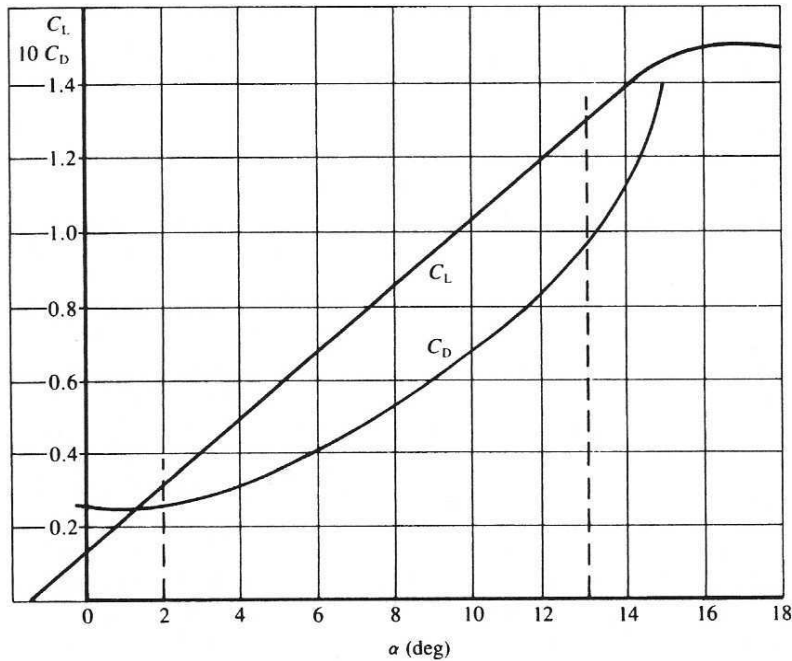


Fig. 3.2 Typical aircraft lift and drag functions with angle of attack (**Mair 1992**)

At low angles of attack C_L increases linearly with increasing α describing the so-called *lift curve slope*. For a thin aerofoil this is given by

$$\frac{dC_L}{d\alpha} = 2\pi \text{ rad}^{-1} \quad (3.26)$$

However, for an aircraft configuration the lift curve slope will have lower values due to various factors, including three-dimensional effects caused by the finite span of the wings. At higher AOA the function becomes non-linear eventually reaching a maximum and then falling rapidly due to flow separation and loss of lift. This non-linear area is affected by several parameters like wing shape, slat/flap settings and Reynolds number, therefore it is usually determined experimentally in wind tunnels or from flight tests at higher AOA near the aircraft's stall speed. For an aerofoil with moderate thickness, the maximum lift coefficient will increase significantly with increasing Reynolds number, which is generally less effective for cambered than for symmetrical sections (**Roskam 1997**, p. 80). Flows of higher Re values have an increased amount of energy and tend to overcome high pressure gradients, thus delaying flow separation and producing a higher lift coefficient at the same angle of attack. This also affects greatly the drag qualities of an aerofoil, since flow separations add a significant amount pressure drag increasing the total drag coefficient.

For an aircraft configuration the maximum lift coefficient determines the so-called stall speed V_S , defined by **JAR-1 1996** as the minimum steady flight speed at which the aeroplane is

controllable. It is usually given for different slat/flap settings depending on the wing configuration. In this work V_S will be regarded as the minimum level flight speed at which an aircraft can generate a lift force equal to its weight. Rearranging equation (3.22) and expressing V_S in terms of equivalent/calibrated airspeed, yields the following formula:

$$V_S = \sqrt{\frac{2W}{\rho_0 C_{L,\max} S_{\text{ref}}}} \quad (3.27)$$

Using this equation the maximum lift coefficient can be calculated for a measured stall speed during flight tests. The precise flight techniques and data reduction sequence are described in detail in Chapter 6.

Along with aerodynamic forces, pressure and shear stress distributions over an aerofoil surface also generate a moment which tends to pitch the aerofoil up or down. Its magnitude depends on the location of the reference point it is taken to be about and on the lift coefficient at a given angle of attack. Pitching moments are also expressed in dimensionless form, as shown later in equation (3.28), and the moment coefficient, given usually with a subscript indicating its reference point, is a function of Re , Ma and α as well. A unique location on an aerofoil is the so-called aerodynamic centre (AC), defined as “the point about which the variation of the pitching moment with angle of attack is zero” (**Roskam 1997**, p. 59), hence the moment about this point will remain constant with changes of C_L . This is a very useful quality, since the centre of pressure, where the resultant aerodynamic force acts, changes with varying AOA, and is not suitable as a reference point for further calculations.

In static stability analysis pitching moments exerted on an aircraft are referenced to its centre of gravity (CG) giving a rotation about the lateral axis. By definition moments are positive in a nose up direction. Similar to lift and drag coefficients, the pitching moment coefficient is also defined for a specific reference area, however it also related to a characteristic length called the Mean Aerodynamic Chord (MAC) as given below:

$$C_{M,c.g.} = \frac{M_{c.g.}}{0,5\rho_\infty V_\infty^2 S_{\text{ref}} \bar{c}} \quad (3.28)$$

MAC or \bar{c} is defined as “the chord of an equivalent wing, without taper, twist or sweep, which has essentially the same total lift and pitching moment of the actual wing” (**Young 2001**, Chapter 2, p. 6). For a planform wing area S it can be calculated by integrating the local chord length along the half wing span as follows:

$$\bar{c} = \frac{2}{S} \int_0^{b/2} c^2 dy \quad (3.29)$$

As described above, the term „aerodynamic centre” applies for an aerofoil in a two-dimensional flow field. However, this concept can also be carried over in static stability analysis for an aircraft configuration giving the so-called neutral point. It is defined as the point on an aircraft about which the pitching moment remains constant with varying angle of attack, or where the curve slope $dC_{M,c.g.}/dC_L$ equals zero (Kimberlin 2003, p. 214). Both the aircraft’s centre of gravity and neutral point positions are usually given in percent of MAC allowing engineers to make a comparison between different aircraft designs. This is discussed further as part of the static stability analysis in Chapter 6.

3.4.2 Drag polar

Aeroplane drag predictions are of great importance in preliminary design calculations determining the thrust required to achieve a specified performance or the performance obtainable for a given thrust. At a certain speed the powerplant’s fuel consumption is approximately proportional to the produced thrust making drag a crucial parameter for the economical efficiency of an aeroplane. In cruise performance analysis drag predictions affect important aeroplane characteristics like range and endurance and are therefore subject to thorough investigation. Since there exists no direct way to measure drag in flight, engineers usually rely on approximate mathematical models to start performance calculations, dividing total drag into different components. The most common classification that can be found in aviation literature estimates total drag as the sum of parasite, induced and wave drag. *Parasite drag* is defined as the drag dependent on lift production or the drag at zero lift. Generally, it can be further divided into interference drag, caused by the interaction between different parts of the aircraft in close proximity, and profile drag further classified in skin friction drag and pressure drag. *Induced drag* describes the lift-dependent part of the total drag. In the classical lifting-line theory it is referred to as the drag that results from the generation of a trailing vortex system downstream on a lifting surface of finite span. *Wave drag* is associated with the formation of shock waves due to compressibility effects at high subsonic and supersonic speeds. For conventional transport aircraft these usually appear at Mach numbers between 0,7 and 0,8, however, since compressibility effects are beyond the scope of this work, wave drag will be disregarded in further discussions.

A simple mathematical model for drag on moderate speed aeroplanes provides the so-called *parabolic drag polar*, which is not a statement of a physical law, but is more or less an empirical relationship. It is given below in equation (3.30) and also presented qualitatively in graphical form in **Fig. 3.3**.

$$C_D = C_{D_0} + \frac{C_L^2}{\pi A e} \quad (3.30)$$

Total drag is divided into two principal components, one dependent on lift (induced drag) and one independent of lift (parasite drag, denoted by C_{D_0}). The induced drag is defined as a square function of C_L for a given aircraft geometry described by the Oswald efficiency factor e and the aspect ratio A . The value of e is definitive for the lift distribution over the aircraft's wings and is generally between 0,65 and 0,90 (Young 2001, Chapter 3, p. 4). According to PRANDTL's classical lifting-line theory wings with a maximum value of e equal to 1,0 have an elliptical lift distribution, hence a uniform downwash velocity along the span. The aspect ratio A is another important geometric property for wings with finite span. Increasing the value of A reduces the effects of trailing vortices, thus decreases induced drag exerted on the aircraft. The aspect ratio is defined as

$$A = \frac{b^2}{S} \quad (3.31)$$

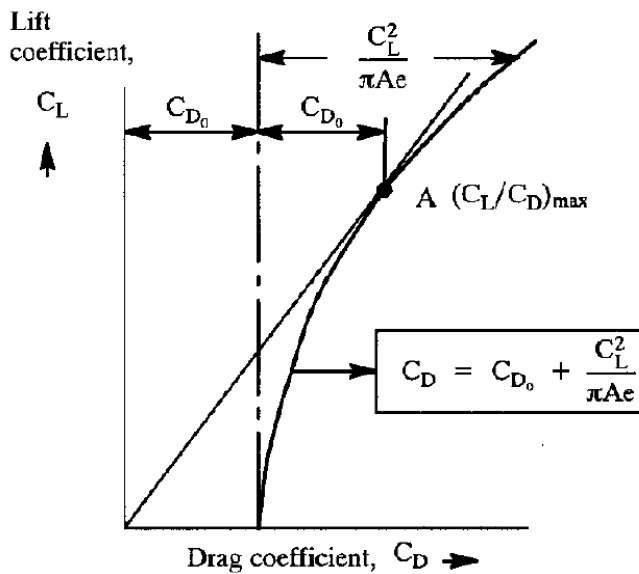


Fig. 3.3 Parabolic drag polar (Roskam 1997)

This simple parabolic drag polar model is a good approximation for conventional aircraft in normal flight conditions. However, it becomes inaccurate when the lift coefficient is either very small or very large (at stall speeds). In the first case, the parabolic model is unsatisfactory, because minimum drag usually occurs at a small positive lift coefficient (Fig. 3.4), not at zero lift, as stated by equation (3.30). On the other hand, at approaching stall condition boundary layer separation causes the induced drag to increase rapidly with

increasing C_L , making the above given square dependency inaccurate. An alternative drag polar, described by **Mair 1992** (p. 39) as the *modified parabolic law*, uses datum lift and drag coefficients at minimum drag and provides a more accurate model at low values of C_L . Equations for this alternative model can also be found in **Roskam 1997** and **Young 2001** (Chapter 3). However, due to its simplicity and adequate representation of the true drag polar during normal flight operation, equation (3.30) will be used in further performance analysis.

A common parameter used in performance calculations is the so called lift-to-drag ratio or glide ratio E , that describes, as its name suggests, the ratio of lift to drag force. Using the dimensionless form given by equations (3.22) and (3.23) it can also be expressed as the ratio of C_L to C_D . For a glider E denotes the distance travelled ahead for a unit of altitude lost.

$$E = \frac{C_L}{C_D} \quad (3.32)$$

The maximum value of E can be determined graphically, as shown in **Fig. 3.3**, by drawing a tangential line from the start of the coordinate system to the drag polar (point A). From equation (3.30) it can be shown that at maximum lift-to-drag ratio the zero-lift drag will equal the induced drag, hence the total drag coefficient will be the doubled value of C_{D_0} .

Fig. 3.4 presents a typical drag polar for an aeroplane in a clean configuration. The symbol β , not used in this work for this purpose, denotes the reciprocal of E giving a minimum value of 0,06, thus a maximum lift-to-drag ratio of approximately 16,7.

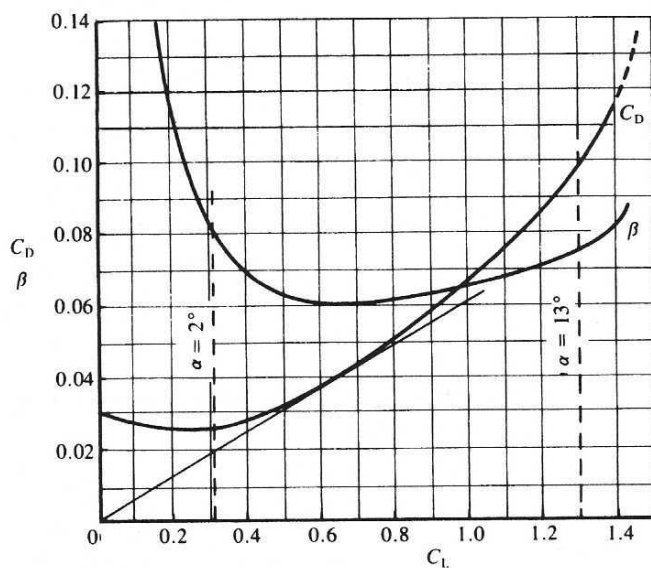


Fig. 3.4 Variation of C_D with C_L for a typical aircraft configuration (**Mair 1992**)

3.4.3 Performance equations

For performance analysis equations describing the dynamics of an aircraft in different phases of flight are needed. Therefore, as stated in the beginning of this section, the aircraft is reduced to a mass point with all forces acting in its centre of gravity, thus no inertia moments about its three axes are taken into account. Further simplifications include a straight line flight path and thrust produced by the powerplant to be in flight path direction, hence angular deviations due to AOA and thrust vector angle to the aircraft datum axis are ignored. The first approximation can be safely made for normal flight operations like climb and descent, where the curvature of the flight path is very small introducing a negligible rate of change of the flight path angle with time.

The governing equations can be obtained using both an energy method regarding the total energy of a moving aircraft as the sum of its kinetic and potential energy, or a free-body diagram with all forces acting on the aircraft considered. The latter one is adopted in this work and presented below in **Fig. 3.5**.

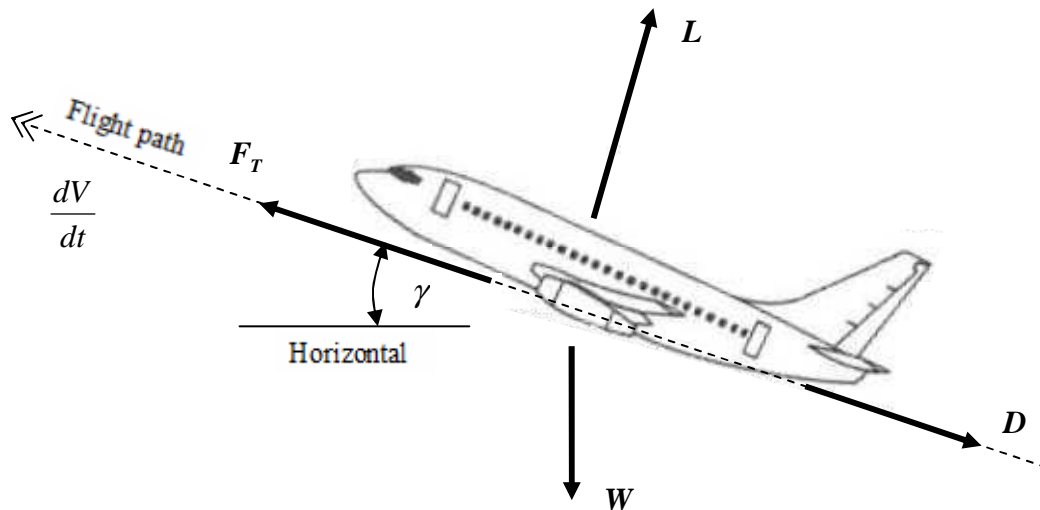


Fig. 3.5 Forces acting on an aircraft in a straight, symmetric flight

In flight path direction the application of NEWTON's laws of motion yields

$$F_T - D - W \sin \gamma = \frac{W}{g} \frac{dV}{dt} \quad (3.33)$$

Normal to the flight path the centripetal acceleration is approximately zero due to the infinite radius resulting from the small curvature, hence the sum of all forces can be estimated as

$$L - W \cos \gamma = 0 \quad (3.34)$$

Equations (3.33) and (3.34) are commonly used approximations for the motion of an aircraft in a symmetric flight at low AOA. These are referred to later in Chapter 6 when methods to determine lift and drag coefficients from flight tests are described, however, their application at higher values of α should be treated with a certain amount of caution due to the above made simplifications.

4 Calibration methods

Calibration of flight instruments is performed both in the laboratory to determine the instrument's own error and during flight testing in order to take into account the effects of speed, altitude and the surrounding airframe. Its main purpose is to establish the relationship between measured values and true values by comparing these and obtaining a certain measurement error for different ambient conditions. Contrary to laboratory calibration which is performed for all instruments, in-flight calibration concerns primarily the Pitot-static system position error influenced by the aircraft's pressure field and by flow inclinations. As laboratory instrument calibration is beyond the scope of this work, only brief references are made regarding temperature, pressure and angle of attack measurement, while the main emphasis in this chapter lies on various in-flight techniques for obtaining the position error.

4.1 Calibration of temperature sensors

Measurement of free-stream temperature in flight testing is important to determine the air density and thus affects the accuracy of the obtainable aerodynamic data. Because of their design and location temperature probes are subject to correction for both instrument error and temperature recovery factor. The instrument error for a temperature sensor should be determined in the laboratory by comparing measured temperature to actual temperature for a certain range, which is given by the planned flight test altitude. For a remote controlled subscaled aircraft a suggested temperature range would be between -10 and 40 °C where non-standard weather conditions up to 1000 m above MSL are considered.

Probes are designed to measure total air temperature by bringing the air to rest relative to the aircraft. Due to the occurring compression air experiences an adiabatic increase in temperature and therefore to obtain the static (ambient) temperature a kinetic term should be subtracted from the measured total temperature. For an adiabatic process the relationship between total and static temperature is given by equation (3.15). Since in practice the air does not come to a full rest and the temperature rise is not perfectly adiabatic, an empirical recovery factor is to be considered as follows:

$$\frac{T_r}{T} = 1 + k_{rec} \cdot \frac{\kappa - 1}{2} \cdot Ma^2 \quad (4.1)$$

According to **Ward 2006a** and **Kimberlin 2003**, for a good flight test measurement system the recovery factor usually will take values in the range between 0,95 and 1,0 and for subsonic speeds it will be constant throughout the flight envelope.

Using equation (3.13) for the speed of sound in equation (4.1) and solving for T_T gives:

$$T_T = T + k_{rec} \cdot \frac{\kappa - 1}{2\kappa R} \cdot V^2 \quad (4.2)$$

Kimberlin 2003 (p. 38) suggests a method for determining the recovery factor graphically by plotting T_T against the term containing the airspeed and the properties of air and then taking the slope of the resulting straight line. This could be done before flight testing for data measured in a wind tunnel where the precise airspeed is known. The exact total temperature is to be calculated from the sensor indicated temperature and the instrument error as follows:

$$T_T = \vartheta_i + \Delta\vartheta_{ic} + 273,15 \text{ K} \quad (4.3)$$

To summarise, for an indicated temperature with a known instrument error the ambient air temperature is to be obtained from the airspeed and the pre-determined recovery factor combining equations (4.2) and (4.3):

$$T = (\vartheta_i + \Delta\vartheta_{ic} + 273,15 \text{ K}) - k_{rec} \cdot \frac{\kappa - 1}{2\kappa R} \cdot V^2 \quad (4.4)$$

An alternative method to obtain the ambient air temperature from the indicated value of the probe gives **Fig. A.2** in **Appendix A**. The chart, taken from **NavAir 1992** (Appendix 9), provides a graphical relationship between the two temperatures dependent on the free-stream Mach number and the recovery factor of the probe. It is suitable for most standard temperature probes with a recovery factor between 0,95 and 1,0.

The *Raven* is not equipped with a typical temperature probe used on modern aircraft, however during flight tests a simple sensor will provide the necessary ambient temperature data. It will be located outside of the airframe in the incoming airflow protected from direct sunlight. Therefore the air is not brought to rest as in a temperature probe and this allows for the kinetic term in equation (3.15) to be neglected when calculating the ambient temperature out of the measured value. This is particularly true for low Mach numbers as it minimises the calculation error furthermore. The only correction applicable here is the instrument error of the sensor, pre-determined in the laboratory. For example, if the instrument corrected temperature is 40 °C and the aircraft is flying at a Mach number of 0,3 – the maximum values of these parameters planned for the flight testing – the ambient temperature, as calculated from equation (3.15), will be 34,5 °C, thus introducing an error of 5,5 °C. However, equation (3.15) assumes that the air is brought to rest adiabatically and the total temperature is the

measured temperature, thus for a sensor located directly in the airflow the increase of temperature due to a slowdown and respectively the measurement error will be of less amount. This statement is to be verified quantitatively for low speeds up to 150 km/h before the actual flight testing. The simple experiment will consist of holding the temperature sensor outside through the window of a moving car and reading the indications for different speeds. By comparing these with the known ambient air temperature a function of the measurement error could be derived.

4.2 Instrument calibration of pressure sensors

Due to their instrument error static pressure sensors and Pitot tubes need to be calibrated before flight testing by obtaining a characteristic curve for a certain pressure range which represents the relation between sensor indicated pressure and actual pressure. It should be noted that since this calibration is to be done before the actual flight testing, no influence of the aircraft's pressure field and thus no position error is regarded in the following.

In the atmosphere pressure decreases with increasing altitude and therefore a static pressure sensor calibration is to be done for a pressure range lower than the normal barometric conditions on the ground. On this matter a U-shaped tube with water can be used to achieve the low pressures for the planned test altitude range, as shown in **Fig. 4.1**. For a known reference pressure at one end of the tube, the unknown pressure at the other end can be obtained by measuring the water level difference in height.

$$p_{ic} = p_{ref} - \rho g \Delta h \quad (4.5)$$

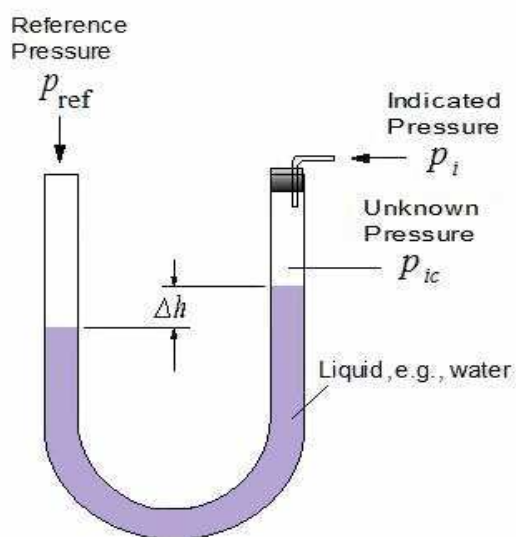


Fig. 4.1 Pressure measurement in a U-shaped tube

A comparison of the calculated pressure with the measurement from the static pressure sensor yields the static pressure instrument error correction:

$$\Delta p_{ic} = p_{ic} - p_i \quad (4.6)$$

Flight tests with the *Raven* aircraft are planned for altitudes between 300 and 500 m, however some manoeuvres would require climbing to a higher (safer) altitude, therefore a reasonable limit is up to 1000 m. With this in mind and considering non-standard conditions on the ground, the pressure altitude range for ISA conditions can then be assumed between -150 and 1400 m, approx. equal to a pressure range between 1030 hPa and 856 hPa. These threshold values consider conditions on the ground in both high and low pressure days. The pressure calibration steps between these values are to be defined according to the accuracy that can be achieved measuring water level differences in a U-shaped tube. Since the dependency between actual and measured value is normally linear, an instrument error could be obtained for the threshold values of both sensors and by means of some values within the pressure range the linearity could be verified. If some high-risk manoeuvres, for example stall or spin behaviour testing, require altitudes outside of the above described range, the linearity could be used to obtain an instrument error in these cases.

At high speeds the total pressure measured by a Pitot tube will have comparatively greater values than the static pressure and these could also be achieved using a water column instead of a U-shaped tube. The total pressure should be calculated dependent on the water depth by knowing the reference pressure above the water surface. The instrument error correction could then be computed as the difference between calculated and indicated total pressure.

$$\Delta p_{T,ic} = p_{T,ic} - p_{T,i} \quad (4.7)$$

Threshold values for total pressure can be determined from equation (3.14) using performance data about the aircraft's maximum and stalling speed presented in **Table 2.1**. This yields a total pressure range between 857 and 1096 hPa.

Normally flight instruments, especially mechanical ones, show a difference in their readings between increasing and decreasing values referred to as instrument hysteresis. This is to be taken in consideration during the pressure sensor calibration by making the calibration steps in both ascending and descending order. After graphically obtaining the characteristic curves for both sensors, mathematical functions with MS Excel could be derived using the tool "Trendline". This allows for an approximate expression which corresponds to a curve progression in a certain range and could be very convenient when using calculation software, as unlike charts mathematical functions can be implemented into programme codes.

4.3 Position error calibration methods

The static pressure source error leads to errors in both altitude and velocity measurements and therefore multiple approaches exist for determining their values. The most common ones include methods using free-stream static pressure measurement and true airspeed methods. When choosing a suitable calibration technique regarding the position error, there are certain factors that should be taken into account. Methods requiring only basic facilities and instrumentation may offer a simple way to calibrate Pitot-static systems, however the obtained data could lack in accuracy. In this case, considering the aircraft dimensions and the location of the pressure sensors in front of the aircraft's nose, one can predict a small influence of the pressure field around the airframe on the measured data, resulting in small position error. Therefore it is important that the chosen calibration method provides a precise measurement to identify this error. The main purpose is to obtain Δh_{pc} and ΔV_{pc} as function of the instrument calibrated airspeed V_{ic} for a certain range of altitudes planned for the flight testing. To minimise the effects of flow inclination (angle of attack and sideslip) static pressure orifices should be located on opposite sides relative to the centreline. If this is not possible the influence of these parameters on the position error should also be included in the calibration charts.

4.3.1 Background

Both altimeters and airspeed indicators use pressure measurements to convert them into specific flight data like altitude and velocity, and therefore their readings will be affected by the position error. As pressure indications are not directly obtainable from these instruments, it is convenient to express the position error in terms of altitude and airspeed corrections, rather than in terms of pressure. Such approach will also be adopted in this case, however it should be noted that although inconsistent with the instrument calibration in the previous section where terms of pressure were used, it allows for a more straightforward use of the calibration methods described by various authors in flight testing books.

As previously stated, none of the above mentioned instrumentation is available for the planned flight testing, thus airspeed and altitude are to be calculated manually using the raw pressure data from the sensors. Taking the calibrated airspeed definition for an ASI given by equation (3.18) and considering the properties of air yields:

$$V_C = a_0 \cdot \sqrt{5 \cdot \left[\left(\frac{P_T - P}{P_0} + 1 \right)^{\frac{1}{3.5}} - 1 \right]} \quad (4.8)$$

According to **Ward 2006a** (p. 24), a carefully designed Pitot tube will reduce the total pressure position error to a negligible value at flow inclinations of up to approximately 20°. Therefore, for the purpose of this work no position error in the total pressure measurement is considered, hence the instrument corrected total pressure $p_{T,ic}$ is used in equation (4.8). If the static pressure is also substituted with its instrument corrected value and thus regarded free of position error, V_C becomes the instrument corrected airspeed V_{ic} .

Taking into account equation (4.6) and (4.7) gives the following formula for V_{ic} :

$$V_{ic} = a_0 \cdot \sqrt{5 \cdot \left[\left(\frac{p_{T,i} - p_i + \Delta p_{T,ic} - \Delta p_{ic}}{p_0} + 1 \right)^{\frac{1}{3.5}} - 1 \right]} \quad (4.9)$$

To obtain the calibrated airspeed from V_{ic} a further correction should be made with respect to the static pressure position error:

$$V_C = V_{ic} + \Delta V_{pc} \quad (4.10)$$

As the atmosphere's variables change continuously, flight test data needs to be reduced to standard day conditions. Only on this basis results from different flight tests or even different vehicles can be compared equitably. Therefore static pressure measurements should be referenced to ISA conditions to calculate pressure altitude. Taking the instrument corrected value for the static pressure and substituting the values for gravity, specific gas constant and temperature lapse rate in the exponent term with their ISA equivalents, equation (3.8) can be written as

$$h_{p,ic} = \frac{T_0}{\Lambda} \cdot \left[1 - \left(\frac{p_{ic}}{p_0} \right)^{\frac{1}{5.25588}} \right] \quad (4.11)$$

In the same way as for the airspeed an actual (free of error) pressure altitude h_p can be obtained:

$$h_p = h_{p,ic} + \Delta h_{pc} \quad (4.12)$$

Since altimeters and airspeed indicators both use pressure data measured by the static port, their position errors are functions of the static pressure position error and therefore an approximation relating these parameters can be obtained for certain conditions. **Ward 2006a** (p. 28) derives a formula based on an isentropic flow process, thus valid only for subsonic speeds, which is given for aviation units (feet/knots). This is modified and presented below in equations (4.13) and (4.14) with no special units considered. The full derivation and a plot of equation (4.14) in SI units can be found in **Appendix B**.

$$\frac{\Delta p_p}{\Delta V_{pc}} \approx \frac{\kappa p_0 V_{ic}}{a_0^2} \left[1 + \frac{(\kappa - 1) V_{ic}^2}{2 a_0^2} \right]^{\frac{1}{\kappa - 1}} \quad (4.13)$$

$$\frac{\Delta h_{pc}}{\Delta V_{pc}} \approx \frac{V_{ic}}{\sigma_{std} g_0} \left[1 + \frac{\kappa - 1}{2} \cdot \left(\frac{V_{ic}}{a_0} \right)^2 \right]^{\frac{1}{\kappa - 1}} \quad (4.14)$$

According to **Ward 2006a**, this equation is a valid approximation for $\Delta h_{pc} < 1000$ ft (approx. 300 m) and $\Delta V_{pc} < 10$ kts (approx. 5 m/s), a sufficient range for flight testing with a subscaled aircraft model. For position error corrections of greater value its accuracy is questionable and alternate sources should be consulted.

4.3.2 Speed course method

There exist various techniques which use a true airspeed approach for in-flight calibration to determine the position error. Due to their simplicity and basic instrumentation requirements they offer an easy way to calibrate Pitot-static systems, however, they often lack accuracy if flight tests are not performed with the necessary amount of care. Using ground speed measurements or anemometer readings to obtain the calibrated airspeed, one can calculate the airspeed position error by comparing this value to the instrument calibrated airspeed, as shown by equation (4.10).

The speed course method consists of flying the aircraft at constant indicated airspeed and low altitude over an accurately measured ground course so a precise ground speed can be calculated using the course distance l and the measured time t between starting and terminal point. To eliminate crosswind effects the course is flown in both directions (opposite headings) and the ground speeds are averaged. Drift is allowed since the aircraft is not stabilised on a track, but is aligned on a heading parallel to the measured course. The course

distance is to be selected in accordance with the airspeeds being flown. Usually landmarks, which remind perpendicular “end lines” like roads or power lines, are used for this purpose. It should be noted that excessively long times to traverse will worsen the test results, but on the other hand, if using stop watches to measure time, the planned timing interval should be large compared to the error in marking the start and stop times. **Fig. 4.2** gives an illustration of the speed course technique:

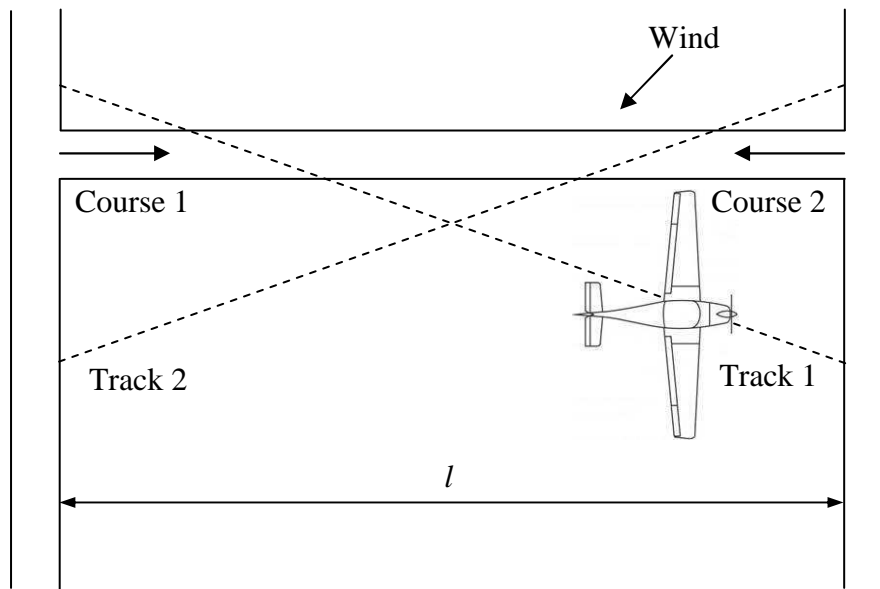


Fig. 4.2 Speed course geometry

The accuracy of this method depends on the ability to stabilise the aircraft over the course, as well as on the stopwatch timing precision. The most important parameter to be held constant is the indicated airspeed with a variation due to turbulence or poor pilot technique not more than 1 kt (approx. 0,5 m/s). For reducing wing effects flight test should be performed when the wind speed is near zero, often near sunset or sunrise (**Ward 2006a**, p. 35).

Appendix 9 of **AC23-8B 2003** gives certain test conditions and aspects of the speed course method that should be taken into consideration before and during flight testing. Some of them are summarised in the following with their SI units given:

- On test day the air should be as smooth as possible, wind speeds should not exceed 10 kts (approx. 5 m/s).
- Test altitude should be as low as practical, but at least one and one-half wing spans above the highest ground elevation to exclude ground effects. All test pairs should be performed at the same altitude.
- The airspeed range should be from 1,3 times the stall speed to the maximum level flight speed. For airspeeds above 250 kts (approx. 129 m/s) a course distance l of 5 miles

(approx 8 km) is to be anticipated. Below 100 kts (approx. 51 m/s) the limit distance is 1 mile (approx. 1,6 km).

These test conditions are provided by the FAA Advisory Circular for certification of Part 23 aeroplanes, but they are neither mandatory nor do they constitute a regulation. Although the original business jet design, upon which the *Raven* has been dynamically subscaled, was intended as a Part 23 aeroplane, these conditions could be used only as a basis of comparison and background information, but should not be utilised straightforwardly for the planned flight testing, because of the considerably smaller size of the aircraft.

A data reduction sequence for obtaining the position error from speed course method test measurements is shown in **Table 4.1**. It is similar to the one suggested by **Kimberlin 2003** (p. 35) with variations in some of the calculation steps due to different flight test data available in this case. The instrument corrected values for pressure, temperature and airspeed are to be obtained using the appropriate instrument error corrections.

Table 4.1 Speed course data reduction sequence

<i>Step</i>	<i>Calculate</i>	<i>From</i>
1	V_{ic}	Equation (4.9)
2	p_{ic}	Equation (4.6)
4	T_{ic}	$\vartheta_{ic} + 273,15$
5	δ	Equation (3.10) with #2
6	θ	Equation (3.11) with #4
7	σ	#5 ÷ #6
8	$\sqrt{\sigma}$	$\sqrt{\#7}$
9	V_G	$l \div t$ (for opposite headings)
10	V_C	#8 × #9 (for opposite headings)
11	$V_{C, avg}$	average V_C for opposite headings
12	ΔV_{pc}	Equation (4.10) with #11 and #1

To obtain Δh_{pc} first the position error Δp_p should be calculated from equation (4.13) using ΔV_{pc} . By correcting p_{ic} the ambient pressure and thus the true pressure altitude h_p can be calculated. A comparison between h_p and $h_{p,ic}$ yields the altitude position error correction, as given by equation (4.12).

4.3.3 GPS techniques

A variation of the speed course technique offers the use of a GPS receiver to obtain the ground speed, rather than calculating it from the course distance. Since the GPS ground speed is the first derivative of the position, a fixed error in the location of the aircraft will not affect the ground speed making conventional GPS receivers highly accurate in their measurements and thus applicable in this case. The component of the ground speed along the aircraft's heading can be obtained using the GPS ground speed and heading and the aircraft's track over the Earth. The test procedure follows the speed course method explained above, however before the actual data recording the aircraft should be stabilised in airspeed and altitude long enough for the GPS receiver to update, usually a matter of seconds (Kimberlin 2003, p. 37). Wind effects should also be minimised by flying reciprocal headings. Airspeed and altitude position error corrections can be obtained with the data reduction sequence from Table 4.1. Unlike the original speed course method, using a GPS receiver offers the advantage of flying the aircraft at higher altitudes as long as the air is smooth, thus allowing tests near stall speed.

Another similar technique using GPS ground speed data is the so-called "cloverleaf method" described by Ward 2006a (p. 36). It consists of an aircraft flying three different headings 120° to each other, thus forming a flight path trajectory reminding of a cloverleaf shape. By measuring the ground speed and the track over the Earth, one can graphically obtain the wind speed and direction, and thus the wind component along the aircraft's heading. An illustration of this method similar to the one given by Ward 2006a is shown in Fig. 4.3:

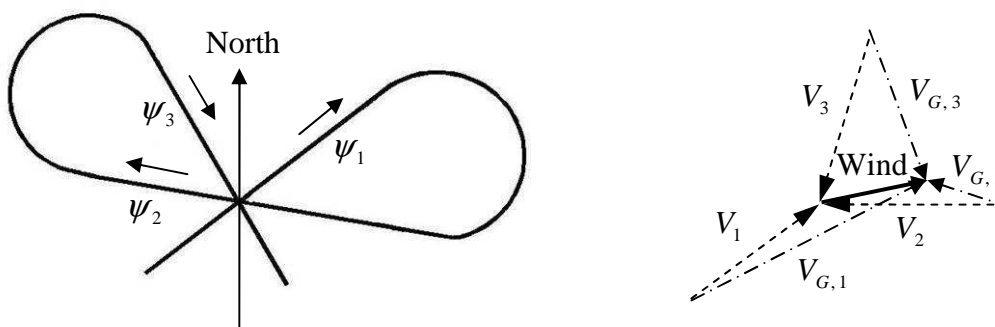


Fig. 4.3 Cloverleaf technique geometry / Ground speed relationships

Wind speed and direction can also be obtained from the local weather forecast or with a weather balloon before flight testing. Another way is to fly exact circles maintaining a constant altitude and allowing the aircraft to drift in wind direction. Using a GPS receiver to plot the trajectory of the flight afterwards, one can draw a line between the centres of the circles, which represents the wind direction. Using the recorded time and the length of the

drift, the wind speed can be calculated. With a known wind speed and direction, the aircraft can be flown into and with the wind to obtain the true airspeed. These manoeuvres however depend highly on piloting abilities and require more than one flight test and a results evaluation in the mean time, which could increase the costs and thus reduce the efficiency.

During flight testing with the *Raven* no real-time data regarding the aircraft's heading is available, which makes difficult for the pilot to maintain a constant heading throughout the flight envelope. If the above described techniques using GPS are to be utilised for calibration purposes, a constant heading during these manoeuvres is required, since not fulfilling this condition may affect considerably the accuracy of the results and make the acquired data questionable. As described in the speed course method, landmarks with a known heading could be used as a reference, however this is also problematic when piloting with a remote control device from the ground.

4.3.4 Calibration using GPS altitude data

By comparing the GPS altitude data with the pressure height calculated from the sensor measured static pressure a calibration curve for the altitude static position error could be obtained. Since a GPS device measures the geometric height above the Earth's surface at a certain point, a transformation into pressure height at standard day conditions should be made.

The calculation order is as follows:

- First, the instrument corrected pressure from the static pressure sensor should be converted into ISA pressure altitude $h_{p,ic}$ using equation (4.11) or by interpolation using **Table A.1** from **Appendix A**.
- Using the GPS altitude and the known elevation of the aerodrome the altitude above MSL could be obtained:

$$H_{MSL} = H_{GPS} + H_{airfield} \quad (4.15)$$

- For non-standard conditions (pressure and temperature) corrections need to be made, as described by **Scholz 2002** (p. 9 and 10). If the local QNH differs from p_0 , a correction of H_{MSL} is to be made for an altitude referenced to p_0 to be calculated. This correction applies only for a pressure deviation from the standard day conditions not for a deviation in temperature.

$$\Delta H = \frac{T_0 + \Delta T_{ISA}}{\Lambda} \cdot \left[1 - \left(\frac{QNH}{p_0} \right)^{\frac{1}{5,25588}} \right] \quad (4.16)$$

- If a temperature deviation ΔT_{ISA} from T_0 exists, a correction is to be made to obtain the pressure altitude corresponding to the ISA.

$$h_p = (H_{MSL} + \Delta H) \cdot \frac{T_0}{T_0 + \Delta T_{ISA}} \quad (4.17)$$

- A comparison to the instrument corrected pressure altitude yields the altitude static position error correction, as described by equation (4.12):

$$\Delta h_{pc} = h_p - h_{p,ic}$$

- For the pressure altitude h_p a relative density σ_{std} can be calculated or taken from ISA tables. Then, using equation (4.9) V_{ic} can be obtained with the sensor indicated pressure values and their corresponding instrument errors. Substituting these parameters and Δh_{pc} in equation (4.14) yields the airspeed position error correction. **Fig. B.1** from **Appendix B** can also be used to obtain the ratio of altitude to airspeed position error correction.

The above described calibration method relies on precisely measured altitude data therefore its application would be reasonable only for highly accurate GPS receivers. Unfortunately, the accuracy commercially available devices can achieve is approximately *10 m*, thus making the altitude data unsuitable for calibration usage. Taking into consideration the position of the pressure sensors on the aircraft, one can assume that a measurement error caused by the influence of the aircraft's pressure field would be smaller than the one of the GPS device. An alternative solution would be to use a Differential GPS, which can achieve accuracies from a couple of meters up to a few centimetres, but will also increase considerably the costs planned for the flight testing. The DGPS requires two receivers, one being the so-called base station with a precise known position on the ground. By comparing it to the position obtained from satellite signals, the base station calculates a difference and applies it to the second receiver located on board of the test aircraft.

4.3.5 Other commonly used methods

In the following several calibration methods frequently used in modern aviation are briefly presented, as described in various flight testing books. However their application in the *Raven* flight testing is due to limited resources and lack of instrumentation not possible.

Trailing cone method

This technique often applied in both commercial and military aviation uses a trailing cone with tubing to transmit static pressure located at a considerable distance behind the aircraft to measure the free-stream static pressure unaffected by the aircraft's presence. The distance should be at least 1,5 to 2 times the aircraft's length. This method is good for high speed flight, but could generate some problems at low speeds, since the cone's weight will cause it to fall down introducing airflow into the static port (**Kimberlin 2003** p. 33).

Pitot-static boom method

This method is standard for small aircraft, where a Pitot-static boom is mounted on the nose or on one of the wing tips, so that the static pressure ports are outside of the aircraft's pressure field. The *Raven* is equipped with a similar device in front of the nose, but it doesn't meet the necessary size requirements to be considered a nose boom. According to **Kimberlin 2003** (p. 32), the minimum distance for nose booms is 1,5 fuselage diameter ahead and for wing tip booms – one chord length. This technique is inaccurate at low speeds due to flow inclinations causing total pressure to enter the static port. This could be improved by using a free swivelling boom, which on the other hand experiences fluttering at high speeds.

Tower fly-by method

With the tower fly-by method only the static pressure source can be calibrated and if recorded data is to be used to obtain the airspeed position error, an assumption of a free of error total pressure measurement is to be made (**AC23-8B 2003**, Appendix 9). The technique is used primary by the military and consists of the aircraft flying down a tower fly-by line at constant speed and constant altitude approximately level with the eyepiece in the tower. Using the known height of the tower and a theodolite to determine the aircraft's height with respect to the tower, the height of the aircraft above ground can be obtained and then compared to the altimeter readings. A detailed data reduction sequence is given by **Ward 2006a** (p. 33) The main problems associated with this technique are the speed limitations due to the low test altitude and the requirements for an instrumented tower.

Pacer aircraft method

This technique uses a second, calibrated aircraft as a standard to calibrate the test aircraft. Though such aircraft is costly to maintain and fly, it allows for flying wide airspeed and altitude ranges and collecting rapidly static position error data. **Ward 2006a** (p. 33) describes two variations of this method, the first one being the pacer and test aircraft flying in formation. The important parameters to be maintained the same for both aircraft are altitude and airspeed,

whereas they should keep a certain distance so that neither pressure measurements are affected by the other's presence. The second variation consists of the test aircraft flying at different speeds past the pacer aircraft, which maintains a constant speed and altitude. The main disadvantage of this variation is the accuracy of reading the instrument indications of both aircraft simultaneously.

4.4 Calibration of vanes

Flow inclinations affect the aircraft's aerodynamic performance and their precise measurement is essential for evaluation of the data recorded during flight testing. For most aircraft AOA and sideslip measurements are done using vanes mounted in the front section of the fuselage. These movable devices orientate themselves in accordance to the movement of the surrounding air, giving the flow inclination relative to the aircraft. Since both lift and drag are functions of angle of attack, its precise measurement is of significant importance during flight testing. On modern civil aircraft flight instruments, for example the Stall-warning Indicator, require accurate data from the vane sensors for critical angle of attack and stall speed determination.

Conventional aircraft are symmetric to a vertical plane on the fuselage centre line, allowing for a symmetrical airflow around the wings during normal flight procedures. However, certain manoeuvres can introduce a sideslip, an airflow coming at a certain angle, the angle of sideslip β , relative to the plane of symmetry. This affects the aircraft's performance and can be an important parameter for example during cross wind landing. **Fig. 4.4** shows a typical shape and location of vanes used for determining flow inclinations. Unlike the Pitot tube on **Fig. 4.4** the *Raven* has only two vanes – one for AOA and one for sideslip measurement.



Fig. 4.4 Pitot tube with vanes for α and β measurement (SpaceAge 2008)

Calibration of vanes can be performed both statically in a wind tunnel and dynamically during flight tests. Its purpose is to obtain a curve relating actual and measured angle of attack. In a wind tunnel different AOA measurements at various airspeeds can be performed and compared to the indicated values from the vane. Certain aspects of wind tunnel measurement like a correction factor due to a deflection of the airflow upwards in the measuring section should be taken into account when determining the actual flow inclination. Normally a measured AOA should be independent of the airspeed value however at higher speeds a fluttering of the vane can cause inaccurate measurements. On the other hand, at very low speeds the vane may not be able to orientate itself exactly in the coming airflow and would indicate lower AOA values, which should also be determined during the wind tunnel tests.

Regarding in-flight calibration of an angle of attack sensor **Ward 2006b** (p. 3-22) describes the following method. Generally, the AOA is can be calculated from the geometric relationship given in equation (4.18):

$$\alpha = \theta_E - \gamma \quad (4.18)$$

In case of a steady, level flight the pitch attitude would equal the angle of attack, since no flight path angle and no acceleration along the flight path exist. The pitch angle could be measured using an attitude gyro, however with an accuracy in the order of 0,5° to 1,0° at best. Therefore a more common measurement is done using accelerometers oriented along the aircraft's longitudinal axis giving an accuracy between 0,1° and 0,3°. This measurement can be approximated with the following equation:

$$a_x \approx \sin \alpha = \sin \theta_E \quad (4.19)$$

Regarding sideslip angle calibration the following method is given by **Ward 2006b** (p. 6-24):

„The sideslip angle can be calibrated with analysis of rudder pulses using a Modified Maximum Likelihood Estimation (MMLE) routine. This estimation technique uses statistical methods to estimate sideslip angle by integrating side acceleration, yaw rate signals and other state variables.”

Since no wind tunnel measurements with the *Raven* are planned before the actual flight testing, data from the accelerometer along the aircraft's longitudinal axis during a steady, level flight can be used for an AOA vane calibration. Unfortunately the above described method for the sideslip angle calibration requires more flight data than available and therefore it is not applicable in this case. Instead the AOA vane can be taken as a reference and its calibration curve can be adopted for the sideslip angle with a certain amount of cautiousness when evaluating the recorded data.

5 Turbine thrust model and performance

The *Raven* is equipped with two gas turbine engines FS-70 Typhoon for remote controlled aircraft manufactured by the company FunSonic. These are regarded in the course of the text simply as “turbines” or “engines”. The company is generally based in Germany, but also have representation in the United States. Its main activity is manufacturing gas turbine engines for remote controlled aircraft and providing service for their repair and maintenance. Other company products include different variations of jet engines, as well as a TurboProp and a 2-shaft Heliturbine engine. Some additional information about the manufacturer and its gas turbine models is available on the official internet homepage, referenced as **FunSonic 2008**.

A sketch of the FS-70 Typhoon is presented in the figure below, taken from the operating manual accompanying the purchased engines. The FS-70 Typhoon is a modern remote controlled aircraft gas turbine with a radial compressor, an axial turbine stage and a ring combustion chamber. Its operation is carried out by a Turbine Control Unit (TCU) located in the fuselage and connected with the aircraft remote control receiver. A thrust/rudder lever at the pilot’s controls is used for thrust inputs. The engines are operated with K1 Kerosene fuel type, however, for starting procedures an electric motor mounted in front of the engine and a propane/butane gas mix are used to start the combustion process. When the engine speed reaches a certain value of RPM, fuel is switched to kerosene supplied from an external tank located in the aircraft by means of a miniature fuel pump. Power supply for the electric motor, the TCU and the fuel pump is provided by a 2400 mAh battery also located within the fuselage. Indicated parameters include engine speed and exhaust gas temperature. Since this chapter is devoted to determine a thrust model of the FS-70 Typhoon giving thrust forces as a function of altitude and airspeed for various engine speeds, it will not go into further details regarding the design and functioning of the engine. Some basic information can be found on the company’s internet homepage and in **Appendix C** where a three-view drawing of the engine with its main dimensions and performance parameters and data on static thrust as a function of engine speed, also taken from the operating manual, are presented.

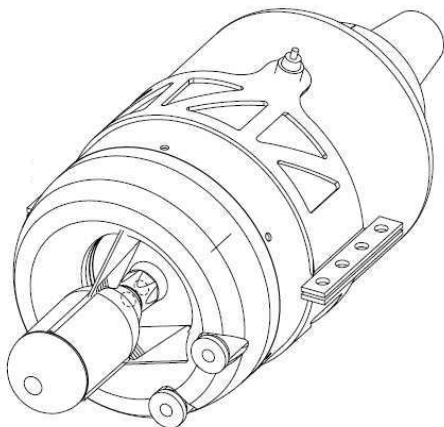


Fig. 5.1 FS-70 gas turbine for propulsion of remote controlled aircraft

One way to determine drag from flight tests is by measuring thrust exerted from the engines, therefore to obtain valid results a precise thrust model combining airspeed, altitude and engine speed is needed. However, since data provided by the manufacturer concerns only static thrust and does not include atmospheric and dynamic effects, alternative solutions should be sought. In this work a method of proportional scaling of thrust curves is applied, which consists of mixing available static thrust data from FunSonic with curves giving thrust as a function of airspeed and altitude provided by another manufacturer for a similar engine. Such mathematical manipulation will surely affect the accuracy of the obtained results giving the need for further verification. However, since no other thrust model of *Raven*'s turbines exists for the time being, this relative simple approach provides qualitatively reliable information on which future investigations can be based.

Several manufacturers of remote controlled aircraft gas turbines were contacted in order to find a similar engine to the one purchased for the *Raven*. The only available data combining airspeed and altitude variations was provided personally to the author by the company AMT. Its official internet homepage is referenced in this work as **AMT 2008**. The engine concerned is an Olympus HP – a significantly more powerful and more fuel consuming gas turbine than the FS-70 Typhoon with larger proportions. It probably does not provide the best solution for scaling thrust curves, however, due to lack of alternatives and information on other less powerful engines, Olympus HP data is used in this work. Basic specifications of both engines can be found in the following table:

Table 5.1 Engine specifications for FS-70 Typhoon and Olympus HP

Parameter	FS-70 Typhoon	Olympus HP
Engine diameter	82 mm	130 mm
Engine length	234 mm	267 mm
Turbine weight (w/o supporting systems)	734 g	2475 g
Maximum operational static thrust	69 N	229 N
Engine speed at max. static thrust	170 000 rpm	108 500 rpm
Fuel consumption at max. static thrust	185 g/min	640 g/min

To start the thrust modelling, first data on measured static thrust as a function of engine speed, provided by FunSonic and presented here in **Table C.1** from **Appendix C**, is transformed into a mathematical approximation by applying “Trendline” to the values given there. The second-order polynomial expression obtained in this way gives a direct function of static thrust with engine speed. A simplified form of this, where units are disregarded and the engine speed n is given in percentage of the maximum speed of 170 000 rpm, is presented below.

$$F_{T, \text{stat}} = 0,00850527n^2 - 0,16677n + 0,981 \quad (5.1)$$

Static thrust values obtained from equation (5.1) for different engine speeds, given in **Table C.1**, are plotted in **Fig. 5.2** together with the static thrust data provided from the manufacturer. From this it is obvious that the polynomial expression matches precisely the progression of the curve given by FunSonic and can be utilised in further calculations.

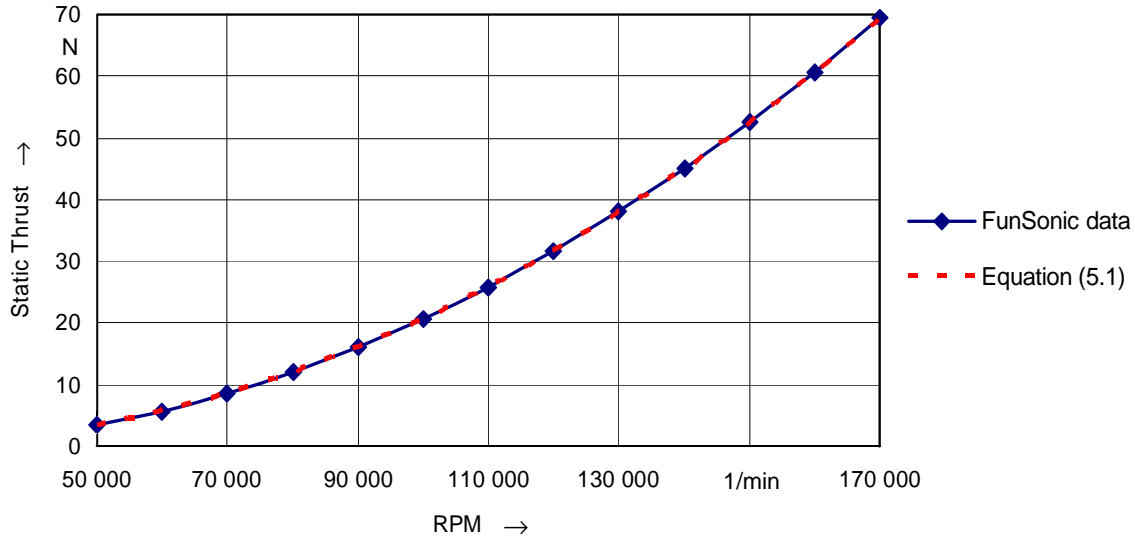


Fig. 5.2 Static thrust versus engine speed – polynomial approximation

Using equation (5.1), one can then calculate values of static thrust for 80, 60 and 40 percent of the maximum engine speed. These and the combined thrust values for both engines obtained with multiplication by a factor of 2 are presented in the following table. In further references to the thrust of both engines in this section the term “total thrust” is used.

Table 5.2 Engine speed and static thrust for one and both engines

Engine speed n [%]	Static thrust	
	Single engine $F_{T, stat}$ [N]	Both engines $F_{T, stat}$ [N]
100	69,36	138,71
80	42,07	84,15
60	21,59	43,19
40	7,92	15,84

To obtain a function of total thrust with airspeed for different altitudes and engine speeds, the data provided from the company AMT is utilised. This data cannot be found on the company’s internet homepage and since it is strictly the property of AMT and is protected by copyright laws, no complete charts are presented in this work, however, read-out values of total thrust for true airspeed steps of 25 m/s at 100 % engine speed and three different

altitudes are included in the last column of each of the following tables. Values of total thrust for the FS-70 Typhoon are obtained for the engine speeds n given in **Table 5.2**. First, curves are scaled for standard mean sea level conditions starting with the values for total static thrust (airspeed equals zero). To obtain total thrust for an airspeed of 25 m/s the static thrust value for each engine speed is multiplied by the ratio of total thrust at 25 m/s and the one at 0 m/s for the Olympus HP turbine. An example of this for the maximum engine speed is shown below:

$$138,71 \text{ N} \frac{437 \text{ N}}{458 \text{ N}} = 132,35 \text{ N}$$

Every next value for total thrust at the appropriate airspeed is obtained using this linear scaling method – the value for the previous airspeed is multiplied by the Olympus HP ratio of current airspeed total thrust to previous airspeed total thrust. Calculated values at MSL for airspeeds up to 200 m/s are summarised below in **Table 5.3**.

Table 5.3 Total thrust variation with V and n for standard conditions at MSL

Airspeed	FS-70 Typhoon at MSL				Olympus HP at MSL
V [m/s]	F_T [N]				F_T [N]
–	$n = 100\%$	$n = 80\%$	$n = 60\%$	$n = 40\%$	$n = 100\%$
0	138,71	84,15	43,19	15,84	458
25	132,35	80,29	41,21	15,11	437
50	129,32	78,45	40,26	14,77	427
75	127,81	77,53	39,79	14,59	422
100	127,81	77,53	39,79	14,59	422
125	129,02	78,27	40,17	14,73	426
150	133,26	80,84	41,49	15,21	440
175	137,80	83,60	42,90	15,73	455
200	143,86	87,27	44,79	16,43	475

Besides MSL conditions the information provided by AMT covers also altitudes of 10 000 and 16 000 ft. Calculations of total thrust values at these are presented in the following. Static thrust data given by FunSonic is valid only for standard day conditions at mean sea level and do not apply for other altitudes, therefore scaling calculations for 10 000 and 16 000 ft cannot be started as described above. The method applied for both altitudes is a multiplication of the value of total thrust for MSL at the appropriate airspeed and engine speed with the ratio of total thrust at MSL to total thrust value at respectively 10 000 or 16 000 ft for the Olympus HP turbine. This is done for all airspeeds up to 200 m/s and all four engine speeds. It can be

shown that such manipulation is mathematically the same as if the values were calculated with the scheme applied for MSL between 25 and 200 m/s, and yields precisely the same results due to the linear scaling. Examples of total thrust determination at 10 000 ft and 80 % engine speed for airspeeds of 0 and 25 m/s are presented in the following:

$$84,15 \text{ N} \frac{375 \text{ N}}{458 \text{ N}} = 68,90 \text{ N}$$

$$80,29 \text{ N} \frac{364 \text{ N}}{437 \text{ N}} = 66,88 \text{ N}$$

Results from calculations applied for all other airspeeds up to 200 m/s and all four engine speeds are presented in the following table:

Table 5.4 Total thrust variation with V and n for standard conditions at 10 000 ft

Airspeed	FS-70 Typhoon at 10 000 ft				Olympus HP at 10 000 ft
V [m/s]	F_T [N]				F_T [N]
–	$n = 100\%$	$n = 80\%$	$n = 60\%$	$n = 40\%$	$n = 100\%$
0	113,58	68,90	35,36	12,97	375
25	110,24	66,88	34,32	12,59	364
50	107,22	65,04	33,38	12,24	354
75	106,61	64,67	33,19	12,17	352
100	106,61	64,67	33,19	12,17	352
125	107,52	65,22	33,48	12,28	355
150	110,55	67,06	34,42	12,62	365
175	114,48	69,45	35,64	13,07	378
200	119,63	72,57	37,25	13,66	395

For total thrust calculations at 16 000 ft the scheme from above can be applied, or due to the given linearity, the obtained thrust values at 10 000 ft can be taken instead of those at MSL. This does not affect the results in any case and is applied here only as a confirmation of the linear characteristics of this method. Again values up to 200 m/s for all four engine speeds are calculated and included in **Table 5.5**. Before that, a calculation example for 0 and 25 m/s at 60 % engine speed is given.

$$35,36 \text{ N} \frac{329 \text{ N}}{375 \text{ N}} = 31,02 \text{ N}$$

$$34,32 \text{ N} \frac{320 \text{ N}}{364 \text{ N}} = 30,17 \text{ N}$$

Table 5.5 Total thrust variation with V and n for standard conditions at 16 000 ft

Airspeed	FS-70 Typhoon at 16 000 ft				Olympus HP at 16 000 ft
V [m/s]	F_T [N]				F_T [N]
–	$n = 100\%$	$n = 80\%$	$n = 60\%$	$n = 40\%$	$n = 100\%$
0	99,64	60,45	31,02	11,38	329
25	96,92	58,79	30,17	11,07	320
50	94,19	57,14	29,33	10,75	311
75	93,59	56,77	29,14	10,68	309
100	93,59	56,77	29,14	10,68	309
125	94,80	57,51	29,51	10,82	313
150	97,22	58,98	30,27	11,10	321
175	100,85	61,18	31,40	11,51	333
200	105,70	64,12	32,91	12,07	349

With all necessary values for total thrust obtained, one can plot these versus true airspeed V , as shown in **Fig. 5.3**, to determine thrust curves for all three different altitudes and four engine speeds. According to the information given by AMT, these have the typical shape of a thrust curve for a remote controlled aircraft gas turbine. With increasing airspeed thrust decreases due to a smaller momentum difference occurring between engine inlet and outlet. However, after reaching an airspeed value of 75 m/s, produced thrust remains constant up to 100 m/s regardless of engine speed setting and surrounding atmospheric conditions. This is strictly due to the data provided by AMT, where for all three altitudes thrust curves are given as horizontal lines between 75 and 100 m/s, and is to be verified for the FS-70 Typhoon engine. For speeds above 100 m/s a gradual increase in thrust can be noticed, which is consistent with the Olympus HP curves. However, this shape is not characteristic for full-size transport aircraft jet engines, where for a subsonic speed range thrust decreases with increasing true airspeed or for cruise performance – increasing Ma . Such thrust variations with Mach numbers of up to 1,0 can be found in **Scholz 2000** for generic turbojet engines with different bypass ratios. These curves have similar shape to the ones given by **Mair 1992** (p. 85) for a Rolls-Royce RB211-535E4 turbofan engine with no minimum thrust values, as opposed to the ones plotted in the figure below. On the other hand, thrust variation with altitude is consistent with data found in these references, where F_T decreases with increasing altitude mostly due to thinner air resulting in decreased operational mass flow.

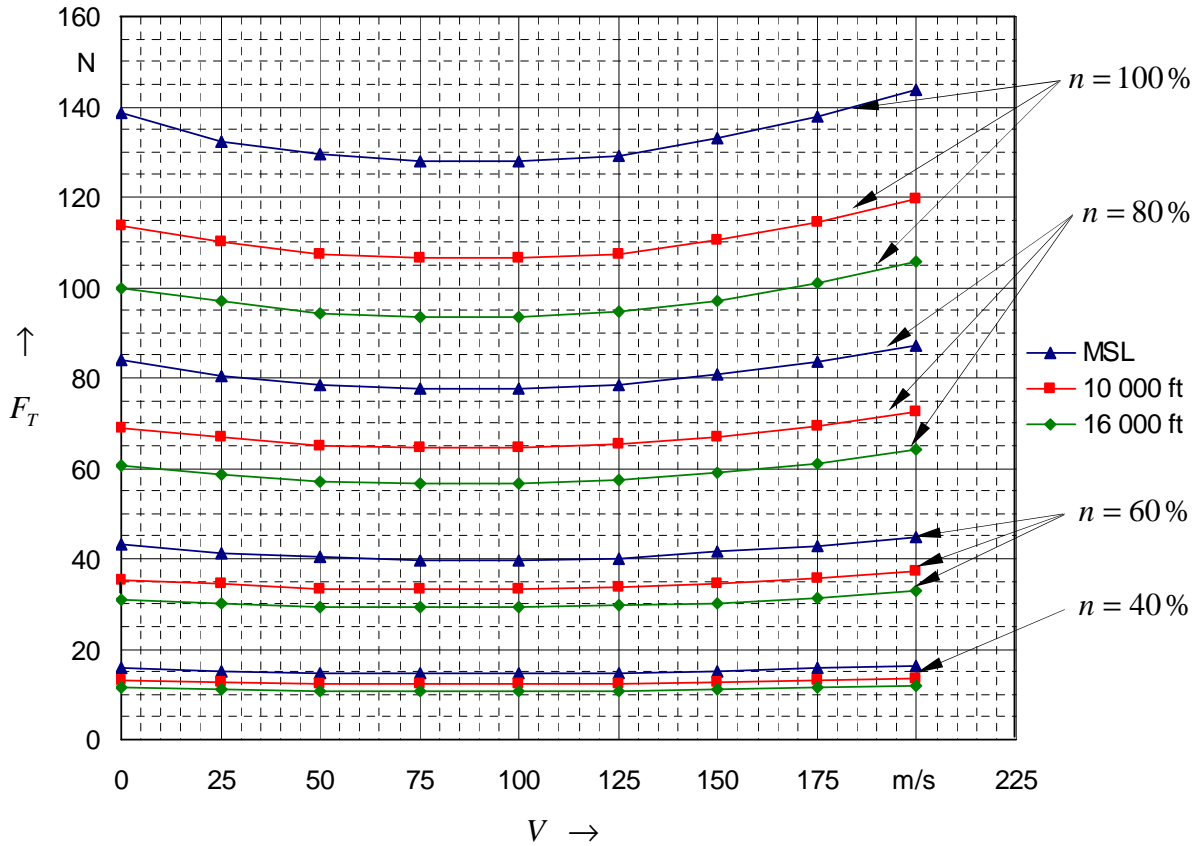


Fig. 5.3 Total thrust as a function of airspeed, altitude and engine speed

The above illustrated curves give total thrust as a function of airspeed for several altitudes and engine speeds, however, if a targeted value of n or H does not correspond to these conditions, the desired thrust needs to be obtained by means of graphical interpolation directly in the chart. Another possibility that requires numerical manipulation is to determine a total thrust function with airspeed at three different altitudes for a certain value of n and then obtain a curve representing the progression of total thrust with altitude for a given airspeed. An example calculation for this method is given in **Appendix D** with the aircraft taken to perform a flight test at 400 m with an airspeed of 110 m/s and a value for n of 75 %.

To conclude this chapter, the most important aspects and possible flaws of this model are summarised. First, all functions of thrust with airspeed and altitude were acquired entirely using data provided by the company AMT for their Olympus HP gas turbine. Although it has similar design to the *Raven* FS-70 Typhoon engine, it is significantly more powerful and more fuel consuming, which makes it not the most suitable variant for a linear scaling manipulation. However, since no other information regarding airspeed and altitude dependencies is available at the time being, this modelling method is applied requiring further verification and demonstration of the accuracy of its results. Secondly, data provided by FunSonic about the change of thrust with increasing engine speed applies only for standard sea level conditions, however, due to the linear scaling for every two values of n the ratio of total thrust at other

altitudes will be precisely the same as for ones at MSL. This implies that the change of thrust with engine speed is assumed to be the same at every altitude, for which no data is available from the manufacturer. Furthermore, data provided by AMT applies only for engine speeds of 100 %, however, it is also used for scaling the values of lesser engine speeds. Such approximations due to lack of information will also introduce a certain amount of error in thrust calculations. For all the above listed reasons this thrust model is to be applied with cautiousness and its results should be considered questionable until further verification is conducted.

6 Flight test methods to determine aerodynamic performance and static stability

Aerodynamic parameters like lift, drag, side force and moment coefficients are usually determined from wind tunnel tests where airspeed, angle of attack and angle of sideslip can precisely adjusted with no deviations due to gusts or other atmospheric disturbances. For these tests the aircraft model is mounted on a six-element force balance that measures quasi-statically forces and moments in all three axes. Out of the measured values one can calculate their dimensionless coefficients using the definitions described in Chapter 3. Before the first flight tests with the *Raven* a method called *car top testing* is to be conducted by the Department of Mechanical Engineering at Linköping University. It consists of the model mounted via a mechanical rig on the roof of a moving at moderate speeds (up to 120 km/h) ground vehicle, where forces and moments are measured by differential strain gauges. Main parameters to be identified include lift and drag as a function of angle of attack, side forces, pitching moment and stall behaviour, as well as flaps and control surfaces deflections. Results from this experiment are not expected to achieve the accuracy of wind tunnel tests, however they can be primarily used to identify the aircraft's characteristics before the first flight and make sure no undesired effects take place. On the other hand, more precise aerodynamic data can be obtained from flight tests, which requires flying the aircraft in a specific way, as well as correcting recorded data for various factors including non-standard day conditions. Such methods and their application on the *Raven* aircraft are the main subject of this chapter.

6.1 Lift and drag determination

6.1.1 Steady level flight

In the last section of Chapter 3 were presented the governing equations for a symmetric flight obtained by taking the balance of all forces acting on an aeroplane. Using these one can calculate lift and drag from values that can be determined during flight like thrust and weight. By manipulating the aircraft's airspeed and altitude, one can reduce the performance equations to simple relationships with only basic parameters. One possibility is to use the flight condition known from cruise performance analyses as steady level flight. This is the state in which civil transport aircraft remain through most of their operational time and it consists of the pilot maintaining constant airspeed and altitude by means of inputs from the control column. Using this information one can simplify equations (3.33) and (3.34) based on the following two statements. First, since the change of altitude with time is zero, the flight path angle will also be zero, hence the pitch attitude will equal the angle of attack. Secondly, since the change of velocity with time is zero, no acceleration takes place along the flight path.

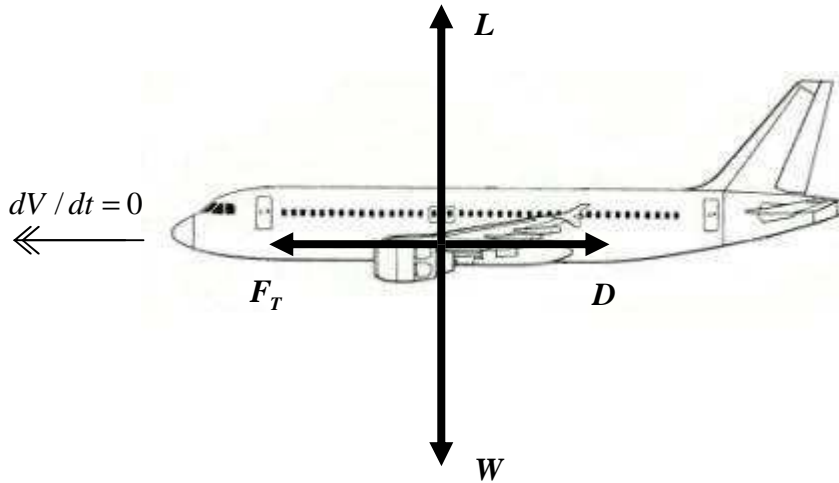


Fig. 6.1 Forces acting on an aircraft in a steady level flight

From **Fig. 6.1** the following relationships can be derived

$$F_T = D \quad (6.1)$$

$$L = W \quad (6.2)$$

Equations (6.1) and (6.2) are the two governing equations for an aircraft during cruise stating that in a steady level flight the lift is equal to the aircraft's weight and the required thrust from the powerplant is equal to the aerodynamic drag produced from the motion in the surrounding environment. Taking these statements into account C_L and C_D can be calculated by replacing the values for weight and thrust in equations (3.22) and (3.23). During flight tests the flow rate of fuel pumped to the engines will be measured which allows for the actual weight of the aircraft at any given time to be calculated in the evaluation process afterwards. Using the pre-determined weight at test take-off, one can obtain the current weight of the aircraft by integrating the fuel flow rate over the time period. To determine the aeroplane's drag from equation (6.1), thrust produced by the powerplant is to be measured or properly modelled using information from the engines' manufacturer. Since the surrounding atmosphere affects engine performance, measured thrust during flight tests is to be corrected for non-standard conditions, usually with only temperature deviations considered. However, at this point no direct thrust measurement on the *Raven* aircraft is possible, making the curves presented in Chapter 5 the only available information on this matter. These can be used to determine thrust at a calculated pressure altitude and measured engine speed with no further corrections required as the curves are given for standard day conditions. If eventually thrust measurements become available during future flight tests, **Ward 2006a** and **Kimberlin 2003** should be consulted for corrections regarding non-standard temperature variations.

Instead of calculating the true airspeed using test day density information, one can apply the corrected for instrument and position error calibrated airspeed in equations (3.22) and (3.23) reducing the number of variables to two for each equation and thus simplifying further programming codes for calculation software. With the values for weight and thrust these equations can be written as

$$C_L = \frac{W}{0,5\rho_0 V_C^2 S_{\text{ref}}} \quad (6.3)$$

$$C_D = \frac{F_T}{0,5\rho_0 V_C^2 S_{\text{ref}}} \quad (6.4)$$

There are several things one should keep in mind when performing a steady level flight for lift and drag determination. First, to calculate lift from the aircraft's weight, it is not necessary to maintain constant airspeed. The important parameters that must be kept steady to justify the statement of equation (6.2) are flight altitude and angle of attack. In a level flight the AOA should equal the pitch attitude of the aircraft since the altitude is maintained constant. During flight tests with the *Raven* both angles are to be recorded, however no real-time data will be available for the pilot. On the other hand, a separate telemetry system will indicate the aircraft's altitude and airspeed and although it is not going to be that much accurate, it can give the pilot the necessary information to fly approximately level. An important parameter to be kept zero is the bank angle of the aircraft, so that no load factor is introduced in equation (6.3). Since there is no other possibility, this must be achieved through visual contact from the ground. To obtain a lift curve slope, the level flight should be performed for varying angle of attack with the aircraft trimmed for every new value of α . With increasing AOA the accuracy of equation (6.2) will become less as the fixed engine position on the fuselage will create deviations between thrust vector and flight path direction. Since for most of its progression the function of lift coefficient with α is linear, the values obtained at lower AOA can be used to determine the lift curve slope.

Secondly, for drag determination, besides the above mentioned parameters, the aircraft's speed is also to be maintained constant in order thrust and drag forces to be balanced as stated in equation (6.1). Indications from the telemetry system should be used for pilot assistance so that the aircraft remains trimmed at the chosen angle of attack. To determine the function of drag coefficient with α , this manoeuvre is also to be performed for various angles of attack up to a certain value near the maximum. As explained above for the lift coefficient, increasing the angle of attack causes deviations of the thrust vector from the flight path direction, thus the determined drag will also be affected from this error with its amount being greater at higher values of α .

Although this method offers a relative simple way to obtain lift and drag from known weight and thrust forces, it also has some disadvantages most of them associated specifically with the *Raven* aircraft. These are discussed in the following.

The main disadvantage of this technique applies for drag determination, since thrust forces produced by the engines cannot be precisely measured or predicted at this point. The turbine model presented in Chapter 5 is based on accurate measurements only from static tests however the influence of airspeed was determined by means of modifying performance data from similar engines to the *Raven* ones. This will definitely introduce a certain amount of error in thrust calculations and will thus falsify the results for the aircraft's drag. However, if at some point in the future a precise thrust prediction or measurement is available, one can use this technique with much more accuracy. Another disadvantage concerns the simplifications applied to obtain equations (6.1) and (6.2). By increasing the angle of attack, lift and drag forces defined respectively normal and parallel to the flow direction, will retain their orientation to the flight path, however this will not be the case for the thrust vector because of the engines' fixed position on the fuselage. Hence, at high angles of attack equations (6.1) and (6.2) will not accurately represent the force distribution in horizontal and vertical direction. A possible way to avoid this error is to take into account only the appropriate thrust component in the considered direction by correcting the total thrust with the angle of attack. And last but not least, at this point the measuring systems of the aircraft do not allow for any real-time information regarding angle of attack or pitch attitude, hence these parameters cannot be monitored during flight tests leaving them to the pilot's judgement. However, since the main goal is to obtain a function of lift and drag coefficients with α , no precise knowledge of the AOA value is needed during the tests, important is that the aircraft is in an trimmed condition with the angle of attack held constant at the same time.

To conclude, the steady level flight method is appropriate only for lift coefficient determination, since thrust produced by the aircraft's engines cannot be measured or predicted accurately at this point. Experiments to obtain thrust curves at low speeds are planned during the car top testing, which could be able to improve the thrust model presented in Chapter 5 and reduce possible error in drag coefficient determination from this technique. Since no complete results are available at this time, it is recommended that the steady level flight is used to determine a function of lift coefficient with α and by combining this with information about the aircraft's drag polar obtained from another method one can calculate the drag coefficient versus angle of attack. This is presented in detail in the following section.

6.1.2 Drag polar determination from a steady glide

To determine the aircraft's best climb and descent performance test engineers use a method called *sawtooth climb*, named so because of the shape of the aircraft's flight path the

alternating climbs and descents produce. **Ward 2006a** (p. 56) describes the sawtooth climb method as series of timed climbs over a certain altitude band, each performed at different constant speed. The altitude band ΔH defines a chosen nominal test altitude for which the rate of climb is plotted against varying speed to determine its maximum. By putting together plots for different nominal altitudes one can determine the speed for best rate of climb for each altitude. Other parameters usually obtained from climb performance tests include minimum time and minimum fuel to altitude and maximum climb angle. One can also perform series of timed descents to determine the aircraft's best descent performance, which is as well an important quality, especially in emergency situations like rapid cabin decompression at high altitudes where the best rate of descent becomes a key factor. Another possibility is to perform gliding flights at different constant speeds with no thrust exerted on the aircraft, where several parameters like lift and drag coefficients, angle of descent, and lift-to-drag ratio can be calculated from the rate of descent (ROD). These offer a practical and relative easy to perform technique to obtain the aircraft's drag polar and are therefore a subject of thorough discussion in this section.

A steady glide method is described in detail by **Meins 2001** as part of the results evaluation from flight tests with a Cessna 172 and a Piper Archer aircraft performed during practical exercises at the Department of Automotive and Aeronautical Engineering of Hamburg's University of Applied Sciences. The test procedure presented in the following is based mainly on information from this work with some additional data correction methods suggested in other references which are fully acknowledged in the course of the text.

Test procedure

The series of gliding flights are performed for a range of constant speeds at an altitude band ΔH bracketing the nominal pressure altitude chosen before the start of the test. The altitude band is to be defined so that timing can be carried out precisely, for example if this is performed manually with a stopwatch. In the *Raven* case time is recorded with a GPS device reducing possible measurement errors, however, due to the limited endurance of the aircraft the altitude band should be chosen as small as possible to allow for a greater range of constant speeds to be flown during one test. A typical altitude band used by **Meins 2001** (p. 69) in the Cessna 172 and a Piper Archer flight tests is between 800 and 1000 ft (approx. from 240 to 300 m). These basic definitions are illustrated in **Fig 6.2**. The altitude band is shown between the lines described with 1 and 2 which give the actual boundaries of the flight test and are included later in the results evaluation process.

To perform a gliding flight the aircraft is first climbed to an altitude mildly above the pre-determined altitude band ΔH . When the flight path reaches its highest point engine power is reduced to idle and the aircraft begins to glide. Speed is to be maintained constant very precisely with inputs on the controls whereas deviations should not exceed ± 1 knot (approx.

0,5 m/s). For this purpose speed indications from the telemetry system can be utilised for pilot assistance. On the other hand, one can also use its altitude indications to determine the start and end altitude of the steady glide since data from the Pitot-static system cannot be converted into pressure height until after the flight test in the results evaluation process. Normally, timing should start at least 100 ft (approx. 30 m) before entering the targeted altitude band and stop 100 ft after reaching its lowest boundary. Since this is carried out by a GPS device throughout the entire flight envelope, in the results evaluation afterwards only the period between Point 1 and Point 2 should be taken into account with timing intervals and altitude indications for every 100 ft. This procedure is to be performed for a variety of constant speeds with intervals of around 5 m/s for the same altitude band. If the test area allows it, each flight should be conducted in approximately the same air mass (Ward 2006a, p. 57).

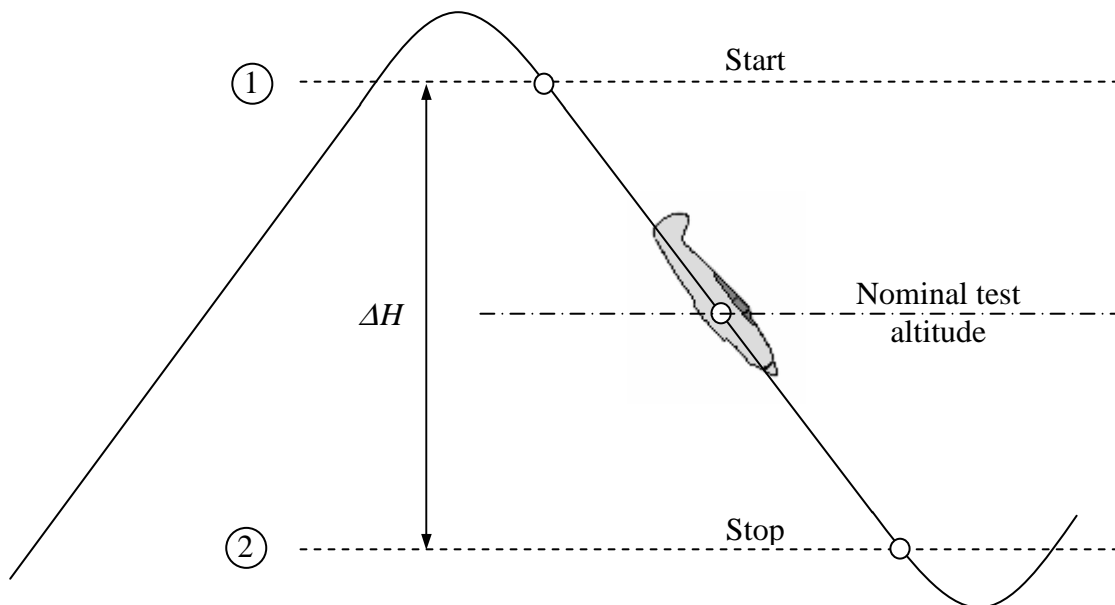


Fig. 6.2 Steady glide illustration (Sawtooth climb segment)

Governing equations and calculation sequence

The mathematical model described in Chapter 3 represents an aircraft's motion during basic flight operations and can also be adopted for a steady glide with certain elements taken into consideration. Since both the thrust produced from the engines and the acceleration along the flight path are approximated as zero, equation (3.33) can be further simplified by neglecting these parameters and substituting the aircraft's weight with lift corrected with the cosine of the flight path angle, as stated by equation (3.34). This yields the following relationship between lift and drag for a steady glide:

$$-D - \frac{L}{\cos \gamma} \sin \gamma = 0 \quad (6.5)$$

A further simplification of this equation can be made by introducing the lift-to-drag ratio E and combining the terms containing the flight path angle γ :

$$E = -\frac{1}{\tan \gamma} \quad (6.6)$$

Hence, in a steady glide the lift-to-drag ratio can be obtained directly from the flight path angle. The minus sign in equation (6.6) denotes the mathematically correct negative value of γ in a descent, which is adopted in further analysis regarding rate of descent calculations from the (negative) change of altitude with measured time. This approach differs from the one described by **Meins 2001** where the flight path angle is considered positive changing the algebraic sign of equation (6.6).

To obtain lift and drag coefficients for every gliding flight performed at a different constant speed first it is necessary to calculate the flight path angle using the rate of descent determined from measured altitude changes and time period between Point 1 and Point 2. The calculation sequence presented in the following describes the data handling for one gliding flight, which is then to be carried over for all the rest. With no effects of gusts considered the rate of descent or the vertical component of the airspeed can be expressed as the change of height with respect to time (**Young 2001**, Chapter 5, p. 29):

$$ROD = -\frac{dH}{dt} = -V \sin \gamma \quad (6.7)$$

However, this theoretically simple geometric relationship introduces some difficulties when applied in flight test calculations since these are influenced by non-standard atmospheric conditions regarding airspeed and altitude measurement and by changes in gross weight during tests due to fuel consumption. Consequently, the measured rate of descent is to be corrected for temperature deviations, acceleration factors and non-standard weight. This procedure is subject to thorough discussion later in this section. Furthermore, each gliding flight is performed at a different constant speed, however, this concerns the indicated airspeed monitored during the test, not the true airspeed V given in equation (6.7). With decreasing altitude and thus increasing relative density, the true airspeed will also slightly decrease at constant indicated airspeed. On that account an average true airspeed is to be obtained for every gliding flight which is then applied in further calculations. Usually an ASI is used for

airspeed indications, which are monitored by the flight test team during performed manoeuvres applying control inputs if necessary. This way the indicated airspeed is the one maintained constant, as is in the case described by **Meins 2001**. However, during tests with the *Raven* aircraft the only real-time speed indications come from a separate telemetry system which does not use pressure measurements from the Pitot-static system and thus does not show the indicated airspeed that is later to be corrected for instrument and position error and used to calculate V . This may introduce some difficulties when evaluating test results afterwards. Therefore, an easy way to obtain the average true airspeed of the aircraft during a gliding flight between Points 1 and 2 is simply to calculate the instrument corrected airspeeds from equation (4.9) for every recorded step, then obtain calibrated airspeed values by applying corrections for position error, and finally determine V using relative density data:

$$V = \frac{V_C}{\sqrt{\sigma}} \quad (6.8)$$

Both calibrated airspeed and relative density can be calculated for every recorded step, however, due to the high frequency of data recording one could take only values for every 20-30 m of altitude change. Using equation (6.8) the respective true airspeeds can be obtained and then averaged for the range of recorded steps. The relative density σ is in this case the ratio of the actual density to the ISA value at MSL, not the relative density corresponding to the pressure altitude found in ISA tables. To calculate σ , first for the relevant pressure altitude a relative pressure δ is obtained from equation (3.8) or taken from **Table A.1**. Then, the relative temperature θ is calculated from equation (3.11) using the actual measured temperature and finally σ is obtained from the ratio of δ to θ (Equation of State). With a known average true airspeed for one glide, the flight path angle can be obtained from the following equation. The calculation sequence for the corrected rate of descent is described later in this section when data correction methods are presented.

$$\gamma = \arcsin\left(-\frac{ROD_{\text{corr}}}{V_{\text{avg}}}\right) \quad (6.9)$$

Consequently, with the flight path angle known, one can calculate a lift coefficient by substituting the lift force in equation (3.22) with a term containing the aircraft's weight, as given in equation (3.34), and by taking the true airspeed to be the average one obtained above. This manipulation yields the following formula for C_L :

$$C_L = \frac{2W_{\text{avg}} \cos \gamma}{\rho V_{\text{avg}}^2 S_{\text{ref}}} \quad (6.10)$$

During a single flight test the aircraft's weight will decrease due to fuel consumption giving the need for a nominal weight value in equation (6.10). For correction of data collected from a sawtooth climb technique **Ward 2006a** uses an average weight calculated for the series of climbs performed during one flight test. This method differs from the calculations presented by **Meins 2001** where the maximum take-off weight (MTOW) is of particular interest and is used to obtain the aircraft's drag polar. **NavAir 1992** and **Kimberlin 2003** offer a similar approach for this problem where the term "standard weight" is used for data corrections describing a pre-determined nominal weight for which tests results are to be obtained. In this work the average weight correction is utilised for the steady glide method, however, if a certain nominal weight is targeted for flight tests, for example MTOW, the above given references should be consulted for alternative solutions, in particular **Meins 2001**.

Another parameter in equation (6.10) that will not remain constant during a gliding flight is the air density. With decreasing altitude air gets thicker slightly increasing the value of ρ throughout the glide. Therefore, density at the nominal pressure altitude is used to obtain aerodynamic forces. For a measured barometric pressure and air temperature at this altitude, ρ can be calculated from equation (3.5).

With the flight path angle known, one can also calculate the lift-to-drag ratio from equation (6.6) and then use it to obtain the appropriate drag coefficient with the value of C_L :

$$C_D = \frac{C_L}{E} \quad (6.11)$$

The above presented calculation sequence is applied for all constant speed glides performed during the test giving a pair of lift and drag coefficients for every single glide. Normally, at low Mach numbers these do not vary with changes of V , however, in this case speed is maintained constant with elevator inputs altering the aircraft's angle of attack throughout the flight and thus introducing an apparent airspeed dependency. On that account one can conclude that the values for lift and drag coefficient obtained from a steady glide method do not give any information regarding their function with changing AOA and can be used only to determine the aircraft's drag polar. This is done by utilising the mathematical model given from equation (3.30) in Chapter 3 where C_D is assumed to be a square function of C_L . By plotting lift versus drag coefficient one can determine a parabolic function and then further improve its smoothness applying the MS Excel tool "Trendline". The intersection of this curve with the C_D -axis yields the parasite (zero-lift) drag coefficient C_{D_0} (see **Fig. 3.3**).

A different approach can be made to obtain the Oswald efficiency factor e by plotting C_D against the square of C_L . According to equation (3.30) this should yield an approximately linear function which can also be adjusted using "Trendline". By taking the derivative with

respect to the square of C_L one can determine the curve slope. Due to the linear dependency all differentials are replaced with finite differences giving the curve slope as:

$$\frac{\Delta C_D}{\Delta C_L^2} = \frac{1}{\pi A e} \quad (6.12)$$

Hence, the reciprocal of e can be determined by multiplying the calculated curve slope with π and the wing aspect ratio A . Using this approach it is also possible to obtain the parasite drag coefficient by taking the value of C_D at zero lift. However, it is most likely that this value differs slightly from the previously calculated one due to the fact that both curves are obtained using the tool “Trendline” which extrapolates measured data differently depending on the type of mathematical function required (in this case linear or square).

Data corrections

As already discussed several times in the past chapters, recorded data during flight tests need to be reduced to a common baseline where effects due to changes in atmospheric properties and weight are standardised. First of all, since the atmospheric conditions on a test day will probably vary from the ISA model presented in Chapter 3, corrections of collected data are to be made for deviations from non-standard conditions of two basic parameters – barometric pressure and air temperature. Pressure corrections normally apply for powerplant performance and altitude measurements, however, in a steady glide, no thrust forces are considered and their corrections are therefore left out in further discussions. On the other hand, altitude corrections can be avoided by setting the altimeter to standard mean sea level pressure (1013 hPa) during tests, so that altitude measurements are automatically referenced to standard conditions. In the *Raven* case pressure altitude is calculated using the appropriate ISA equations, hence altitude corrections for pressure deviations are also not subject to discussion in this section. Non-standard temperature variations also effect both powerplant and altitude data. Deviations from the ISA values may occur due to a non-standard temperature lapse rate or due to a warmer (or cooler) surface temperature with a standard lapse rate (**Ward 2006a**, p. 65). In the latter condition, during a descent air density deviations from the standard values will reflect in a different change of potential energy than one given for ISA conditions. On the other hand, a non-standard temperature lapse rate introduces an apparent acceleration affecting measured true airspeeds. However, this method is not adopted here instead a similar correction for occurring acceleration is used. If this particular correction is required in future work, **Ward 2006a** should be consulted.

Secondly, data collected from a sawtooth climb method requires a correction for changes in gross weight. For a set of climbs and descents the aircraft’s weight would decrease with time

due to fuel consumption making each manoeuvre performed at different weight. Hence, recorded data should be standardised to a nominal value giving the need for a precise measurement of the aircraft's actual weight at each point during flight operation. This can be achieved either by assuming that the rate of descent varies linearly with time due to changes in weight or by calculating the actual weight of the aircraft using fuel flow rate measurements. In the first case, by repeating a descent with the same parameters at the end of the test, one can obtain new data, which is then used to establish the linear dependency with time. Since fuel flow rate measurements are available in the *Raven* case, its exact weight at any time during tests can be calculated. Apart from corrections for non-standard weight, other typical data reduction methods include also corrections for occurring acceleration and effects of vertical wind gradients. Their application is discussed in the course of the text.

In the results evaluation process first recorded data is filtered and synchronised and then parameters like calibrated airspeed and pressure altitude are calculated and corrected for instrument and position error using the appropriate equations. To obtain a rate of descent the recorded altitude band ΔH at which the glides were flown and the time for their performance (between Point 1 and Point 2) have to be extracted for each constant speed. In further calculations not corrected values obtained from measurements in test day conditions will be denoted with the index "t". The first correction made to the recorded altitude band is for non-standard temperature deviations, where the temperature lapse rate is assumed to be the same as on a standard day. However, due to a warmer (or cooler) surface the change of potential energy expressed in altitude terms is different on a non-standard day which causes deviations in the measured altitude band. **Fig. 6.3** below shows the altitude band for a measured difference in pressure for both standard and non-standard surface temperature.

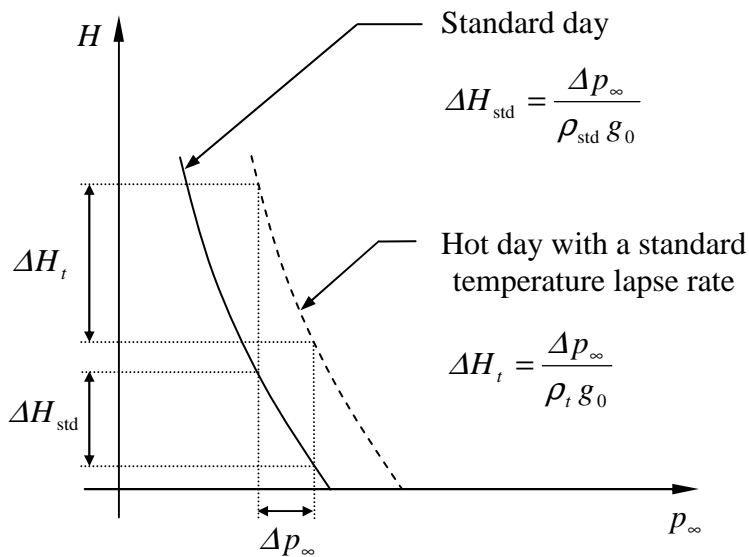


Fig. 6.3 Changes of altitude for measured ambient pressure difference

Taking this information into account and making use of the Equation of State, the correction for non-standard temperature can be simplified to the following relationship where the index “temp” denotes the altitude increment at standard day conditions corrected for temperature deviations and replaces the “std” used in **Fig. 6.3**:

$$\Delta H_{\text{temp}} = \Delta H_t \frac{T_{\text{std}}}{T_{\infty,t}} \quad (6.13)$$

Hence, the altitude band recorded in test day conditions is to be multiplied by the ratio of standard temperature, taken from ISA tables, to measured test day temperature which on a hot day reduces the recorded value. According to **Ward 2006a** (p. 66), both temperatures apply for the nominal pressure altitude at which the glides are performed. This is contradictory to the correction method described by **Meins 2001** (p. 71) where first the reciprocal ratio is used and second – the temperature values are given for sea level conditions. In this work the first method is adopted since it offers a straightforward explanation of the physics behind the effects of non-standard temperature deviations on changes of potential energy.

A second correction to the altitude band is to be made for an occurring acceleration during the glide. With decreasing altitude the values for relative density become greater, thus at constant indicated speed the true airspeed is reduced throughout the glide. Mathematically this can be expressed as an acceleration factor in the governing equations. **Meins 2001** uses an energy approach to calculate the altitude difference caused by this effect. Since the aircraft’s total energy remains constant, a decrease in its kinetic energy, expressed in a smaller value of V , produces an increase of its potential energy, expressed in a greater value of H . The indices “1” and “2” denote the values for airspeed at respectively Point 1 and Point 2.

$$mg\Delta H = \frac{1}{2}m(V_2^2 - V_1^2) \quad (6.14)$$

Hence, in this case the altitude difference ΔH on the left hand side of equation (6.14) is negative reducing the absolute value of the corrected for temperature deviations altitude band. However, since the altitude band was taken to be negative, to express this mathematically correct ΔH has to be subtracted from the previously calculated altitude band. As already mentioned in this section, this differs from the calculation sequence presented by **Meins 2001**, since the altitude band there is taken to be positive. Solving equation (6.14) for the altitude difference and introducing it as a correction factor yields:

$$\Delta H_{\text{acc}} = \Delta H_{\text{temp}} - \frac{V_2^2 - V_1^2}{2g} \quad (6.15)$$

The last correction mathematically presented in this section applies for non-standard weight deviations. The effects of wind gradients are discussed briefly in the last paragraph, however no direct calculation sequence is given. There exist several methods to correct recorded data for changes in gross weight, the simplest one being by applying the ratio of a measured weight at the nominal test altitude during the glide to the average weight for the complete flight test. This correction is shown below:

$$\Delta H_{\text{cor}} = \Delta H_{\text{acc}} \frac{W_t}{W_{\text{avg}}} \quad (6.16)$$

One of the main disadvantages of such correction is that it ignores changes of induced drag due to decrease of weight. However, it is easy to use and provides results that differ only slightly from ones obtained with more sophisticated methods (**Ward 2006a**, p. 57). These include terms for induced drag correction and require knowledge of the aircraft's Oswald efficiency factor e which in the *Raven* case is available only from preliminary design calculations at this point. Therefore equation (6.16) is utilised for non-standard weight corrections completing the calculation sequence for the altitude band.

With the corrected altitude band between Point 1 and Point 2 and the time needed for the aircraft to glide, one can calculate its rate of descent corrected for various non-standard conditions as follows:

$$ROD_{\text{cor}} = -\frac{\Delta H_{\text{cor}}}{\Delta t} \quad (6.17)$$

Finally, changes in wind speed and direction should also be taken into account, if necessary, when calculating rates of descent. Particularly vertical wind speed gradients could cause variations of airspeed expressed mathematically in terms of an acceleration factor. This introduces some difficulties in practical calculations, since wind gradients are subject to constant changes. Equations to determine an acceleration factor caused by occurring vertical wind speed gradients are given by **Ward 2006a** (p. 58), however these are not adopted in this work due to their requirement for knowledge of wind speed changes with altitude. On the other hand, by performing flight tests in a certain manner, these effects could be minimised to a negligible level. One option to do this is by flying the aircraft almost perpendicular to the pre-determined wind direction. Alternatively, performing manoeuvres in opposite headings could eliminate wind effects, unfortunately this would also increase the required time and the costs planned for the flight tests.

Summary

The above described technique offers a relative simple way to obtain the aircraft's drag polar from flight tests. Combined with the steady level flight method given in the previous section of this chapter, one can determine a function of the drag coefficient with varying angle of attack without having to rely on engine thrust modelling. If a function of lift coefficient with α is obtained using information regarding the aircraft's weight during a steady level flight, the drag polar determined with this technique can be used to calculate drag for the lift values at a known AOA, thus one can indirectly obtain a function of drag coefficient with angle of attack. The most important parameter to be held constant during a steady glide is the aircraft's speed. Since no ASI is available at this point, indications from the telemetry system will be the primary reference for speed control. However, the actual values of indicated airspeed are not of particular interest when tests are performed for drag polar determination, therefore indications from the telemetry systems do not need to be synchronised with the airspeeds calculated from Pitot-static system data. Measured pressure and temperature are to be corrected for occurring errors using the calibration curves obtained from previous tests. True airspeeds should be calculated for suggested altitude steps of 100 ft (approx. 30 m) and then averaged to one value used later to obtain the flight path angle and lift coefficient. For this purpose a relative density is required at every level, thus pressure and temperature values are also to be calculated for these steps. The further calculation order for reduction of data collected from a steady glide method is summarised in **Table 6.1**. This is valid for one constant speed glide only and is to be repeated for all the rest. At the end one should have lift and drag coefficients for every airspeed tested, which are afterwards plotted against each other to obtain a drag polar and an Oswald efficiency factor

Table 6.1 Steady glide data reduction sequence

<i>Step</i>	<i>Calculate</i>	<i>From</i>
1	P_{ic}	Equation (4.6)
2	T_{ic}	$\vartheta_{ic} + 273,15$
3	h_p	Equations (4.11) and (4.12) with #1
4	ΔH_t	Values of #3 for the targeted Points 1 and 2
5	δ	Equation (3.8) or Table A.1 for values of #3
6	θ	Equation (3.11) with values of #2
7	σ	#5 ÷ #6
8	V_C	Equations (4.9) and (4.10)
9	V	#8 ÷ $\sqrt{\#7}$
10	V_{avg}	Average all values of #9

Table 6.1 Steady glide data reduction sequence (continued)

<i>Step</i>	<i>Calculate</i>	<i>From</i>
11	ΔH_{temp}	Equation (6.13) with T_{std} and #2 at the nominal pressure altitude
12	ΔH_{acc}	Equation (6.15) with #11 and values of #9 for Point 1 and 2
13	W_{avg}	Average weight values at the start and at the end of the flight test
14	W_t	Fuel flow rate and the period of time until nominal test altitude
15	ΔH_{cor}	Equation (6.16) with #12, #13 and #14
16	ROD_{cor}	Equation (6.17) with #15 and the time period Δt between 1 and 2
17	γ	Equation (6.9) with #16 and #10
18	E	Equation (6.6) with #17
19	ρ	Equation (3.12) with #7 at the nominal pressure altitude
20	C_L	Equation (6.10) with #10, #13, #17 and #19
21	C_D	#20 \div #18

Like the steady level flight technique, this method also has several disadvantages. First, in the governing equations thrust was assumed to be zero, which is not exactly accurate for gas turbines like the *Raven* ones. With the thrust lever on idle position a small thrust force is produced which could falsify obtained results. Another disadvantage in the *Raven* case is the short flight operational time available for tests. Since for every glide a climb to the initial altitude is required, the limited endurance of the aircraft might result in limited number of constant speeds tested. Thus, with only few values of lift and drag coefficients available the extrapolation of the drag polar with “Trendline” could introduce small errors. And finally, in Chapter 3 aerodynamic forces were assumed to be independent of changes in thrust, however, this is not precisely true since inlet flows and engine jet stream have a small influence on the surrounding airflow field. The resulting pressure distributions affect both lift and drag forces, so that the drag polar determined from steady glides with engines working on idle might differ slightly from the one present at high engine speeds.

6.1.3 Stall speed and maximum lift coefficient

At high angles of attack and approaching stall speed the steady level flight method described previously in this chapter becomes inaccurate due to an increasing thrust force component perpendicular to the flight path direction. As already discussed, the simple drag polar model used in the steady glide technique is also inappropriate at high values of α , thus the non-linear area of the function of lift coefficient with angle of attack cannot be determined

precisely from the methods presented so far. Generally, this section deals with ways to obtain the aircraft's stall speed and a resulting maximum lift coefficient from flight tests, as well as with the required data reduction sequence applied for non-standard conditions.

In Chapter 3 lift coefficients were assumed to be a function of angle of attack only, however, the non-linear area is also affected by the local flow characteristics resulting in additional Reynolds number dependency for incompressible flows. This can be seen in wind tunnel test results for classical NACA-aerofoils where curves at different values of Re are plotted. Their progression starts to vary at high angles of attack increasing the lift coefficient at greater values of Re . In Reynolds number calculations a characteristic length is needed, whose value is not directly expressed by a physical law and is usually chosen by convention. For an aircraft this is taken to be the wing's MAC, hence Re can be calculated from

$$Re = \frac{\rho V \bar{c}}{\mu} \quad (6.18)$$

The air density is obtained using test data for pressure and temperature at the appropriate altitude. On the other hand, the dynamic viscosity can be calculated from SUTHERLAND's law where it is given as a function of air temperature only. There exist several variations of this law differing slightly in their constants and reference values. In this work the version given by **Scholz 2002** (p. 8) is adopted, where the value of measured temperature is in Kelvin and the resulting dynamic viscosity in $\text{kg}/(\text{m} \cdot \text{s})$:

$$\mu = 1,458 \cdot 10^{-5} \frac{T^{1,5}}{T + 110,4} \quad (6.19)$$

An obtained Reynolds number has no direct influence on further calculations regarding the maximum lift coefficient, however, it is an important parameter to be taken into account when comparing results. Since during subscale flight tests the values of Re are expected to be considerably lower than ones supposed to be flown with a full-sized aircraft, the obtained results for $C_{L, \max}$ will not be representative.

To obtain the aircraft's stall speed in flight, **NavAir 1992** (p. 3.32) gives a so-called power-off gradual deceleration technique. The chosen altitude for the test has to be sufficient for the pilot to gain control after the aircraft has been stalled without endangering its safety. First the aircraft is trimmed in a steady level flight at a speed approximately 1,2 times the predicted stall speed, then the engine power is reduced to idle. The angle of attack is slowly increased until the stall occurs with the pilot using pitch control inputs to adjust a deceleration rate of not more than 0,5 kts/s. This is necessary to achieve a steady state stall speed not influenced

by non-steady flow effects due to rapid deceleration. Usually, a stall is indicated by a nose pitch down and the aircraft beginning to plunge down. Afterwards thrust power from the engines is increased and the aircraft is brought to a steady state. **Kimberlin 2003** (p. 48) gives a value of 1 kt/s for the deceleration rate, which has to be achieved by the time the aircraft reaches a calibrated airspeed of 1,1 times the calibrated stalling speed. This information is based on FAA regulations concerning Part 23 aeroplanes. A similar test procedure to the one described above is given also by **Meins 2001** (p. 87), however, no values for trim speed and deceleration rate are specified.

Normally, stall speed tests with a forward centre of gravity position are not hazardous and do not endanger the overall safety, however, if these are performed for the first time on a new aircraft design, one should take the necessary precautions. In case of subscale flight testing, like the *Raven* one, no additional safety equipment is required, therefore the only aspect to be considered is the aircraft's altitude. At first, the maximum altitude planned for flight tests can be adopted to ensure the pilot has enough time to restore the aircraft's steady state motion. Another aspect to be considered is the aircraft's speed measurement. The stall speed cannot be obtained by observation since no airspeed indicator is available. However, using data from the Attitude and Heading Reference system regarding pitch attitude, one can determine the moment when the aircraft's nose starts to pitch down. On the other hand, one can also use altitude information calculated from static pressure data to establish the moment when the aircraft itself begins to plunge down losing its altitude. Once this point in time is determined differential pressure data from the static and total pressure ports should be converted into a corrected for instrument and position error airspeed utilising equations (4.9) and (4.10). This airspeed indicates the calibrated stall speed of the aircraft for test conditions, $V_{S,t}$.

Once the test stall speed is obtained, it needs to be corrected for non-standard conditions. Both **NavAir 1992** and **Kimberlin 2003** give data reduction sequences for corrections regarding weight, deceleration rate and centre of gravity position. According to the latter one, the FAA requires stall speed measurement tests to be conducted "at maximum take-off gross weight at the most forward centre of gravity" (p. 47). In general, this yields the highest value of stall speed obtainable, which is then published in flight manuals and pilot's operating handbooks providing the crew with a certain amount of safety, since normally for other conditions the stall speed will have lower values. Due to fuel consumed from take-off to the required altitude where stall speed tests are conducted, the aircraft's weight will not match the maximum take-off weight. Using fuel flow rate indications and the time period between take-off and performed test, one can calculate the current aircraft weight and use it to correct the obtained stall speed as given below:

$$V_{S,MTOW} = V_{S,t} \sqrt{\frac{m_{MTOW}}{m_t}} \quad (6.20)$$

Further corrections given by **Kimberlin 2003** (p. 50) can be made for a deceleration rate greater than 1 kt/s and for incorrect centre of gravity position. Such corrections are described as practical for results evaluation, if these two test parameters do not match the desired ones, however, they are not accepted as valid by the FAA and cannot be utilised for regulations fulfilment. For a light aircraft like the *Raven* a deceleration rate of 1 kt/s should not be difficult to obtain prior to reach 110 % of the stall speed. On the other hand, the primary purpose of flight tests at this point has pure experimental nature with no requirements from aviation authorities to be met. Therefore the deceleration factor correction is not considered in this work and only the centre of gravity correction is adopted. The mathematical expression of this method is presented further below in equation (6.22). If corrections for deceleration rate are required in future tests, the above given source is to be consulted.

With a calibrated stall speed obtained, the respective maximum lift coefficient can be calculated by rearranging equation (3.27), given in Chapter 3, and substituting the maximum take-off weight values for stall speed and aircraft weight. One can also use the test values of these parameters, since mathematically they represent the same ratio, as stated by equation (6.20). Hence, for the maximum lift coefficient the following relation is valid:

$$C_{L, \max} = \frac{2m_t g}{\rho_0 V_{S,t}^2 S_{\text{ref}}} \quad (6.21)$$

If tests are performed with an incorrect or undesired centre of gravity position, it is possible to make a correction afterwards by adjusting the aircraft's speed for changes in tail down load. After the stall speed is corrected for non-standard weight using equation (6.20), a lift coefficient is calculated with equation (6.21) and then modified as follows:

$$C_L = C_{L,t} \left[1 + \frac{x_{c.g.} - x_{c.g.,t}}{l_{\text{tail}}} \right] \quad (6.22)$$

The parameters indicated with “*t*” denote the previous values for which the correction is made although the lift coefficient is obtained not directly from test measurements but from the non-standard weight corrected airspeed. Both centre of gravity positions in equation (6.22) are given as the direct distance along the aircraft's longitudinal axis from a certain reference point, for example the nose tip. Usually in aviation literature the CG position is presented in percentage of the mean aerodynamic chord. If this is the case, equation (6.22) has to be modified by multiplying the difference of the *x*-values with MAC and dividing it by 100. The tail length is assumed to be the distance from ¼ chord of the wing to ¼ chord of the horizontal stabiliser. Obtained like this, the new lift coefficient is representative for the desired centre of gravity position and is to be converted back to stall speed.

Finally, to ensure that valid data is used for stall speed determination, tests should be conducted multiple times. According to **Kimberlin 2003** (p. 49), at least five stalls should be performed and for each of them a calibrated speed corrected for non-standard conditions is to be calculated. Only on this basis enough statistical data is provided to obtain valid results for a given configuration. Since the stall speed value varies with changes in the wing configuration due to flap deflection, these set of stalls are to be repeated for different flap settings including these at take-off and landing configuration.

6.2 Longitudinal static stability

An aircraft regarded as a rigid body has six degrees of freedom, three translations and three rotations about its body axes, and thus requires six equations to fully describe its motion in the surrounding air. These enable further analysis of the aircraft's dynamic behaviour and response to a disturbance in pitch, roll or yaw, providing engineers with information on its overall stability. Depending on the degrees of freedom and motions considered, one can divide the aircraft's stability into *longitudinal* and *lateral-directional* stability. These are the result of two general types of motion each defined by three of the above mentioned equations. A longitudinal motion takes place in the aircraft's plane of symmetry and is characterised with a forward and downward translation (respectively along the longitudinal x and vertical z axis) and a pitch rotation (about the lateral y axis). On the other hand, a lateral-directional motion involves rolling and yawing rotations about respectively the x and z axes and a translation along the y axis. For most conventional designs both stability concepts can be studied independently providing accurate solutions to the aircraft's overall response following a disturbance. A further classification divides stability analysis into *static* stability, where forces and moments are taken to arise due to the displaced position of the aircraft, and *dynamic* stability, which is concerned with forces and moments that arise due to velocities and accelerations (**Young 2001**, Chapter 11, p. 2).

The remaining sections of this chapter deal with aircraft static stability and the possibilities for its analysis from flight testing. First, the concept of elementary longitudinal static stability is presented with simplified equations and conditions defining the state of equilibrium and the static margin for a conventional aircraft configuration, which are then further developed into a flight test method to determine the neutral point and the change of pitching moment coefficient with varying lift coefficient. For such basic analysis to be conducted several simplifications have to be made concerning the aircraft geometry and the aerodynamic and thrust forces generated. These include disregarding compressibility effects and deformations of the airframe structure due to aeroelasticity. On top of all, control surfaces are taken to have linear characteristics and the aircraft is assumed to be operating in a steady level flight well above its stall speed within the linear area of the lift curve slope, thus all aerodynamic force and moment derivatives are constants.

6.2.1 Trim equation and static margin

The concept of occurring pitching moment due to pressure and shear stress distributions on the aircraft surface was briefly described as part of the theoretical background on aerodynamic forces given in Chapter 3. It was defined about the centre of gravity of the aircraft with a mathematical expression given in dimensionless form by equation (3.28). According to NEWTON's first law, for an aircraft to be in a steady level flight the sum of all forces acting on its body and the moment about its CG have to be zero. This differs from the approach made in section 6.1.1 where the aircraft was defined as a mass point with all forces acting in its centre of gravity. In longitudinal stability analysis forces are taken to act at different locations of the aircraft's surface requiring a second condition in order the aircraft to be in a state of equilibrium, also known as "trim".

Normally, aerodynamic forces generated by the wings will not act precisely at the aircraft's centre of gravity and will thus produce a moment that usually tends to pitch the nose down depending on the CG location. Conventional aircraft configurations use a downward force created by the tailplane to compensate for this moment and to establish the state of trim. For an aircraft to be statically stable, "... following a small disturbance in pitch, a moment must be produced which tends to restore the aircraft to the trimmed condition" (Young 2001, Chapter 11, p. 7). Hence, if for example due to a vertical gust the aircraft's AOA is increased, for positive static stability a negative pitching moment (nose down) is required to reduce the angle of attack. The variation of moment coefficient with C_L can be expressed by a linear function, which for a stable aircraft will have a negative slope (see Fig. 6.4). An increased angle of attack would result in a greater lift coefficient, hence the positive static stability will reflect in a restoring negative pitching moment (area of the linear function below the horizontal axis). In order the aircraft to be trimmed at the new position of higher AOA, an elevator input is needed to produce a greater downward force and balance the moment about the centre of gravity. This would shift the linear function to the right with a higher trim value of lift coefficient, however, the slope will remain the same creating a set of parallel lines for different trim conditions. By extrapolating the line towards the vertical axis, one can determine a moment about the CG at a hypothetical condition of zero-lift (dashed lines on Fig 6.4). This would occur due to non-symmetrical pressure and shear stress distributions and would equal the moment about any reference point, including the aerodynamic centre, defined as the point about which the pitching moment remains constant with changes in AOA. This is a very useful quality, since it allows the resultant aerodynamic force to be assumed acting in the AC with an additional moment about the aerodynamic centre considered.

Variations in the aircraft's centre of gravity position affect its degree of static stability by changing the curve slope of the linear function. Shifting the CG backwards reduces the slope, thus makes the aircraft less stable until it reaches neutral stability at a value of the slope equal to zero. Further aft movement of the centre of gravity makes the aircraft unstable introducing a positive slope. Examples of these variations are shown also in the figure below.

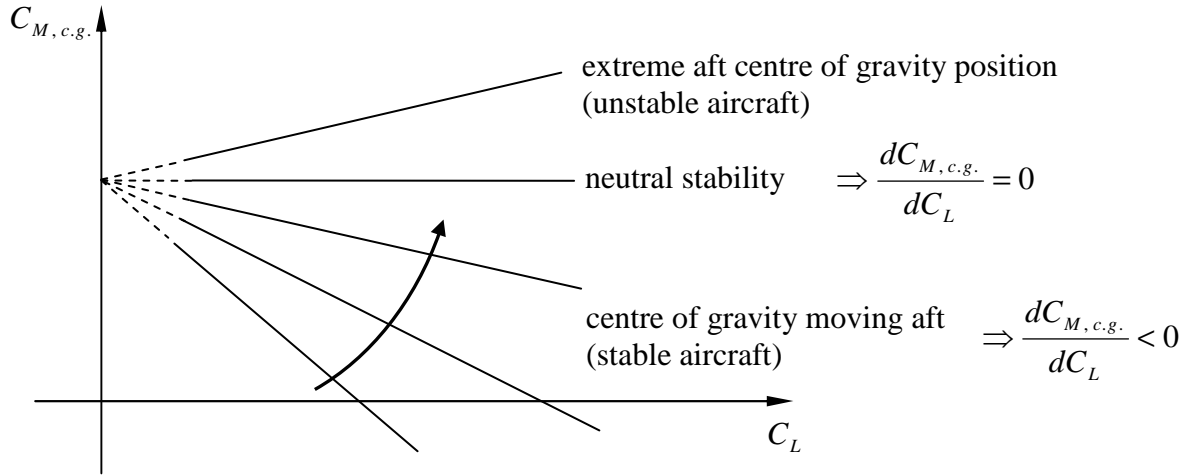


Fig. 6.4 $C_{M,c.g.}$ versus C_L for different centre of gravity positions

For an aircraft regarded as a two-dimensional body in its plane of symmetry a trim equation can be derived considering all forces acting at their appropriate locations and using them to calculate a resultant pitching moment about the centre of gravity. In this work a simplified version, presented later in equation (6.23), is obtained by reducing the aircraft geometry to two parts that generate aerodynamic forces acting in their respective aerodynamic centres – “wing + body” and “tailplane”. The term “wing + body” describes the entire aircraft body less than the tail, including wings, fuselage, engine nacelles, etc. A detailed derivation of equation (6.23) can be found in **Young 2001** (Chapter 11) and is not presented in this work, however, some aspects and assumptions are discussed in the following:

- For small angles of attack lift forces can be approximated perpendicular to the aircraft’s longitudinal axis, thus moment arms are expressed as x -values. This differs slightly from the scheme suggested by **Young 2001** (Chapter 11, p. 18), where all distances are given parallel to the zero-lift line of the aircraft with a separate symbol used. However, simplifications for moment arms along the x axis can be found in most references quoted in this work, including **Kimberlin 2003** and **Ward 2006a**, therefore they are adopted here.
- Moments produced by thrust and drag forces about the centre of gravity are small compared to ones due to lift forces and can be neglected in further analysis.
- The moment about the aerodynamic centre of the tailplane is also negligibly small, hence only one moment is given below on the right hand side of equation (6.23) – the one about the “wing + body” AC.

With all assumptions taken into account the simplified trim equation can be written in its dimensionless form as

$$C_{M,c.g.} = C_{M,a.c.} + \frac{x_{c.g.} - x_{a.c.}}{\bar{c}} C_L - \bar{V} C_{L,tail} \quad (6.23)$$

The index “a.c.” denotes the aerodynamic centre of “wing + body”. The symbol \bar{V} is a summary of all geometric parameters multiplied by the tail lift coefficient. It is called *tail volume coefficient* and is defined as:

$$\bar{V} = \frac{l_{\text{tail}} S_{\text{tail}}}{\bar{c} S_{\text{ref}}} \quad (6.24)$$

The distance between both aerodynamic centres, called the tail arm, is denoted with the same symbol in equation (6.24) as the one used in the previous section of this chapter for stall speed correction regarding incorrect CG position (p. 84). This is a valid approximation since for most classical aerofoils the AC lies around $\frac{1}{4}$ chord length from the leading edge.

Taking the derivative of equation (6.23) with respect to the total lift coefficient yields the following relationship, where the moment coefficient about the AC is dropped since it does not change with varying C_L :

$$\frac{dC_{M,c.g.}}{dC_L} = \left(\frac{x_{c.g.} - x_{a.c.}}{\bar{c}} \right) - \bar{V} \frac{dC_{L,tail}}{dC_L} \quad (6.25)$$

For an aircraft with positive static stability the derivative of moment coefficient with total lift coefficient must have a negative value to produce a restoring moment, as discussed earlier in this section. The slope depends on the centre of gravity position, whereas the aircraft becomes less stable with the CG moving aft (see **Fig. 6.4**). However, at one specific location it is neutrally stable, hence the moment coefficient is independent of changes in lift. This unique position is called the *neutral point* and is defined in dimensionless form as

$$\frac{x_N}{\bar{c}} = \frac{x_{a.c.}}{\bar{c}} + \bar{V} \frac{dC_{L,tail}}{dC_L} \quad (6.26)$$

Furthermore, the resulting dimensionless distance between centre of gravity and neutral point is defined as the *static margin* and can be given in percentage of the mean aerodynamic chord of the wing. In this work it is an expression of the direct ratio of the distance between these points along the longitudinal axis and the MAC:

$$K_N = \frac{x_N - x_{c.g.}}{\bar{c}} \quad (6.27)$$

By substituting both the neutral point and static margin definitions in equation (6.25), one can obtain the following relationship between K_N and the slope $dC_{M,c.g.}/dC_L$:

$$K_N = -\frac{dC_{M,c.g.}}{dC_L} \quad (6.28)$$

Hence, for a stable aircraft the centre of gravity location must be ahead of the neutral point giving the static margin a positive value. If the aircraft possesses neutral stability the CG and the neutral point have the same location on the longitudinal axis, thus the static margin will equal zero. A possible technique to obtain a function of pitching moment coefficient with lift coefficient (and also with AOA for the given linearity) from flight tests is first to determine the neutral point of the aircraft and then use it to calculate the static margin. The precise test description and data evaluation sequence of this flight test method is subject of the next section.

6.2.2 Neutral point determination from flight tests

Before proceeding to a method to determine the neutral point position on the longitudinal axis, first it is necessary to consider the aircraft's control system. Depending on the connection between aerodynamic control surface and pilot control column one can classify reversible and irreversible control systems. The first one describes a system rigidly connected together, hence an input from the pilot will move the control surface and vice versa – if the surface moves, it will cause a reaction at the control column. On the other hand, irreversible control systems use hydraulic or electrical actuators and have no rigid connection between the controls. Therefore, an external movement of the aerodynamic control surface will provide no direct feedback to the control column giving the need for artificial feel devices to assist the pilot. Usually, for an aircraft with such control system the elevator angle will be fixed at a given control column position. For reversible control systems however, if the control column is not held fixed by the pilot, the elevator is free to float. Due to generated aerodynamic forces on the elevator surface a moment about its hinge line is produced, which can be balanced using trim tabs located at the rear section of the elevator. With respect to the stability of the aircraft these two conditions give the so-called *stick-fixed* and *stick-free* longitudinal static stability, for which the neutral point location on the x -axis will be different, and therefore they have to be dealt with separately in further analysis.

The *Raven* aircraft is equipped with a telemetry system for remote control from the ground which utilises electrical actuators to provide the desired deflection of the aerodynamic control surfaces when given an input from the pilot. Hence, the elevator hinge moments are balanced

by actuators holding the surfaces in a fixed position. In such case no feedback is given to the pilot and he or she must rely strictly on visual contact to gain a feel for the aircraft's response to inputs. For this reason, the following longitudinal static stability analysis assumes a stick-fixed condition and the method presented applies for stick-fixed neutral point determination. This is based mainly on information presented by **Young 2001** (Chapter 12) if not stated otherwise, whereas some aspects are slightly modified and denoted with the appropriate nomenclature used in this work. As stated in the beginning of this section, elevators are assumed to have linear characteristics, thus all derivatives are constants.

The *Raven* aircraft has a fixed horizontal stabiliser and therefore pitch attitude is controlled by deflecting its elevators and thus changing their angle relative to the local airflow. This on the other hand changes the lift coefficient of the tailplane and balances the resulting moments about the centre of gravity. Taking into account the above made assumption about the linearity of control surfaces, it can be shown that the elevator angle to trim varies linearly with changes in total lift coefficient. A detailed derivation of this statement can be found in **Young 2001** (Chapter 12, p. 17). The elevator angle to trim is given as the sum of a hypothetical trim angle at zero lift and the lift coefficient multiplied by a constant term, which consists of the static margin, the tail volume coefficient and additional parameters given for the specific airframe geometry. For a fixed aircraft design only the static margin can be modified by changing the centre of gravity position, hence the slope of the linear function depends on the value of K_N . Examples of this dependency are illustrated below in **Fig. 6.5**.

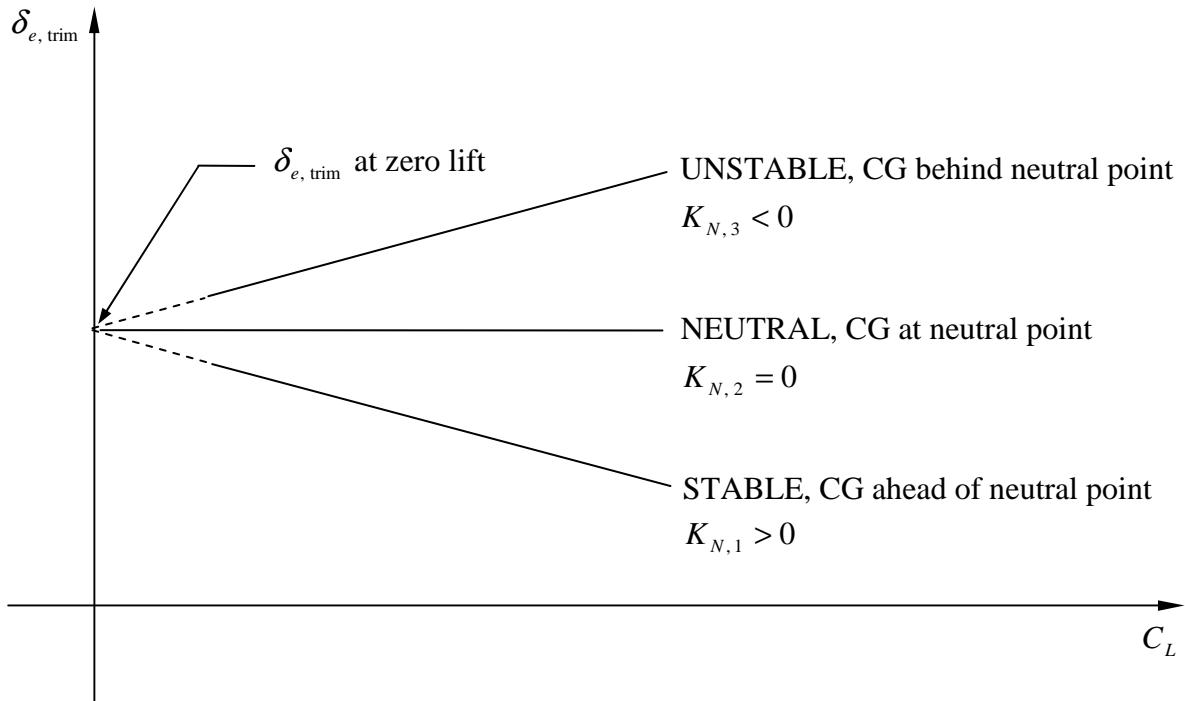


Fig. 6.5 Elevator angle to trim versus C_L for different centre of gravity positions

At a theoretical condition of zero lift all lines will have the same value of elevator angle to trim. Hence, for a neutrally stable aircraft the horizontal line will also intersect the vertical axis at the same point. This simple quality can be utilised to determine the stick-fixed neutral point position from flight tests. The technique consists of the aircraft being flown at two different CG positions denoted below with x_1 and x_2 , which could be chosen safely forward to maintain positive static stability during tests. Using elevator inputs the aircraft is trimmed in a steady level flight for a variety of speeds at both CG positions and the respective elevator angles to trim are recorded. Then, for every trim angle a lift coefficient is determined, as described in section 6.1.1 for the steady level flight method. Finally, these are plotted to obtain a linear function for each CG location, as shown in the figure below:

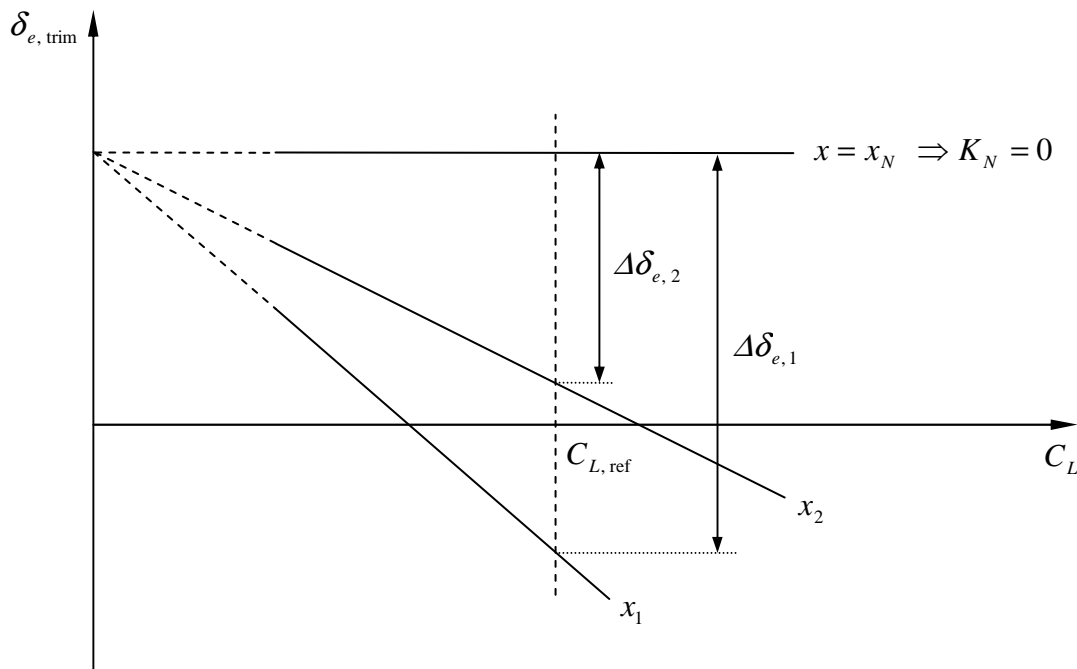


Fig. 6.6 Elevator angle to trim versus C_L for two CG positions flown

When extrapolated to the vertical axis, both lines intersect at the hypothetical elevator trim angle at zero lift. Through this point a horizontal line should be drawn and then the distances $\Delta\delta_{e,1}$ and $\Delta\delta_{e,2}$ to the appropriate centre of gravity lines should be taken for a given value of lift coefficient denoted in **Fig. 6.6** with the index “ref”. Since these functions have a constant slope, any obtained value of C_L can be selected. With K_N proportional to $\Delta\delta_e$, the following relationship is valid:

$$\frac{\Delta\delta_{e,1}}{\Delta\delta_{e,2}} = \frac{x_N - x_1}{x_N - x_2} \quad (6.29)$$

Solving for the neutral point's longitudinal coordinate, equation (6.29) can be written as

$$x_N = \frac{x_2 \Delta \delta_{e,1} - x_1 \Delta \delta_{e,2}}{\Delta \delta_{e,1} - \Delta \delta_{e,2}} \quad (6.30)$$

For a certain centre of gravity location, one can determine the respective value of the static margin, which according to equation (6.28) is the negative slope of the linear function of moment coefficient about the CG with lift coefficient. To obtain a function of moment coefficient with angle of attack, one can use the lift curve slope determined previously from a steady level flight test method, as shown in section 6.1.1.

$$\begin{aligned} \frac{dC_{M,c.g.}}{d\alpha} &= \frac{dC_{M,c.g.}}{dC_L} \frac{dC_L}{d\alpha} \\ &= -K_N \frac{dC_L}{d\alpha} \end{aligned} \quad (6.31)$$

If flight tests are performed for various centre of gravity locations, one can plot the moment coefficient versus angle of attack and obtain similar linear functions to the ones showed in **Fig. 6.4**, only the horizontal axis will consist of values for AOA. However, these will be valid only for the linear area of the lift curve slope and will not be representative at approaching stall speeds because of the assumptions made earlier.

An alternative graphical method would be to plot the elevator angle to trim against the total lift coefficient for two or more CG positions, as shown above in **Fig. 6.6**, and then determine the slope of each curve. The neutral point is given at a static margin value of zero where the function of trim angle with lift coefficient is a horizontal line, thus by plotting the determined slopes $d\delta_{e,trim}/dC_L$ against the CG position (expressed usually in percentage of MAC), one can obtain a linear function and then extrapolate it to its interception with the horizontal axis where $d\delta_{e,trim}/dC_L$ equals zero. This yields directly the neutral point position in percentage of MAC, as shown in the figure below. The calculation sequence continues as described above with equations (6.27) and (6.31) to obtain a function of moment coefficient with α . For both methods one can apply the MS Excel tool "Trendline" to determine all lines and their slopes from plotted separate points.

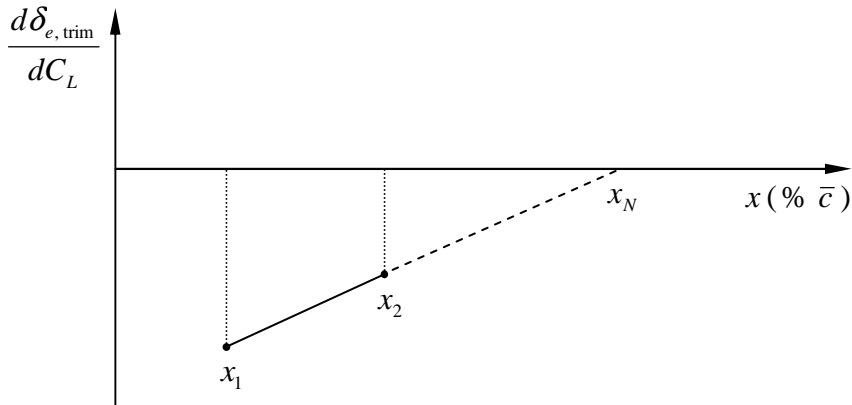


Fig. 6.7 Slope of elevator angle to trim with C_L plotted versus CG position

The above described technique offers a relative simple way to determine the stick-fixed neutral point position from flight tests with no additional equipment or special pilot flying qualities required. However, it assumes that all obtained trim curves are linear, which in practice is most likely not the case meaning that the location of the neutral point is not fixed and varies with changes in lift coefficient (**Young 2001**, Chapter 12, p. 21). Reasons for this include non-linearity of lift-curves of wing and tailplane especially near to the stall, non-linear characteristics of control surfaces, Reynolds number effects, interference between different parts of the aircraft etc. In such cases the stick-fixed neutral point position is to be determined for various lift coefficients and then plotted to obtain a curve representing its movement. An example of this technique can be found in **Kimberlin 2003** (p. 226), where the complete procedure is presented by means of flight test data from a Piper Archer aircraft. The results evaluation is similar to the one given in **Fig. 6.6**, however, the functions of elevator angle to trim with lift coefficient will not be linear. By drawing tangents at the tested values of C_L , one can determine the appropriate slopes $d\delta_{e, trim} / dC_L$ and then plot these as shown in **Fig. 6.7**, however, instead of one there should be several lines, each for a constant value of lift coefficient. Since for different CG positions the slopes at a constant lift coefficient will probably not have the same value, the tool “Trendline” can be utilised to extrapolate plotted points. The intersection of each line with the horizontal axis represents the stick-fixed neutral point position in percentage of MAC at the respective value of lift coefficient for the line. Finally, these can be plotted to determine a graph that shows the movement of x_N with C_L .

6.3 Lateral-directional static stability

So far in this chapter the longitudinal static stability of the aircraft was discussed, where changes in angle of attack were taken to generate only one moment, the pitching moment about the centre of gravity. On the other hand, the study of lateral-directional stability deals with the response of the aircraft in a sideslip – when its flight path deviates from the plane of

symmetry by the angle of sideslip β . Due to a present asymmetric flow field such motion would generate not only a yawing moment about the vertical axis, but also a side force in lateral direction and a rolling moment about the longitudinal axis, making lateral-directional stability analysis more complicated than the one discussed in the previous section. Furthermore, in this case rudder and aileron controls used to produce moments about either the vertical or the longitudinal axis also produce moments about the other axis introducing inevitable cross-coupling effects, which should be taken into account. Since the primary purpose of this section is to present a method for determining the function of side force coefficient with sideslip angle, only general concepts of lateral-directional stability analysis are included here with an emphasis on a flight test technique involving performance of steady heading sideslips to obtain directional stability derivatives describing the aircraft's control effectiveness, as well as the change of side force coefficient with β .

6.3.1 Governing equations

First, it is necessary to establish a reference body axes system of the aircraft and define a direction for positive and negative control surface deflections. So far only the aircraft's pitching moment was defined positive when tending to rotate the nose upwards, and coordinates along the longitudinal axis were mentioned, however, their direction was not specified. The most commonly used aircraft body axes system is also adopted in this work with moments in pitch M , roll \mathcal{L} , and yaw N taken positive about the appropriate positive axis direction applying the right-hand rule. This is shown in the figure below, which is similar to the one given by **Ward 2006a** (p. 131). Respectively, side forces are defined positive in positive y direction. The angle of sideslip is considered positive when the relative wind is displaced to the right of the aircraft's plane of symmetry.

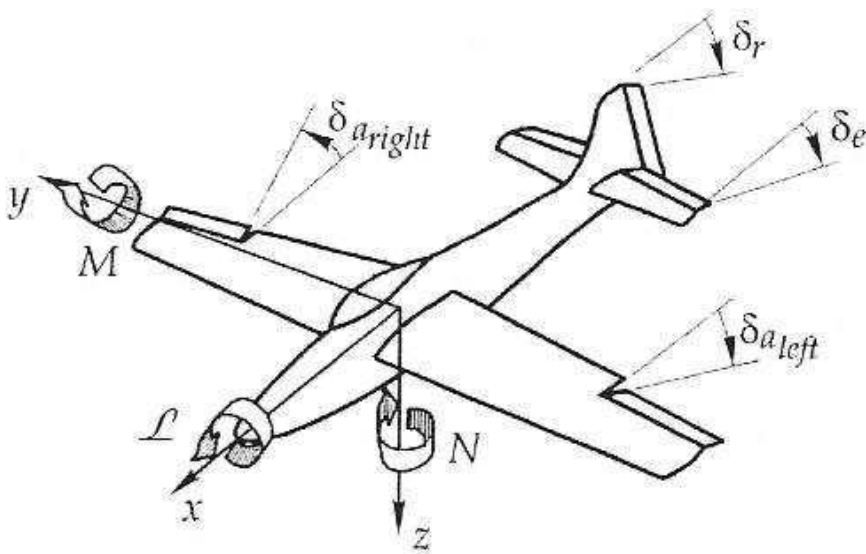


Fig. 6.8 Aircraft body axes system and standard sign convention

Further definitions for control surface deflections utilise the so-called “standard sign convention”, also shown in **Fig. 6.8**. For positive rudder and elevator angular deflections the observer is assumed to be sighting along the corresponding positive axis (z or y) and applying the right-hand rule, hence left rudder deflections and downward elevator deflections are positive. On the other hand, aileron deflections are considered positive when producing a positive rolling moment, hence an upward right aileron motion is required.

All necessary mathematical equations describing the aircraft’s static lateral-directional stability can be summarised using the dimensionless matrix form presented in equation (6.32) below, where forces and moments generated from roll or yaw rates are not considered due to the static nature of the problem discussed here. The parameters given in the derivative matrix denote changes in the appropriate side force or moment coefficient with the respective value from the angle vector. For apparent reasons these derivatives are not presented individually in the list of symbols in the beginning of this work and their meaning can be deduced from combinations of symbols and indexes adding the substantive “change” in front.

$$\begin{Bmatrix} C_Y \\ C_{L'} \\ C_N \end{Bmatrix} = \begin{bmatrix} C_{Y\beta} & C_{Y\delta_a} & C_{Y\delta_r} & C_L \\ C_{L'\beta} & C_{L'\delta_a} & C_{L'\delta_r} & 0 \\ C_{N\beta} & C_{N\delta_a} & C_{N\delta_r} & 0 \end{bmatrix} \begin{Bmatrix} \beta \\ \delta_a \\ \delta_r \\ \phi \end{Bmatrix} \quad (6.32)$$

NavAir 1997 (p. 5.34) also includes constants in each row of the derivative matrix describing side force, rolling and yawing moment at zero values for sideslip angle, aileron deflection, rudder deflection and bank angle, which could result from asymmetric configurations or loadings. However, such constants do not play any role in future calculations since, as seen later in this section, lateral-directional stability equations are differentiated with respect to sideslip angle. Although these are subject to cross-coupling effects, to conduct further analysis it is of some benefit to divide equation (6.32) into individual expressions and regard them separately. Such approach is presented in the following.

Equation (6.32) contains three further expressions, each describing a different force or moment acting on the aircraft – a side force in lateral direction, a rolling moment about the longitudinal axis and a yawing moment about the vertical axis. First, occurring side forces due to a motion in sideslip are discussed. These are generated by different parts of the aircraft, however, their main contributors are the vertical tail and an inclination of the lift vector due to existing bank angle (**Kimberlin 2003**, p. 304). In a steady sideslip a side force would cause a lateral translation, which for civil transport aircraft can be utilised to counter occurring drift due to heavy crosswinds during take-off and landing phase. In equation (6.32) the side force expression is given in the first row with the appropriate derivatives denoted with the index “Y” – the direction in which the side force occurs. Both **NavAir 1997** and **Ward 2006a** state that the change in side force due to aileron deflection is usually negligibly small and can be

dropped in further calculations. The influence of the aircraft's lift component in sideslip direction is denoted by the lift coefficient multiplied by the sine function of the bank angle, which for small values of ϕ can be replaced by the angle itself. In this work a flight test method consisting of series of steady heading sideslips is adopted, hence all forces are in equilibrium making the total side force coefficient equal to zero. Considering all this information and taking the derivative with respect to sideslip angle, the first row in equation (6.32) can be written as

$$C_{Y_\beta} + C_{Y_{\delta_r}} \frac{\partial \delta_r}{\partial \beta} + C_L \frac{\partial \phi}{\partial \beta} = 0 \quad (6.33)$$

This is the main equation that later in this chapter will be used to determine the change in side force coefficient due to sideslip C_{Y_β} .

The second row in equation (6.32) expresses static lateral stability, which is the study of the effects of sideslip on the aircraft's rolling moments. Since such analysis is beyond the scope of this work, only basic concepts are briefly discussed here without expressing these mathematically, as it is done for the side force and yawing moment coefficients. In order an aircraft to be stable, positive sideslip should provide a negative rolling moment, according to the sign convention, and vice versa, thus positive lateral stability is given when the aircraft tries to roll away from the sideslip. The main term producing lateral stability effects is the change of rolling moment due to sideslip, or "dihedral effect". It is mostly affected by the aircraft's geometric dihedral, the wing sweep angle and the vertical position of the wings on the fuselage. The vertical tail also has some influence on this derivative, whereas the magnitude of its contribution depends primarily on its size and moment arm to the centre of gravity in z direction. For a stable aircraft the change of rolling moment due to sideslip has a negative value, since it produces a negative moment about the longitudinal axis in case of a positive sideslip angle. Other derivatives in equation (6.32) include the change of rolling moment due to aileron deflection, or "lateral control power" and due to rudder deflection, however, these are not subject to further discussion here. For more information **Ward 2006a** (p. 174) or **NavAir 1997** (p. 5.32) should be consulted.

The last row of derivatives in equation (6.32) represents the static directional stability, or the effects of sideslip on the moments about the aircraft's vertical axis. When in a sideslip, a stable aircraft would produce a yawing moment that tends to restore zero sideslip, thus a rotation towards the relative wind (positive yawing moment at positive angle of sideslip). **Ward 2006a** (p. 171) refers to this as "weathercock stability" with the relevant derivative being the first one in the matrix given in equation (6.32) – the change of yawing moment due to sideslip. For a stable aircraft this derivative would have a positive value when the standard sign convention is used. The primary contributor to weathercock stability is the vertical tail,

which in case of a sideslip would experience a change in its local angle of attack and would produce a force that rotates the aircraft so as to reduce sideslip. The main parameter influencing this force is consequently the lift curve slope of the vertical tail, which can be modified by using a dorsal or a ventral fin. Other derivatives characterising directional control effectiveness are the change of yawing moment due to rudder deflection, or “rudder power”, and due to aileron deflection. According to the sign convention, a rudder deflection to the left is considered positive, which produces negative yawing moment, hence for a stable aircraft the rudder power is negative. On the other hand, in a subsonic flight aileron deflections, primarily used for lateral control, also produce an effect called “adverse yaw”, which exerts a yawing moment opposite to the desired direction of roll due to increased induced drag on the wing with the higher lift. Hence, this derivative will also be negative for a stable aircraft. In a steady heading sideslip where no accelerations take place, similarly to equation (6.33) for the side force, the directional stability expression can be written as

$$C_{N_\beta} + C_{N_{\delta_a}} \frac{\partial \delta_a}{\partial \beta} + C_{N_{\delta_r}} \frac{\partial \delta_r}{\partial \beta} = 0 \quad (6.34)$$

6.3.2 Steady heading sideslip test procedure and data reduction

So far in this section only theoretical background on static stability derivatives and the resulting governing equations for side force and yawing moment in a steady state was given. As already mentioned several times, the change of side force coefficient due to sideslip and other important derivatives describing the aircraft’s control effectiveness can be determined from flight tests by utilising a steady heading sideslip technique. It requires flying the aircraft at two CG positions and collecting data regarding angle of sideslip, bank angle, rudder and aileron deflections, actual weight and speed. The latter ones are used to calculate a lift coefficient for every sideslip performed. Yaw and roll rates, as well as lateral accelerations do not apply directly in post-flight test calculations, however, if this information is available it can be utilised to verify the accuracy of the recorded data. In the following paragraphs the precise technique description and the data handling afterwards are presented.

A steady heading sideslip manoeuvre begins with carefully trimming the aircraft at the nominal altitude and test airspeed. If tests are to be performed for a range of speeds with a power-off engine setting, one should start with the lowest speed at the highest altitude to minimise altitude loss. This is to be determined during the test planning phase to utilise flying time rationally. With the aircraft trimmed, a steady sideslip is entered by applying rudder at the desired direction. The aircraft is then stabilised at this sideslip angle and data is recorded. To establish a zero yaw rate, rudder and aileron should be applied simultaneously. Unlike in a level, unaccelerated turn, to maintain a steady heading sideslip a cross-controlled condition is required, meaning lateral and directional controls are applied in opposite directions. Once an

equilibrium condition is established and data is recorded, the sideslip angle is further increased by increasing the rudder deflection and again the aircraft is stabilised and data is collected. This procedure is to be repeated up to the maximum available rudder angle. **Kimberlin 2003** (p. 308) suggests using steps of approximately 0,25 full rudder deflection. Once tests are completed in one sideslip direction, the entire procedure is repeated for the opposite direction. Generally, the pilot should choose a fixed reference point at the distant horizon to help him maintain constant heading for each individual sideslip angle. However, since the *Raven* aircraft is piloted from the ground, constant heading is to be maintained strictly through visual contact. Normally, steady heading sideslips are not considered hazardous tests, however, if these are conducted at low speeds and large values of β there is the possibility of occurring stall at one wing resulting in an abrupt roll departure. Therefore at these conditions sideslip manoeuvres should be approached with caution. Unfortunately, no real-time data regarding sideslip angle is available for the *Raven* flight tests, thus visual contact from the ground will also be of primary assistance on this matter. In future tests, available real-time data regarding sideslip angle and heading by use of telemetry system could fairly improve the accuracy of the obtained results.

In the results evaluation phase all recorded data is first to be corrected for the appropriate instrument errors. In particular, static pressure measurements could be affected considerably by the occurring lateral flow inclinations, which would further reflect on less accurate calibrated airspeed and lift coefficient calculations. Corrected data is then plotted versus angle of sideslip to determine slopes like $\partial\delta_r/\partial\beta$ and $\partial\phi/\partial\beta$. A more detailed data reduction sequence and application of the governing equations can be found in the next paragraphs. Regarding plotting instrument corrected data, **Kimberlin 2003** (p. 309) gives exemplary plots of bank angle, aileron and rudder deflections versus angle of sideslip for a PA28-161 Warrior II propeller-driven aircraft. It is apparent that most plots are non-linear functions, which can be explained with occurring flow separations at various parts of the aircraft. Also, due to an alignment of the propeller slipstream with relative wind, the resulting plots from both sideslip directions are not symmetrical.

To obtain important derivatives describing the aircraft's control effectiveness, both **Ward 2006a** (p. 179) and **Kimberlin 2003** (p. 354) suggest the application of the above described steady heading sideslip technique for two different centre of gravity positions. This way the adverse yaw derivative from equation (6.34) can be eliminated and further relationships between change of yawing moment coefficient and change of side force coefficient can be estimated. However, this method requires certain assumptions to be made in order to simplify the governing equations, which reduces the accuracy of the obtained results for the aircraft's control effectiveness. These assumptions are summarised in the following:

- The distance along the aircraft's longitudinal axis between both CG values in question is small compared to the moment arm of the vertical tail to the z axis. **Fig. 6.9** gives an illustration of all geometric parameters used in further calculations and their definitions.

- Bank angles recorded during tests are small in a steady straight sideslip, therefore the rudder side force derivative can be ignored in equation (6.33).

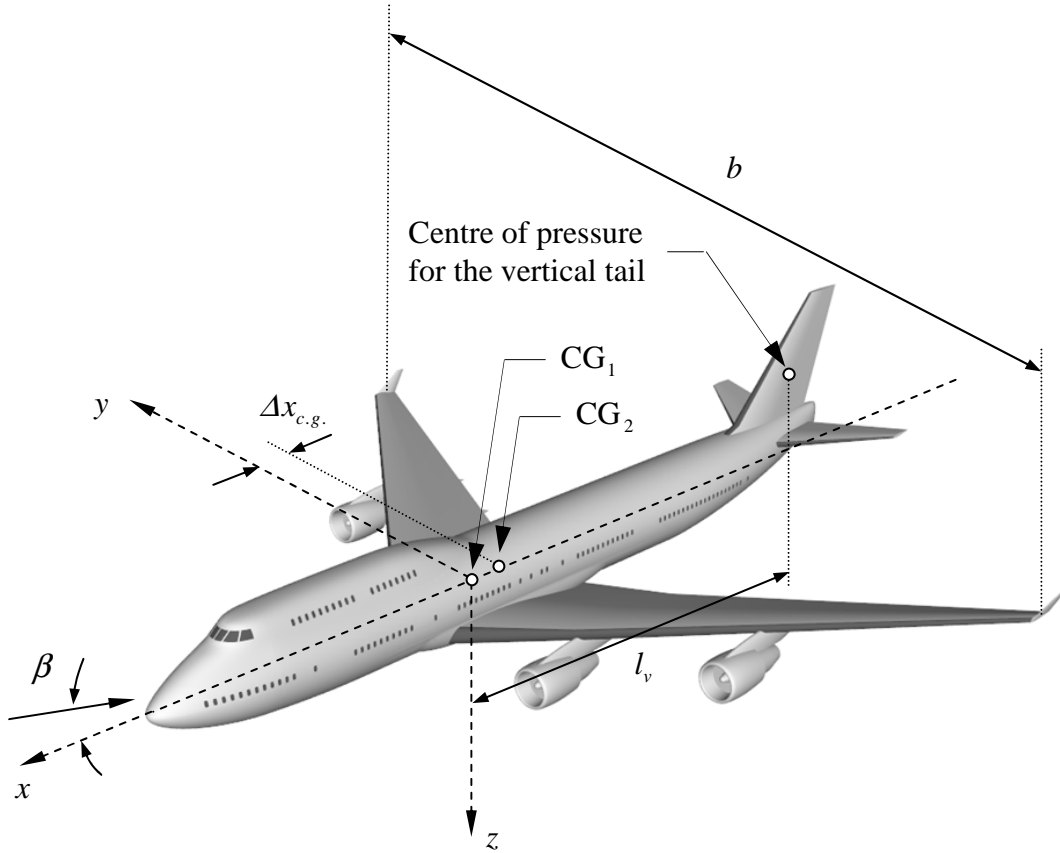


Fig. 6.9 Geometry of steady, straight sideslip at two different CG positions

Utilising these assumptions, one can come to the following conclusions. First, for small variations of CG along the x axis the rudder power derivative is essentially independent of the centre of gravity position, thus only variations of the weathercock stability derivative apply in this case. The change of this derivative due to a shift in CG backwards can be calculated using the equation below, where different centre of gravity positions are denoted with the indexes “1” and “2”.

$$C_{N_{\beta,2}} = C_{N_{\beta,1}} + C_{Y_{\beta}} \frac{\Delta x_{c.g.}}{b} \quad (6.35)$$

Secondly, with no change of side force coefficient due to rudder deflection considered, according to equation (6.33) the change of side force coefficient with β is a function of lift coefficient and the measured slope $\partial\phi/\partial\beta$ only. Hence,

$$C_{Y_{\beta}} = -C_L \frac{\partial\phi}{\partial\beta} \quad (6.36)$$

Since neither the slope $\partial\phi/\partial\beta$ nor the lift coefficient change with variations in CG position, the change of side force coefficient with angle of sideslip, whose determination is of primary importance in this section, can be obtained directly from equation (6.36). Lift coefficient is calculated using actual weight data and the corrected for instrument and position error calibrated airspeed, as shown for the steady level flight method in section 6.1.1. Since it is most likely that obtained slopes from plotting control surface deflections versus sideslip angle are not constant, **Ward 2006a** (p. 181) suggest taking these at zero sideslip angle.

To calculate further directional stability and side force derivatives, plots of rudder deflections versus sideslip angle are utilised. The data reduction sequence continues with writing down equation (6.34) for both CG positions, which yields the following expressions:

$$C_{N_{\beta,1}} + C_{N_{\delta_a}} \left(\frac{\partial\delta_a}{\partial\beta} \right)_1 + C_{N_{\delta_r}} \left(\frac{\partial\delta_r}{\partial\beta} \right)_1 = 0 \quad (6.37)$$

$$C_{N_{\beta,2}} + C_{N_{\delta_a}} \left(\frac{\partial\delta_a}{\partial\beta} \right)_2 + C_{N_{\delta_r}} \left(\frac{\partial\delta_r}{\partial\beta} \right)_2 = 0 \quad (6.38)$$

The slopes $\partial\delta_r/\partial\beta$ for both centre of gravity positions are also taken at zero sideslip angle for the same reason mentioned above. By substituting equation (6.37) from (6.38) "... and observing that the aileron slope change with sideslip is usually small" (**Ward 2006a**, p. 180),

$$\begin{aligned} C_{N_{\beta,2}} - C_{N_{\beta,1}} &= C_{Y_{\beta}} \frac{\Delta x_{c.g.}}{b} \\ &= C_{N_{\delta_r}} \left[\left(\frac{\partial\delta_r}{\partial\beta} \right)_2 - \left(\frac{\partial\delta_r}{\partial\beta} \right)_1 \right] \end{aligned} \quad (6.39)$$

Hence, for a known difference in tested CG positions along the longitudinal axis, the change of yawing moment due to rudder deflection can be calculated utilising the determined slopes $\partial\delta_r/\partial\beta$ for every centre of gravity, the wing span b and the previously obtained change of side force coefficient with sideslip angle. Furthermore, the change of side force coefficient due to rudder deflection can be estimated as

$$C_{Y_{\delta_r}} = -C_{N_{\delta_r}} \frac{b}{l_v} \quad , \quad (6.40)$$

The vertical tail moment arm l_v is taken to be the distance along the x axis between the vertical tail centre of pressure and the initial centre of gravity, as seen in **Fig. 6.9**. Since no information regarding the centre of pressure location of the vertical tail is available for the time being, this distance can be roughly estimated at first.

The above described method offers a straightforward test procedure and data reduction sequence to determine aircraft control effectiveness and the change of side force coefficient with sideslip angle. However, due to the simplifications made to the governing equations, it does have serious flaws when the accuracy of the obtained results is concerned. Other methods presented by **Ward 2006a** include the use of an external object (for example a parachute) with a known drag coefficient, mounted at a fixed position on one wing to produce an ascertainable asymmetric moment. By measuring the rudder deflection necessary to overcome this moment, one can determine the rudder yawing moment derivative. A similar to this method that includes placement of known weights at a certain spanwise location provides reliable data for lateral control effectiveness. These techniques yield more accurate results, however, they also require additional equipment and more complicated flight test performance, making them irrelevant in the *Raven* case for the time being. For data reduction sequence and test procedures the above given reference should be consulted.

7 Dynamic stability flight tests

So far in this work flight tests for determination of aerodynamic data and static stability were thoroughly discussed together with the appropriate data reduction sequences. This last chapter deals with dynamic stability in general and with flight test methods to determine parameters like frequency and damping ratio for existing stability modes of classical aircraft configurations. Dynamic stability describes the behaviour of the aircraft with time following a disturbance from equilibrium. It "... characterises the vehicle's ability to change from one equilibrium condition to another" (**Ward 2006a**, p. 185). As it was described earlier, dynamic stability takes into account forces and moments that arise due to velocities and accelerations, therefore measurements are not to be made in a state of equilibrium. Consequently, the required flight testing methods are more complicated than the ones given so far. Due to this complexity and the fact that investigations of the *Raven* dynamic stability are not a priority of the first flight tests planned, the approach in this chapter will not go into great detail for all characteristic aircraft motions remaining more general in the information provided for some tests. The text will concentrate mostly on the practical part of the flight tests describing thoroughly the individual test procedures and data reduction sequences where available, while the theoretical part will be left aside. Further details can be found in the references given in the course of the text.

In a dynamic sense, a moving body is regarded as stable when it tends to remain in equilibrium position over a period of time, hence positive dynamic stability is present when the amplitude of the resulting motion is decreasing with time. An aircraft can be statically stable and dynamically unstable at the same time, when the amplitude function passes through equilibrium, but increases with time. However, it cannot be dynamically stable and statically unstable. One can further classify stability modes into non-oscillatory and oscillatory. In the first case the amplitude would decrease or increase depending on whether the aircraft possesses positive or negative dynamic stability, however, the motion would not pass through equilibrium condition. In oscillatory modes a tendency to return to trim should be present, hence positive static stability is required. These are basic concepts which will be referred to indirectly in this chapter. To conduct further analysis, dynamic motions will be divided into two sets – a longitudinal and a lateral-directional motion – and will be discussed separately, as was done in the static stability analysis earlier.

Before proceeding to the longitudinal and lateral-directional stability, first it is necessary to present the types of control inputs used in flight tests to determine the aircraft's dynamic characteristics. Normally, dynamic motions are excited using rapid pilot inputs to the control surfaces. **Ward 2006a** (p. 208) classifies three typical control inputs – step inputs, singlet inputs and doublet inputs. In the ideal case the surface rate should be infinite, thus the desired deflection angle should be reached in zero time. However, no control system can provide such infinite surface rate. The appropriate ideal control surface deflections for all three typical

inputs are given in **Fig. 7.1**. One can see that the change of control surface angle with time is infinite (vertical line). The function of the actual control surface deflection with time performed by the pilot will have a slight inclination from the vertical line.

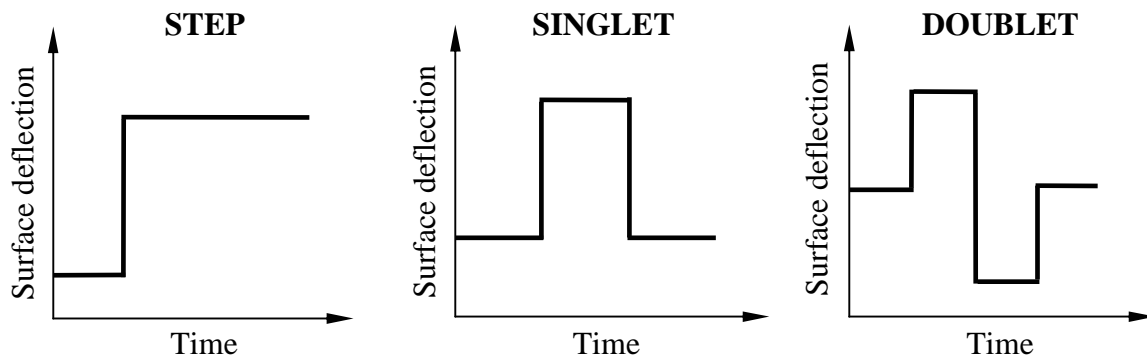


Fig. 7.1 Types of control inputs for dynamic stability flight tests

The first ideal input shown in **Fig. 7.1** is the *step* input consisting of moving the control surface to the desired deflection angle and holding it fix in this position. Hence, the control surface is set to a new trim position causing the aircraft to take a new equilibrium state. For example, an elevator step input will cause the aircraft altitude, angle of attack and airspeed to take new trim values some time after the input. The second type of control input is the *singlet* input or pulse, for which the control surface does not remain in the new position, unlike in the step input case. Short time after the deflection occurs, the pilot returns the control column to the initial position, hence this input consists of a positive and a negative step input of the same magnitude. The last input is called the *doublet* and consists of two singlet inputs in opposite directions occurring consecutively one after the other. Hence, after the control surface is returned back to trim position, it is immediately deflected to the same angle in the opposite direction and then returned back to trim.

From these control surface inputs the latter two are most commonly utilised in dynamic stability flight tests. Normally, for the pilot to be able to return accurately the controls in the initial position, the displacement of the control column is measured. Since most likely such measurement cannot be applied for the *Raven* controls, inputs should be repeated until the one that best excites the targeted mode is found using visual contact from the ground.

7.1 Longitudinal dynamic stability

As stated in the introduction of this chapter, the approach here is to present the practical side of the flight tests avoiding theory on dynamic stability as much as possible, including equations of motion and stability derivatives. However, it is of some benefit to describe

briefly the results from such theoretical analysis and what they mean for the individual modes of motion. Both **Kimberlin 2003** (p. 236) and **Ward 2006a** (p. 186) compare the dynamic behaviour of aircraft longitudinal motion with a spring-mass-damper system, since mathematically the solutions for both equations of motion are identical. As these are second-order differential equations, a transform is applied to reduce them to algebraic equations containing the complex LAPLACE operator. The longitudinal equations can then be written in determinant form, which is afterwards solved to obtain a quartic characteristic equation. This can be further factored into two quadratic terms, each of them describing two characteristic modes of motion for a conventional aircraft configuration – the *short period* and the *phugoid* mode. Since they are expressed by quadratic terms, both are oscillatory motions, however, of widely differing frequency. The phugoid mode is a lightly damped motion of low frequency with a long period of more than 30 seconds. On the other hand, the short period, as its name suggests, is a high frequency motion with a period that normally ranges between 0,5 and 5 seconds. If plotted in a complex plane, the roots of both quadratic terms would have imaginary components, which is an indication of oscillatory motion. Roots for phugoid will be much nearer to the imaginary axis and depending whether they are on the positive (right) or negative (left) side, the motion will be respectively unstable or stable. On the other hand, roots for short period will usually be far to the left of the imaginary axis, thus indicating a stable motion. For reasons stated earlier, a graphical illustration of this analysis is not presented in this work and can be found in the references given so far in this section. Since the purpose here is to investigate flight test methods to determine frequency and damping ratio for both short period and phugoid, these are presented individually in the following.

7.1.1 Short period mode

The aeroplane short period mode takes place at nearly constant airspeed with occurring changes in angle of attack and pitch rate. For most conventional aircraft it is well-damped with times to half amplitude about 0,5 seconds. However, if this is not the case, the short period oscillation becomes of great importance because the pilot must control it immediately. Normally, depending on the control system one can discriminate between stick fixed and stick free short period. In the latter case the aeroplane short period may be coupled with an elevator rotation about the hinge line, called elevator short period. However, this is not discussed here since the *Raven* aircraft is equipped with an irreversible control system consisting of electrical actuators, which hold the elevators in a fixed position. In a short period mode “... the restoring tendency for the pitch oscillation is provided by static stability while the amplitude of the oscillation is decreased by pitch damping” (**Kimberlin 2003**, p. 242). Hence, the dominant stability derivative which contributes primarily to the increase of damping is the change of moment coefficient due to pitch rate. On the other hand, the short period natural frequency would increase with increasing derivative that gives the change of moment coefficient with angle of attack.

Theoretically, short period damping ratio and natural frequency can be calculated by applying certain assumptions about the stability derivatives in the equations of motion. **Ward 2006a** (p. 199) gives approximations for such calculations using dimensional derivatives. As seen from the example given there, the obtained results for natural frequency are very close to the ones obtained from the full characteristic equation, giving a difference of approx. 3 %. For the damping ratio the difference lies a bit higher – at approx. 17 %. On the other hand, **Kimberlin 2003** (p. 245) presents also approximations for natural frequency and damping ratio calculation, however, these include predominantly geometric values of the aircraft, like wing area, MAC and inertia moment about the lateral axis, and flight parameters, like Ma and p . The derivatives there are restricted to lift curve slope and change of moment coefficient with angle of attack and pitch rate. Since no reliable information regarding stability derivatives of the *Raven* is available at this point, the formulas given in the latter reference are more suitable for pre-flight testing calculations to predict short period damping ratio and natural frequency.

Practical experience shows that since for most conventional aircraft the short period mode is heavily damped, it could be difficult to record reliable data, based on which calculations to determine the natural frequency and damping ratio can be made. **Kimberlin 2003** (p. 250) gives three techniques used to excite short period mode with the control surface inputs described in the beginning of this chapter. The first and most suitable method consists of applying the doublet input, which in addition to exciting the short period mode, also tends to suppress the phugoid mode making data reduction easier in the post-flight test evaluation process. The precise technique consists of trimming the aircraft at nominal test altitude and airspeed and then rapidly moving the aircraft nose up, down and back to trim by applying elevator inputs. Data is recorded until the short period motion has subsided. The pilot should try varying the frequency of the doublet input until he finds the one that best excites the short period frequency of the aircraft.

Another possible control surface input to excite short period is the singlet. This should however be avoided, since it also tends to excite the phugoid mode making the separation of short period and phugoid motions in the post-flight data analysis very difficult. On the other hand, this technique is necessary to apply for aeroplanes with a high short period frequency. The last method available for short period flight testing is the so-called “2-g pull-up”, which is a form of the step input. After trimming the aircraft, the pilot performs a pull-up decreasing airspeed and increasing altitude. Then the aircraft’s nose is pushed over entering a steep dive. At approaching trim conditions the pilot smoothly rotates the aircraft using elevator control inputs so that trim speed and altitude are achieved at the same time. This method is also very good for determination of short period characteristics since it suppresses the phugoid mode. Its main application should be for aircraft with low short period frequency. However, it also requires excellent pilot skill to perform the above described manoeuvre. In the *Raven* case the real-time indications of trim altitude and airspeed from the separate telemetry system can be utilised for pilot assistance.

Ward 2006a describes several methods for reduction of recorded test data. A rough estimate for short period damping ratio can be obtained using equation (7.1). It is a valid approximation for values of λ between 0,1 and 0,7. By counting the number of peaks in pitch attitude until an oscillation can no longer be discerned, one can determine the damping ratio. This is however easier to observe for a pilot sitting in the cockpit of a full-sized vehicle than for one piloting a model aircraft from the ground.

$$\lambda_{sp} \approx \frac{7 - \text{number of peaks counted}}{10} \quad (7.1)$$

More precise results can be achieved using graphical methods where the response curve representing the aircraft behaviour with time is analysed. Some of these methods are the Transient Peak Ratio (TPR), the Maximum Slope and the Time-Ratio method. The latter two are discussed here with a data reduction sequence given only for the Maximum Slope method. The TPR method is briefly presented in the next section where flight test procedures to determine phugoid characteristics are discussed.

The Maximum Slope method, as well as the Time-Ratio method, are normally used for short period damping ratios between 0,5 and 1,0. The basic assumption made for these methods is that any oscillations associated with aircraft dynamics can be taken to be either a first- or a second-order response. A qualitative example of recorded short period data is presented on the left side in **Fig. 7.2**. Both elevator deflection and aircraft pitch rate are plotted versus time with a magnified image of the dotted square area around the pitch rate response curve given on the right. The Maximum Slope data reduction method consists of drawing first horizontal lines at the half-cycle peaks (maximum and minimum) and then a maximum slope tangent line for the progression of the curve between them (shown below as a dashed line).

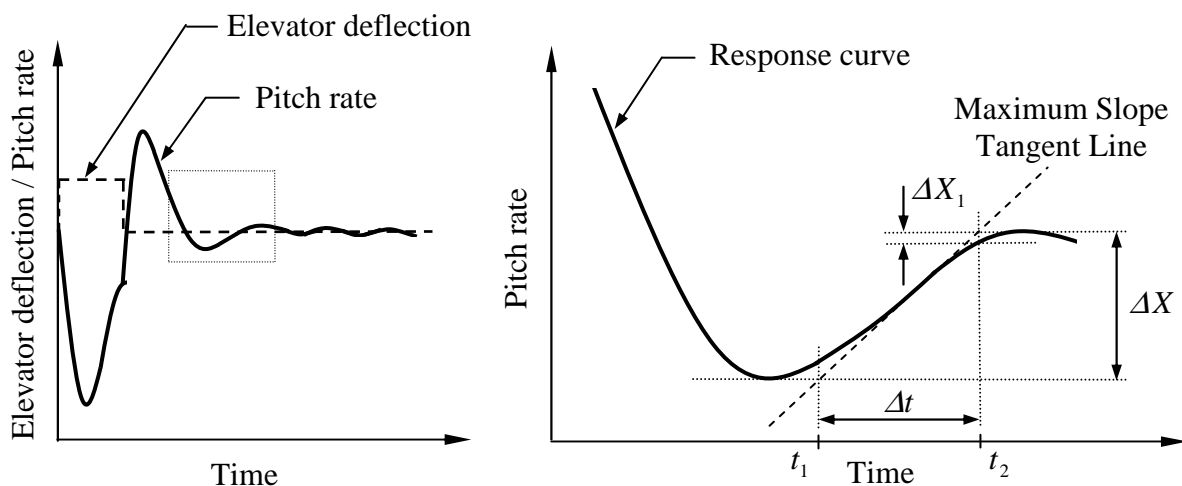


Fig. 7.2 Qualitative example of Maximum Slope method for data reduction

The intersections of the maximum slope tangent line with the horizontal lines at both half cycle peaks define Δt . With ΔX given between these half cycles peaks and ΔX_1 defined from the intersections of the t_2 vertical line with the response curve and the maximum slope tangent line, one can calculate the ratio $\Delta X_1 / \Delta X$ and use it to enter the chart presented in **Fig. 7.3**. Although “X” has units of °/sec, it is regarded only as an auxiliary symbol and is therefore not referenced in the list of symbols. The chart below is taken from **Ward 2006a** (p. 220) where the damping ratio is denoted with the symbol “ ζ ” not utilised in this work. With the term $\omega_n \Delta t$ determined, one can calculate the natural frequency with

$$\omega_{n,sp} = \frac{\omega_n \Delta t}{\Delta t} \quad (7.2)$$

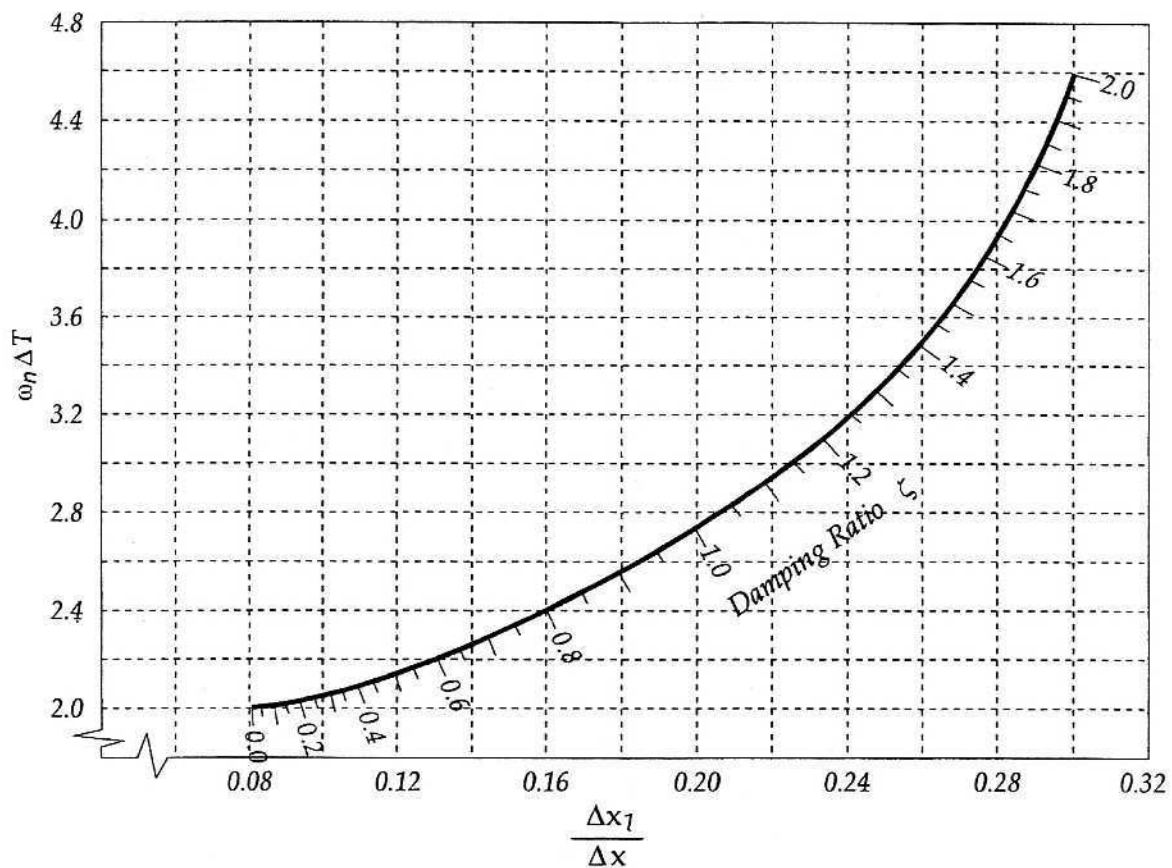


Fig. 7.3 Chart for determining damping ratio and natural frequency (**Ward 2006a**)

The problems associated with this data reduction method concern primarily the parameter ΔX_1 , which is usually small and difficult to measure accurately. However, the resulting error affects mostly the short period damping ratio λ , whereas the natural frequency remains largely unaffected. An alternative technique for short period data reduction described by **Ward 2006a** (p. 218) is the Time-Ratio method, which requires a steady-state equilibrium to

be reached after the short period mode excitation has subsided. Basically, the data reduction sequence consists of taking values of Δt and ΔX at three places of the response curve and similarly to the Maximum Slope method use them to enter a specific chart where λ and ω_n can be read. This yields three different values for the damping ratio, which are normally averaged, depending on the quality of the response curve, to obtain a final value. More detailed description of the precise data handling and an example calculation for an F-89 Scorpion short period characteristics can be found in the above given reference.

Analogue to a mass-spring-damper system, the short period damped frequency ω_d can be calculated using the values for λ and ω_n , as shown in equation (7.3). This equation can also be utilised for calculations regarding the damped frequency of the phugoid mode.

$$\omega_d = \omega_n \sqrt{1 - \lambda^2} \quad (7.3)$$

7.1.2 Phugoid mode

The phugoid mode describes a low frequency motion during which potential and kinetic energy are exchanged. Essentially, it is an airspeed and altitude oscillation typically taking place with a negligible variation of angle of attack. With increasing altitude the aircraft's speed decreases, thus lift decreases. After reaching a certain maximum altitude value, due to the decrease in lift the aircraft goes into a dive where altitude is decreased and airspeed increased. This causes lift to increase and at some point the aircraft reaches a minimum value of altitude and a maximum value of airspeed. Due to the increased lift the aircraft starts climbing again and the process is repeated. A qualitative illustration of a phugoid response curve is given in **Fig. 7.4**. The damping effect in this motion is provided by aeroplane drag, which increases with increasing airspeed and vice versa, and tends to return the aircraft to the neutral condition of trim speed. Consequently, in an equilibrium flight the damping ratio is directly proportional to the aircraft total drag coefficient. If the aircraft altitude is maintained constant, λ would increase with increasing true airspeed. On the other hand, if the aircraft's true airspeed is held constant, the phugoid damping ratio would decrease directly proportional to the change in density with altitude.

Like in the short period mode case, approximations to determine pre-flight test values of damping ratio and natural frequency for the phugoid mode can also be found in the references given so far in this section. These approximations are the same as the ones given also by **Meins 2001** (p. 101) and are presented here in equations (7.4) and (7.5). The phugoid natural frequency is taken to be inversely proportional to the trim airspeed and the damping ratio is given as inversely proportional to the lift-to-drag ratio. Using pre-determined values for trim airspeed and lift and drag coefficients, one can calculate rough estimates of the phugoid

characteristics. However, unlike the results calculated with the short period mode approximations, the ones obtained for the phugoid mode are due to the assumptions and simplifications made rather crude and cannot be utilised to provide accurate conclusions.

$$\omega_{n,p} = \sqrt{2} \frac{g}{V_{\text{trim}}} \quad (7.4)$$

$$\lambda_p = \frac{1}{\sqrt{2}E} \quad (7.5)$$

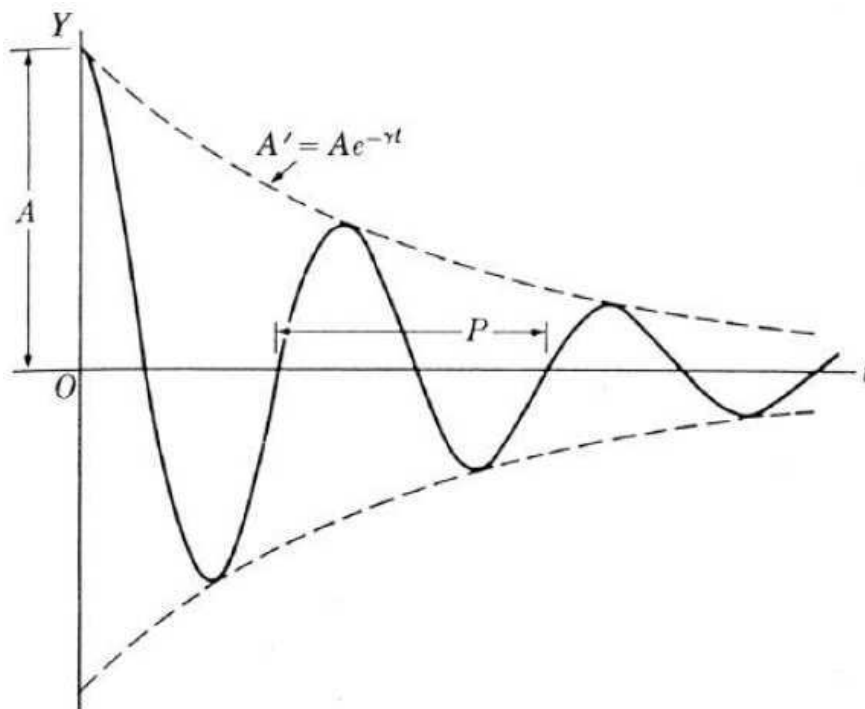


Fig. 7.4 Qualitative illustration of a damped phugoid oscillation (Meins 2001)

For flight test measurements the phugoid motion is excited with a singlet of fairly long duration. First the aircraft is stabilised at test trim speed and altitude for a given aircraft configuration of power, gear and flaps. Careful trimming is essential for an accurate phugoid flight test performance. Therefore, in the trimmed position speed and altitude have to remain within respectively 0,5 kts and 20 ft for approx. 15-20 seconds with no inputs from the pilot (Ward 2006a, p. 209). Once this is achieved, the pilot applies an elevator input holding the step long enough to reduce the aircraft's speed by 10-15 kts from the trim airspeed. Then the elevator is returned carefully to trim position using control movement matching the aircraft long period frequency. Afterwards the occurring oscillation is recorded with the pilot making no further longitudinal inputs. In order the wings to be maintained level, small lateral control inputs are allowed, as even small bank angles may affect both the phugoid damping ratio and its natural frequency.

Response curves for altitude, airspeed and pitch attitude all can be utilised in the evaluation process to determine the aircraft's phugoid characteristics. One possible method for reduction of data recorded during flight tests is the TPR method, which is the most useable one for damping ratios between -0,5 and 0,5. By plotting true airspeed versus time, one can obtain a response curve with similar progression to the one given in **Fig. 7.4**. If the half cycle peaks are numbered with 1,2,3,4 etc., one then takes the amplitudes X_1, X_2, X_3, X_4 etc. (vertical distances from the t -axis to the appropriate peaks) and calculates the ratio of every two adjacent amplitudes. Ideally, these ratios should be identical, however, since for actual test measurements they are not, one can take an average value. This parameter is called Transient Peak Ratio and is used to enter a specific chart from which the phugoid damping ratio can be determined. Such chart is however not presented here, it can be found in both **Kimberlin 2003** (p. 250) and **Ward 2006a** (p. 218). With the obtained damping ratio one can calculate $\omega_{n,p}$ from equation (7.6), where the phugoid damped period is denoted with T_p .

$$\omega_{n,p} = \frac{2\pi}{T_p \sqrt{1 - \lambda_p^2}} \quad , \quad (7.6)$$

Besides the above described graphical method, one can also apply a numerical method to determine phugoid characteristics. This is presented here using example flight test data recorded during laboratory exercises at the Hamburg University of Applied Sciences on October 15, 2003. The MS Excel data file containing this information and the calculation sequence is referenced here as **Scholz 2005**. First, values of measured airspeed are taken for every half cycle peak during the occurring phugoid mode and the corresponding time is noted. These are presented in the first two rows of **Table 7.1**. A mathematical expression of the change of airspeed with time containing phugoid damping ratio and natural frequency is then used to start the numerical process. This is presented in the following equation

$$V(t) = V_{\text{trim}} + \frac{V_{\text{max}}}{2} e^{-\lambda_p t} \cos(\omega_{n,p} t) + \Delta V t \quad , \quad (7.7)$$

where the phugoid characteristics λ and ω_n and the parameters $V_{\text{trim}}, V_{\text{max}}$ and ΔV are not known at first. The essence of this method is that one uses iteration to calculate these parameters, so that they yield a response curve for the true airspeed as close as possible to the measured one. A suitable tool for performing this iteration process is the MS Excel "Solver", for which initial values of the above presented parameters should be provided. For this purpose, equations (7.4) and (7.5) can be utilised to calculate rough estimates of phugoid damping ratio and natural frequency with the aircraft trim speed known. For V_{max} and ΔV however, empirical values have to be used. The mathematical manipulation consists of taking the square of the difference between measured airspeed and calculated airspeed from equation

(7.7) for every measured time point. The iteration process is then started using “Solver” under the condition that the parameters in equation (7.7) need to be adjusted until the sum of all squared differences reaches a minimum value. The results for the calculated values of true airspeed with time and the squared differences are given in the last two rows of **Table 7.1**.

Table 7.1 Example data for measured and calculated airspeed

Time t [s]	True airspeed V [kts]		Δ^2
	measured	calculated	
0	150	147,668	5,437
14,4	85	84,881	0,014
28,9	135	139,141	17,149
43,0	95	93,221	3,167
57,7	133	131,143	3,448
71,5	100	101,096	1,201
88,0	127	127,113	0,013
102,4	100	102,320	5,383
119,8	125	124,868	0,018
132,0	105	105,321	0,103
147,5	120	120,255	0,065
159,9	112	109,972	4,115

The resulting phugoid characteristics and parameters of equation (7.7) calculated in the iteration process are given in the following table. Also, phugoid damping ratio and natural frequency calculated from equations (7.4) and (7.5) with the trim speed determined from the iteration are given to make a comparison. The lift-to-drag ratio used to compute λ is the maximum one determined from steady glide flight tests. One can see that unlike the natural frequency values, which are comparable, the relative error for λ is more than 600 %.

Table 7.2 Solver results for phugoid characteristics and parameters

Parameter	Calculated value		Unit
	Iteration	Eq. (7.4) and (7.5)	
V_{trim}	114,2326768	-	kts
V_{max}	66,87112585	-	kts
λ_p	0,008668716	0,06225	-
$\omega_{n,p}$	0,208474721	0,23608	rad/s
ΔV	-0,008800093	-	kts/s

Both measured true airspeeds and results from equation (7.7) are plotted versus time in **Fig. 7.5**. Although in most cases the measured points do not lie directly on the half cycle peaks, one can see that this numerical method yields a satisfactory approximation of the true airspeed response curve for the phugoid motion.

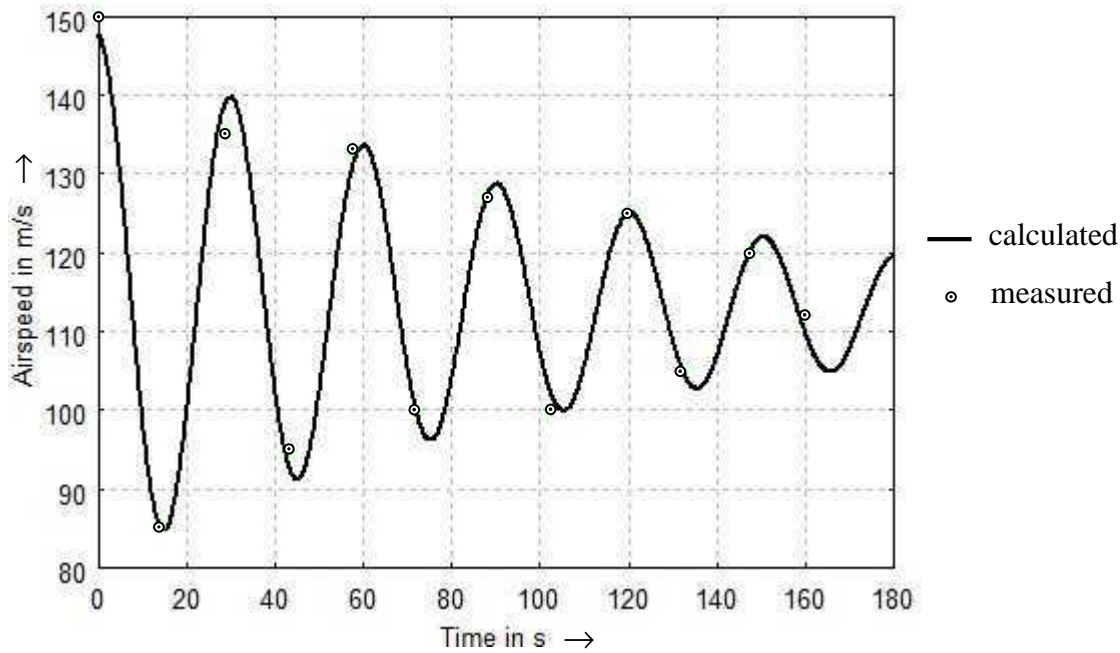


Fig. 7.5 Plot of measured and calculated airspeed versus time in a phugoid mode

7.2 Lateral-directional dynamic stability

So far in static lateral-directional analysis the aircraft's lateral and directional responses were considered separately with an emphasis on the directional stability and methods to determine the change of side force coefficient with angle of sideslip. In dynamic lateral-directional stability the responses are coupled with the aircraft's inertia affecting this coupling, therefore they will not be separated here. Similar to the longitudinal modes of motion, using a transformation for small disturbances one can determine a characteristic equation for the lateral-directional modes of motion. For a conventional aircraft configuration these are the *spiral* mode, the *roll* mode and the *Dutch roll* mode. From all three modes regulations only for the Dutch roll mode are issued by the civil aviation authorities, whereas the other two are not considered. If plotted in a complex plane, both spiral and roll roots lie on the real axis and have no imaginary components indicating a non-oscillatory motion for both modes. Normally the roll mode has a large negative real root, hence the motion is heavily damped for most conventional aircraft. On the other hand, the spiral root is very near to the imaginary axis and can be either positive or negative indicating respectively a divergence or a convergence. A root at the origin would suggest neutral spiral mode stability indicating neither a convergence nor divergence when the motion is excited. Unlike the other two lateral-directional modes, the Dutch roll mode is represented in the complex plane by a pair of roots with both real and imaginary components, which indicates a second-order oscillatory type of motion. A plot of the roots of all three lateral-directional stability modes in a complex plane can be found in **Kimberlin 2003** (p. 3.14).

7.2.1 Spiral mode

The spiral mode is a first-order lateral-directional mode of motion, which in case of divergence can be described as an increase in bank angle after a bank angle disturbance from wings level flight. With occurring bank angle, a sideslip in direction of the lowered wing is introduced which creates a force at the vertical tail tending to yaw the aircraft in direction of the sideslip. Due to the occurring yawing moment lift generated by the wing going forward, which is also the higher wing, is increased, thus creating a rolling moment in direction of the sideslip. With steadily increasing yaw and bank angles the curvature of the turn becomes tighter and the aircraft goes into a spiral dive gaining speed and losing altitude. An illustration giving the motion of the aircraft in a spiral mode, as viewed from both axes concerned, is presented in **Fig. 7.6**.

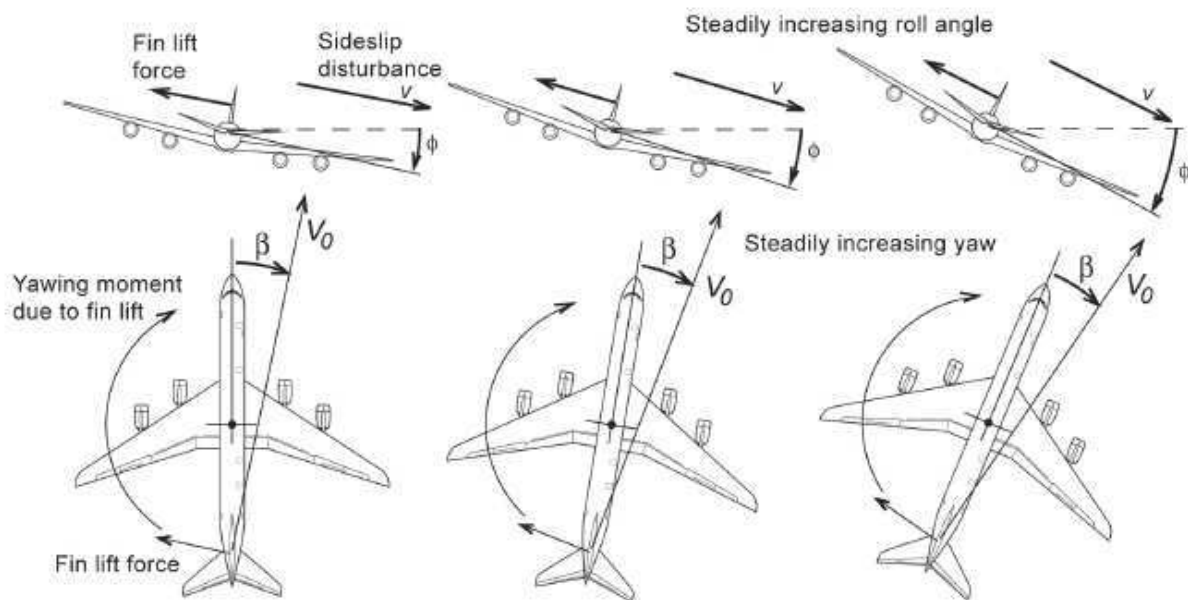


Fig. 7.6 Aircraft behaviour in a spiral mode (MIT 2008)

Normally, some spiral mode instability is allowed, since even when divergent, this motion can be easily controlled by the pilot for conventional aircraft configurations. However, the time to double the bank angle should be long enough, so that the pilot can apply a correction without having to devote an excessive amount of his attention. Strong directional stability tends to make the spiral mode diverge, with the rate at which the divergence occurs being greater at lower speeds and smaller at high speeds (Kimberlin 2003, p. 314). On the other hand, improving the aircraft's lateral stability makes it converge, hence an increased dihedral effect tends to stabilise the spiral mode. Increasing the sweep angle of the wings also improves spiral mode convergence, however, both measures have the undesirable effect of reducing Dutch roll damping ratio. Since Dutch roll stability is of greater importance for the aircraft's handling qualities, a slightly unstable spiral mode is preferred.

To test the aircraft's spiral mode behaviour, first the air vehicle is brought to the desired trim condition for airspeed, altitude, power setting, flaps and gear. After trim is achieved, the aircraft is rolled to a bank angle of approx. 10° (according to **NavAir 1997**, p. 123 – at least 5° , but not more than 20°) using a small rudder input while the lateral controls are held fixed. After establishment of the steady bank angle, the rudder is returned to trim position and all controls are released. The change of bank angle with time is recorded – if ϕ increases, the spiral mode is unstable; if the aircraft rolls out of the turn, then the spiral mode is stable. After data is recorded, the aircraft is recovered and the above described procedure is repeated with opposite bank angle. Usually aileron inputs are not utilised to bank the aircraft, because of the significant rolling moments generated. An alternative control input that can be used instead of rudder deflection is a slight power reduction of one engine for a multi-engined aircraft.

Depending whether the spiral mode is divergent or convergent, in the evaluation process the time to double or respectively the time to half the bank angle is to be determined. In this work a data reduction sequence is presented by means of recorded data given in **Scholz 2005**. The observed spiral mode motion is unstable, hence the time-to-double is determined using the recorded variation of bank angle with time, presented below in **Table 7.3**.

Table 7.3 Example bank angle variation with time in a spiral mode

Time t [s]	Bank angle ϕ [$^\circ$]
0	10
13	20
26	30
36	45

Mathematically the variation of bank angle with time can be approximated with an exponential function of the natural logarithm containing a damping ratio λ . For an initial value of bank angle equal to 10° this approximation can be written as

$$\phi(t) = 10e^{-\lambda t} \quad , \quad (7.8)$$

where for the measured data λ equals -0,0428 indicating a divergent spiral mode. Both measured and calculated data from equation (7.8) are presented graphically in **Fig. 7.7**. Knowing that at time-to-double the bank angle is twice as much as the initial value, one can apply a mathematical manipulation from which the resulting t_{double} can be calculated as

$$t_{double} = \frac{\ln(2)}{-\lambda} \quad (7.9)$$

For the previously calculated value of λ the time-to-double is approximately 16 seconds, differing from the measured time of 13 seconds to reach a bank angle of 20° . One can see that up to 25 seconds both curves in **Fig. 7.7** have significantly different progression, hence the resulting 3 seconds discrepancy in t_{double} .

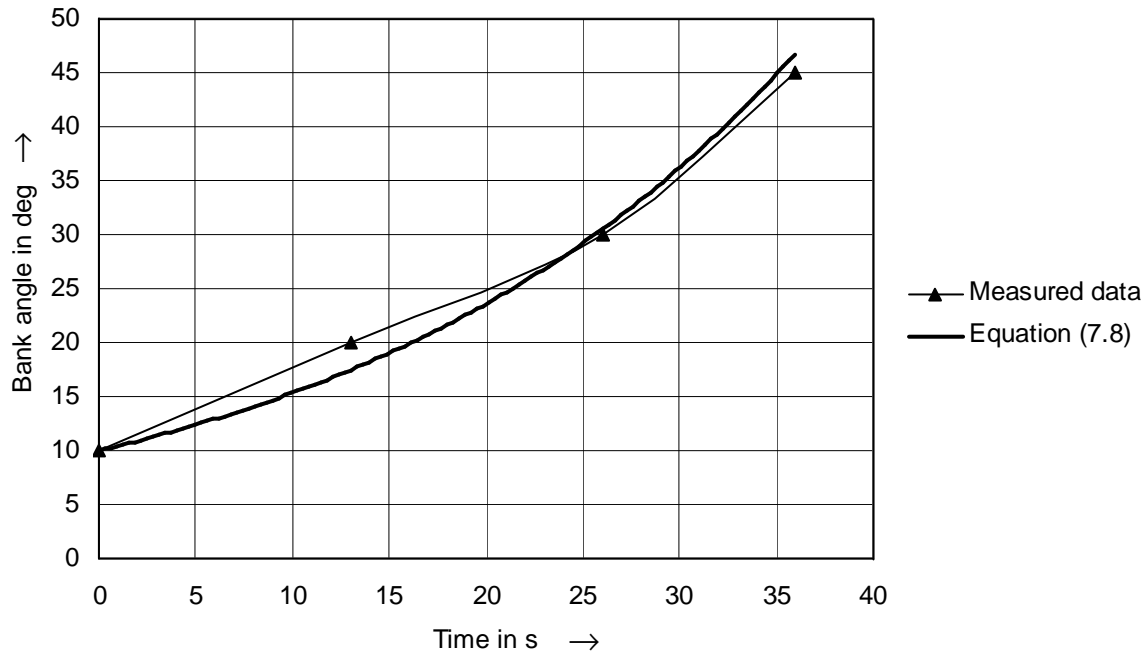


Fig. 7.7 Example of spiral mode measured data and mathematical approximation

An alternative method to determine graphically the spiral mode time-to-double is presented in section 7.2.4 where data reduction sequence for a lateral-directional response to a step aileron input is given.

7.2.2 Dutch roll mode

The Dutch roll oscillation consists of tightly coupled yawing and rolling motions and usually occurs at medium to high frequency. With no directional stability augmentation system installed it has normally moderate to light damping ratio. Strong lateral stability and increase in the wing sweep angle reduce the aircraft's natural Dutch roll damping. An illustration of a Dutch roll motion, as seen from both the vertical and the longitudinal axis, with four specific positions during the oscillation is presented in **Fig. 7.8**. Such yaw-roll oscillation can be quite uncomfortable for both crew and passengers, therefore civil transport aircraft with swept wings often need a yaw damper to increase the aircraft's natural damping and improve both its ride and handling qualities. A large vertical tail would also augment the Dutch roll natural damping ratio. For Part 23 aeroplanes the FAA requires that "... any Dutch roll oscillation

that occurs between stalling speed and maximum allowable speed must be damped to 1/10 amplitude in 7 cycles with the primary controls fixed and free” (Kimberlin 2003, p. 311).

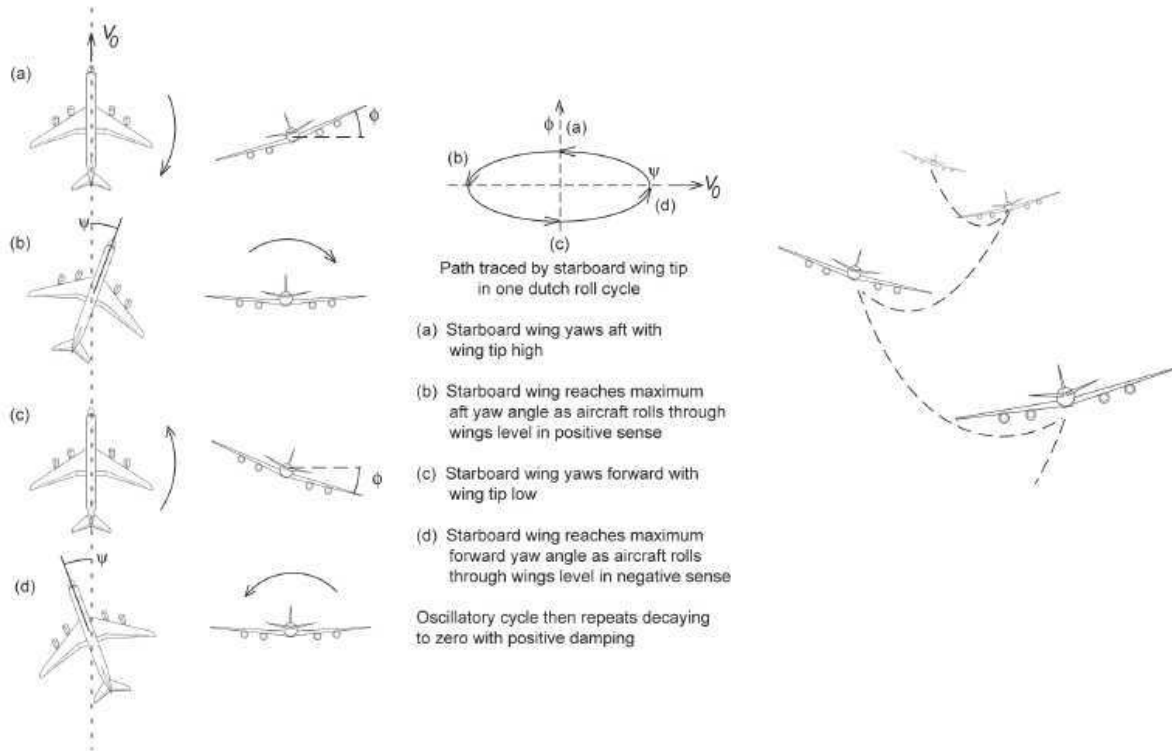


Fig. 7.8 Dutch roll oscillation (MIT 2008)

For calculation of rough estimates of Dutch roll natural frequency and damping ratio, Kimberlin 2003 (p. 315) gives mathematical approximations presented in the following. For the natural frequency the rolling moments due to sideslip and due to roll rate are assumed to be zero, which yields a relationship given below in equation (7.10). One can see that the frequency varies directly with Mach number and increases with increasing directional stability. On the other hand, increasing altitude and moment of inertia in yaw reduce Dutch roll natural frequency.

$$\omega_{n, Dr} \approx Ma \sqrt{C_{N\beta} \frac{\kappa p S b}{2I_{zz}}} \quad (7.10)$$

For the Dutch roll damping ratio, in addition to the above made assumptions for the natural frequency, also the side force due to sideslip is taken to be equal to the yawing moment due to yaw rate. With this considered, the following equation is valid:

$$\lambda_{Dr} = C_{NR} \sqrt{\frac{\rho S b^3}{8C_{N\beta} I_{zz}}} \quad (7.11)$$

As was for the natural frequency, Dutch roll damping ratio is reduced with increasing altitude and moment of inertia about the vertical axis. On the other hand, in this simplification neither the aircraft's speed nor its Mach number is present. Similar to a spring-mass-damper system, the yaw rate damping C_{N_R} acts as a damper and increases the overall value of λ_{Dr} .

There exist several techniques to excite a Dutch roll motion in dynamic stability flight testing. The most commonly used method is the doublet input for which the rudder is moved left and right in phase with the natural motion of the aircraft and then returned to trim position. Afterwards the controls are released and the occurring oscillation recorded. The advantage of this method is that it excites the Dutch roll mode well without exciting the spiral mode. An alternative technique consists of stabilising the aircraft at a steady bank angle and then starting the oscillation with an aileron singlet. Important is that the aileron input is applied as rapidly as possible to roll out of the steady bank angle. As level flight is approached, abrupt aileron is applied in the opposite direction returning the control surface to trim position. This method offers an advantage for aircraft with high inertias often providing more realistic amplitudes than the rudder doublet (**Ward 2006a**, p. 214). Another possible control surface input to excite a Dutch roll motion consists of the so-called rudder kicks method where rudder is depressed and released rapidly and the occurring oscillation observed. The problem with this method is that it tends to excite the spiral mode in addition to the Dutch roll mode. For aircraft with high damping ratio, a Dutch roll oscillation can be excited using a form of the singlet input involving two control inputs simultaneously. First the aeroplane is stabilised in a steady heading sideslip, then both rudder and aileron controls are released at the same time and brought to zero deflection position. This technique is also suitable for aircraft for which a rudder doublet or an aileron singlet does not excite the Dutch roll oscillation adequately.

A complete graphical method for determining the characteristics of all three lateral-directional stability modes from recorded aircraft response data can be found in **Ward 2006a** (p. 223). Due to the complexity of its graphical nature, it is only partly presented in section 7.2.4 of this work. An alternative, simplified data reduction sequence to obtain frequency and damping ratio of recorded Dutch roll mode is given in **Scholz 2005**. It is however more suitable if the oscillation is observed from the cockpit, in particular the motion of the wing tips. After the oscillation is excited, time is measured for which five cycles are observed. Dividing this by 5, one obtains the damped Dutch roll period T_p . Then the Dutch roll frequency equals the reciprocal of T_p multiplied by 2π . To calculate the damping ratio, an assumption is made that the oscillation is subsided when 5 % of the initial amplitude is reached. The resulting mathematical expression to calculate λ_{Dr} is given below in equation (7.12). Due to the simple measurements applied in the above described method, Dutch roll characteristics obtained this way are to be used with discretion.

$$\lambda_{Dr} = -\frac{\ln(0,05)}{2T_p} \quad (7.12)$$

7.2.3 Roll mode

The roll mode describes the aircraft response to a lateral or roll motion, which for a conventional configuration would be excited with an aileron input. The response can be approximated with a decaying exponential function representing the roll rate P . The characteristic time constant in the exponent is usually in the order of one to two seconds. In a simplified, single degree of freedom roll response, due to aileron deflection a disturbing moment about the longitudinal axis rolls the aircraft in direction of the wing with an aileron deflected upwards. As the aeroplane rolls, the spanwise lift distribution changes due to change in effective angle of attack creating a restoring rolling moment, hence roll damping occurs. An illustration of this process is presented below in **Fig. 7.9**. Due to existent roll damping a constant aileron deflection held fixed will only at first yield an accelerating roll rate, for which the acceleration would decrease with time until a steady-state roll rate is achieved.

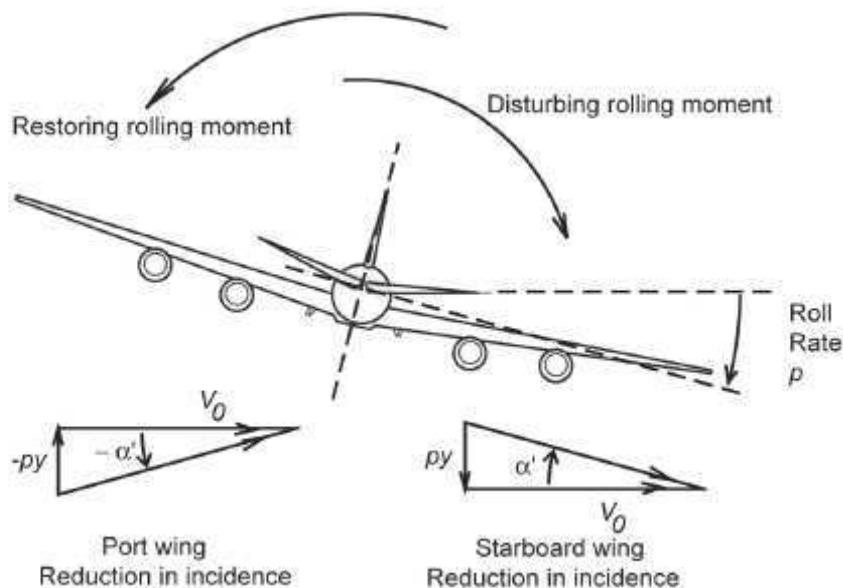


Fig. 7.9 Restoring rolling moment in a roll mode (MIT 2008)

Kimberlin 2003 (p. 325) describes the characteristic time constant for roll mode τ_r , as the time for the roll rate to reach 63,2 % of the steady-state roll rate following a step aileron input. This time constant is not affected by lateral control deflection, hence regardless of the aileron deflection magnitude, τ_r will remain constant. This is true, since with increased aileron deflection, the achievable steady-state roll rate is greater, however the time to reach 63,2 % remains the same. An illustration of this can be found in the above given reference (p. 330). On the other hand, there are a number of parameters which influence the roll rate time constant. These are briefly presented here. First, if the aircraft's moment of inertia in roll is increased, the roll mode time constant increases due to the increased resistance of the aircraft to change in roll. However, since inertia does not affect the speed an object can achieve, the

steady-state roll rate at a constant aileron deflection would not change with increased inertia in roll. Also, if true airspeed is held constant, an increase in altitude would reflect in a greater value of τ_r . This is inversely true for the airspeed. If the aircraft's altitude is held constant, the roll mode time constant would decrease with increasing speed. On the other hand, the steady-state roll rate increases proportional to the true airspeed. This simple theoretical analysis applies only for a rigid model of an aircraft with a simplified, single degree of freedom roll response, while for a real aeroplane with six degrees of freedom additional factors come forward. These include Dutch roll influences, roll coupling and aeroelastic effects. However, more complicated analysis of this lateral-directional mode is beyond the scope of this work, therefore they are not considered here.

The most often used technique to excite the roll mode during flight tests is a step or a singlet aileron input. Once trimmed for a chosen bank angle at the desired flight conditions, the aircraft is rolled to the same bank angle of the opposite roll direction. At this bank angle the aircraft is again stabilised and then rolled back in the other direction using an identical step aileron input of the same magnitude. The initial bank angle is chosen according to the type of aircraft tested. For small, more manoeuvrable aircraft a bank angle of 45° is used. For larger aircraft it is about 30° (**Ward 2006a**, p. 216). To achieve the necessary precision in repeating aileron inputs, temporary stops can be used. Longitudinal controls may be applied to maintain the aircraft's speed during rapid rolls. Normally, roll tests are conducted in both directions, since factors like propellers or turbine rotations often influence the dynamic behaviour of the aircraft differently in each direction.

7.2.4 Lateral-directional stability data reduction

In this last section dedicated to dynamic stability flight testing a graphical method to determine characteristic parameters of lateral-directional modes of motion is presented. This technique applies for analysis of lateral-directional response to a step aileron input, however, due to its complexity and requirement for graphical examples of an aircraft response curve only the basic data reduction sequence is summarised here. The complete process with graphical examples can be found in **Ward 2006a** (p. 223).

After synchronising and correcting recorded data for possible measurement errors, the complete roll rate response to an aileron input is plotted against time. Usually, a roll rate ratio is plotted – recorded roll rate normalised by the initial peak value. For this method linearity is assumed, hence according to the superposition principle for linear systems the response curve can be regarded as the sum of all three lateral-directional modes of motion – spiral mode, roll mode and Dutch roll mode. Mathematically, the function of roll rate with time can be estimated using the expression given in equation (7.13) where each of the three terms

represents the mode of motion corresponding to the index given. The essence of this method is to break down a measured response that contains the components of all lateral-directional modes of motion and then identify characteristic parameters for the individual ones.

$$P(t) = K_s e^{-\frac{t}{\tau_s}} + K_r e^{-\frac{t}{\tau_r}} + K_{Dr} e^{-\lambda_{Dr} \omega_{n,Dr} t} \cos\left(\omega_{n,Dr} \sqrt{1 - \lambda_{Dr}^2} + \psi_{\text{phase}}\right) \quad (7.13)$$

This graphical data reduction is suitable for aircraft with roll and spiral mode responses widely separated in frequency. Using this assumption, one can show that the roll mode will have little influence after the first 3-4 seconds, hence for the remaining time the oscillation is almost entirely composed of spiral mode and Dutch roll mode. The precise data handling is described in the following points:

- First, spiral and Dutch roll mode envelopes are extracted from the measured data by picking out local maximum and minimum points of the response curve and plotting them against time on a semilog paper. To avoid roll mode influences, these points are taken from approx. 3 seconds onward. Smooth curves are drawn through the upper and lower peaks to define the envelope of the spiral mode and Dutch roll mode terms. The spiral mode component is then the numerical average between both curves. On a semilog plot it should be a straight line with K_s being the intersection with the roll rate axis (at zero time). For two random values of this curve, denoted with X_1 and X_2 , and the time difference Δt between them, one can obtain the spiral mode time constant as follows:

$$\tau_s = \frac{\Delta t}{\ln \frac{X_2}{X_1}} \quad (7.14)$$

With the time constant determined, the corresponding time-to-double or respectively time-to-half for a convergent spiral mode equals $0,693\tau_s$. Once all characteristics for the spiral mode response are obtained, one can plot its component using the first term in equation (7.13). The procedure then continues with subtracting the resulting curve from the overall response time history to determine the response containing only Dutch roll and roll mode components.

- For the rest of the data reduction method it is important that both the peaks of the Dutch roll oscillation at later times of the response curve and the combined Dutch roll and roll mode response in the first 3-4 seconds are plotted accurately. The procedure is similar to the one presented above – maximum and minimum points of the Dutch roll oscillation after the first 3-4 seconds are extracted and plotted on semilog paper. This should yield two

parallel straight lines, one for the local maxima and one for the local minima. The Dutch roll damping ratio λ_{Dr} is defined by the slope of either of these lines. The damped period T_p is estimated directly from the response plot after the first 3-4 seconds. With both these parameters known, one can utilise them to reconstruct the Dutch roll component in the first 3-4 seconds. By subtracting this graphically from the combined roll mode and Dutch roll mode response curve, one can obtain the roll mode component.

- By plotting the roll mode component of the response curve on semilog paper, one can determine the roll mode time constant τ_r , defined in the previous section of this chapter as the time for which the roll rate reaches 63,2 % of the steady-state roll rate. As was for the spiral mode, in a semilog plot the roll mode component is also a line, whose intersection with the vertical axis at zero time yields the constant K_r . At a normalised roll rate value equal to $(1 - 0,632)K_r$, a horizontal line is drawn and its intersection with the roll mode line yields the time constant. Alternatively, τ_r can be calculated from equation (7.15) by taking two amplitude values of roll rate, P_1 and P_2 , and the corresponding time increment Δt . In the example presented by **Ward 2006a** (p. 228) both solutions yield the same result.

$$\tau_r = \frac{\Delta t}{\ln \frac{P_2}{P_1}} \quad (7.15)$$

The above described graphical method to obtain characteristic parameters for spiral mode, roll mode and Dutch roll mode from a lateral-directional response to a step aileron input produces good results only for conventional aircraft with a Dutch roll damping ratio less than approx. 0,3. The condition for spiral and roll modes widely separated in frequency is also necessary to be able to exclude the roll mode in the first step of the data reduction. The roll mode time constant τ_r is typically about 1 second and the time needed for the roll mode to reach approx. 95 % of its final value is usually $3\tau_r$ after the input is returned, hence the 3-4 seconds boundary is in most cases a safe approximation.

8 Summary

Various flight test techniques and methods for data reduction to determine essential aerodynamic and flight mechanical parameters were presented in this work as part of a subscale flight testing project carried out at Linköping University. Where possible, these were adjusted in accordance with the available instrumentation of the *Raven*. This last chapter gives a brief summary of the topics discussed in the course of the thesis and partly describes the author's personal opinion on these in form of conclusions and recommendations.

First of all, two in-flight methods for position error calibration with the appropriate data reduction sequence were presented thoroughly – one using a true airspeed approach and one with an altitude correction approach. The first one, the speed course method, presents a relative simple technique for Pitot-static system position error calibration with only basic instrumentation required. The obtained results lack the accuracy of more sophisticated methods and are highly dependent on the precision with which the test procedure is executed. Important parameters to be held constant are the aircraft speed and heading. With no ASI and no heading indications, the *Raven* pilot must rely strictly on visual contact from the ground and on indications coming from the telemetry system to maintain these parameters constant. A variation of this method can be made utilising GPS ground speed measurements. However, this variation applies only for the data reduction process and does not improve the existing weaknesses in the test procedure. A similar method utilising the so-called “cloverleaf technique” presents an alternative solution, however, it also requires flying at constant heading. The second method, whose data reduction was developed by the author using ISA equations for altitude corrections, assumes accurate GPS altitude data, which for commercially available devices is not the case. The use of differential GPS with a ground station could improve the accuracy of this method, however, due to increased costs such application is not considered at the time being. Taking into account the aircraft dimensions and the position of the Pitot tube on a small nose boom, there is the possibility that for both calibration methods the error made by imprecise execution of the test procedure might be greater than the one due to the presence of the sensors in the aircraft's pressure field. This statement is to be verified with data acquired from flight tests.

Regarding the turbine thrust model, only general conclusions can be drawn due to lack of data for verification. The progression of the obtained thrust functions with airspeed matches the information provided by AMT, however, such thrust curves are not typical for a full-size transport aircraft jet engine. At first thrust decreases with increasing airspeed and after a certain minimum value between 75 and 100 m/s it starts increasing, for which no meaningful explanation was found. Since the linear scaling method, on which the thrust model is based, uses data from different manufacturers, the resulting thrust curves will most likely be inaccurate. These however can be regarded as basic information on FS-70 Typhoon thrust characteristics, for which more thorough investigations are to be conducted in the future.

Since the determination of lift and drag coefficients with changes in angle of attack has high priority in the first flight tests to be conducted, significant effort was devoted to investigating suitable flight test methods and adjusting them to the available equipment of the *Raven*. As a result, two methods were presented – a steady level flight method, where lift and drag functions with angle of attack can be directly determined using respectively weight and thrust indications, and a technique to obtain the aircraft's drag polar from series of steady glides. In the first one, the biggest disadvantage concerns drag determination, since as described above, the accuracy of the existing thrust model is questionable at the time being. Another downside is, that at high angles of attack the thrust vector cannot be assumed parallel to the flight path anymore, introducing a small thrust force component in lift direction. On the other hand, the steady glide method, utilised in flight test laboratory exercises at Hamburg University of Applied Sciences, yields satisfactory results for the aircraft's drag polar. It does not however make any statements about the functions of lift and drag with AOA. Therefore, a combination of these two methods can be used to neutralise the disadvantages of the individual ones. Since actual aircraft weight can be measured accurately using fuel flow rate indications, a function of lift with angle of attack can be obtained with a steady level flight method, and then with the determined drag polar from series of steady glides one can calculate drag coefficients at tested AOA from the first method and obtain a function of C_D with α .

Normally, stall speed flight tests do not present any complexity, neither in piloting skills nor in data reduction. They can however be hazardous if nominal altitude is not chosen appropriately and test procedures are not planned with the necessary caution prior to flight testing. Important is that a small deceleration rate is applied when increasing the aircraft angle of attack. Possible errors due to large flow inclinations at approaching stall condition may occur for static pressure measurements falsifying results for calibrated airspeed.

The flight test method presented for determination of neutral point and function of pitching moment coefficient with AOA is straightforward and does not require any specific instrumentation, or complex data reduction sequence. Important is that tests are performed at two different CG positions with the aircraft trimmed at a range of various airspeeds. Lift coefficients are then determined using actual weight information and calculated calibrated airspeeds. On the other hand, flight tests methods for determination of aircraft performance in sideslip require more complicated piloting techniques. Since the aircraft is piloted from the ground, no reference points on the horizon can be used to stabilise that aircraft at a steady heading. Also, control inputs in a sideslip are cross-coupled which can be unnatural for the pilot to perform.

Finally, the presented dynamic stability flight tests are not adjusted to the available instrumentation of the *Raven*. Most of them require precise performance of the characteristic control inputs, which also consists of returning these to trim position afterwards. Hence, if the trim position of the controls cannot be measured, as is the case for the *Raven* aircraft at this point, an accurate execution of the manoeuvre will be more difficult for the pilot to perform.

For such measurements for example, real-time indications of control surface deflections can be of significant assistance to the pilot. Another downside of the presented dynamic stability tests is that most of the data reduction methods given are simplified and yield only estimated values for the characteristic parameters. This is especially true for lateral-directional dynamic stability modes, where all three modes of motion are coupled making data reduction more complicated.

In general, the information presented here gives a purely theoretical approach of the existing problem with no acquired flight test data to back up the proposed methods and verify their accuracy. Since this work presents the first approach of flight test planning with the *Raven* aircraft, further adjustments would probably be needed when actual tests are performed in order to improve the practical application of the methods described here.

References

- AC23-8B 2003** U.S. DEPARTMENT OF TRANSPORTATION, FEDERAL AVIATION ADMINISTRATION: *Advisory Circular, AC23, Flight Test Guide for Certification of Part 23 Airplanes*
- AMT 2008** URL: <http://www.amtjets.com/> (2008-08-10)
- Anderson 1984** ANDERSON, J.D.: *Fundamentals of Aerodynamics*. New York : McGraw-Hill, 1984
- FunSonic 2008** URL: <http://www.funsonic.de/> (2008-08-10)
- JAR-1 1996** JOINT AVIATION AUTHORITIES: *Joint Aviation Requirements, JAR-1, Definitions and Abbreviations*
- Kimberlin 2003** KIMBERLIN, Ralph D.: *Flight testing of Fixed-Wing Aircraft*, AIAA Education Series. Reston, VA : American Institute for Aeronautics and Astronautics, 2003
- Lundström 2008** LUNDSTRÖM, David; AMADORI, Kristian: *Raven – A Subscale Radio Controlled Business Jet Demonstrator*. Linköping, University, Department of Mechanical Engineering, paper, 2008
- Mair 1992** MAIR, W. Austyn; BIRDSALL, David L.: *Aircraft Performance*, Cambridge Aerospace Series. Cambridge, UK : Cambridge University Press, 1992
- Meins 2001** MEINS, Oliver: *Bestimmen von Flugleistungen und -eigenschaften aus Flugversuchsdaten der Muster Cessna 172 und Piper Archer*. Hamburg, Hochschule für Angewandte Wissenschaften, Department Fahrzeugtechnik und Flugzeugbau, theoretische Arbeit, 2001
- MIT 2008** URL: <http://ocw.mit.edu/NR/rdonlyres/Aeronautics-and-Astronautics/16-61Aerospace-DynamicsSpring2003/B97E0200-2B1C-45A9-96AD-3CED05AE7233/0/lecture18.pdf>
- NASA 1975** TALAY, Theodore: *Introduction to the Aerodynamics of Flight*. Washington, D.C. : NASA Langley Research Center, 1975

- NavAir 1992** U.S. NAVAL TEST PILOT SCHOOL: *Fixed Wing Performance : Flight Test Manual, USNTPS-FTM-No.108*. Patuxent River, MD, 1992. – URL: http://www.usntpsalumni.org/html/usntps-ftm-no_108.html (2008-08-21)
- NavAir 1997** U.S. NAVAL TEST PILOT SCHOOL: *Fixed Wing Stability and Control : Theory and Flight Test Techniques, USNTPS-FTM-No.103*. Patuxent River, MD, 1997. – URL: http://www.usntpsalumni.org/html/usntps-ftm-no_103.html (2008-08-21)
- Roskam 1997** ROSKAM, Jan; LAN, C.T.: *Airplane Aerodynamics and Performance*. Lawrence, KS : Design, Analysis and Research Corporation, 1997
- Scholz 2000** URL: <http://www.fzt.haw-hamburg.de/pers/Scholz/materialFM1/GenericEnginePerformance.pdf> (2008-08-15)
- Scholz 2002** SCHOLZ, Dieter: *Unterlagen zur Vorlesung: Flugmechanik 1*. Hamburg, Hochschule für Angewandte Wissenschaften, Department Fahrzeugtechnik und Flugzeugbau, lecture notes, 2002
- Scholz 2005** URL: <http://www.fzt.haw-hamburg.de/pers/Scholz/materialFP/Musterrechnung.xls> (2008-08-15)
- SpaceAge 2008** URL: <http://www.spaceagecontrol.com/adpspec.htm> (2008-08-10)
- Ward 2006a** WARD, Don; STRGANAC, Thomas; NIEWOEHNER, Rob: *Introduction to Flight Test Engineering*. Vol. I. 3rd Ed. Dubuque, IA : Kendall/Hunt Publishing Company, 2006
- Ward 2006b** WARD, Don; SCHWEIKHARD, William G.: *Flight Test Principles and Practices*. Lawrence, KS : The University of Kansas Continuing Education, 2006
- Young 2001** YOUNG, Trevor: *Flight Mechanics*. Limerick, University, Department of Mechanical and Aeronautical Engineering, lecture notes, 2001
- Zingel 1999** ZINGEL, Hartmut: *Gasdynamik*. Hamburg, Hochschule für Angewandte Wissenschaften, Department Fahrzeugtechnik und Flugzeugbau, lecture notes, 1999

Appendix A

Charts and tables

International Standard Atmosphere

Table A.1 International Standard Atmosphere values

Geopotential height		Barometric pressure		Temperature			Density		Speed of sound
H		P	δ	T	ϑ	θ	ρ	σ	a
m	ft	Pa	-	K	°C	-	kg/m ³	-	m/s
-200	-656,168	103751	1,02394	289,45	16,3	1,00451	1,2487	1,01934	341,061
-150	-492,126	103140	1,01791	289,13	16,0	1,00338	1,2427	1,01448	340,869
-100	-328,084	102532	1,01191	288,80	15,7	1,00226	1,2368	1,00964	340,678
-50	-164,042	101927	1,00594	288,48	15,3	1,00113	1,2309	1,00481	340,486
0	0	101325	1	288,15	15,0	1	1,2250	1	340,294
50	164,042	100726	0,99409	287,83	14,7	0,99887	1,2191	0,99521	340,102
100	328,084	100129	0,98820	287,50	14,4	0,99774	1,2133	0,99043	339,910
150	492,126	99536	0,98234	287,18	14,0	0,99662	1,2075	0,98568	339,718
200	656,168	98945	0,97651	286,85	13,7	0,99549	1,2017	0,98094	339,526
250	820,210	98358	0,97071	286,53	13,4	0,99436	1,1959	0,97622	339,333
300	984,252	97773	0,96494	286,20	13,1	0,99323	1,1901	0,97151	339,141
350	1148,294	97190	0,95920	285,88	12,7	0,99210	1,1844	0,96683	338,948
400	1312,336	96611	0,95348	285,55	12,4	0,99098	1,1786	0,96216	338,755
450	1476,378	96035	0,94779	285,23	12,1	0,98985	1,1729	0,95751	338,563
500	1640,420	95461	0,94213	284,90	11,8	0,98872	1,1673	0,95287	338,370
550	1804,462	94890	0,93649	284,58	11,4	0,98759	1,1616	0,94826	338,177
600	1968,504	94322	0,93088	284,25	11,1	0,98647	1,1560	0,94365	337,983
650	2132,546	93756	0,92530	283,93	10,8	0,98534	1,1504	0,93907	337,790
700	2296,588	93194	0,91975	283,60	10,5	0,98421	1,1448	0,93451	337,597
750	2460,630	92634	0,91422	283,28	10,1	0,98308	1,1392	0,92996	337,403
800	2624,672	92076	0,90872	282,95	9,8	0,98195	1,1336	0,92542	337,210
850	2788,714	91522	0,90325	282,63	9,5	0,98083	1,1281	0,92091	337,016
900	2952,756	90970	0,89780	282,30	9,1	0,97970	1,1226	0,91641	336,822
950	3116,798	90421	0,89239	281,98	8,8	0,97857	1,1171	0,91193	336,628
1000	3280,840	89875	0,88699	281,65	8,5	0,97744	1,1116	0,90746	336,434
1050	3444,882	89331	0,88163	281,33	8,2	0,97631	1,1062	0,90302	336,240
1100	3608,924	88790	0,87629	281,00	7,9	0,97519	1,1008	0,89858	336,046
1150	3772,966	88251	0,87097	280,68	7,5	0,97406	1,0954	0,89417	335,851
1200	3937,008	87716	0,86569	280,35	7,2	0,97293	1,0900	0,88977	335,657
1250	4101,050	87182	0,86042	280,03	6,9	0,97180	1,0846	0,88539	335,462
1300	4265,092	86652	0,85519	279,70	6,6	0,97067	1,0793	0,88102	335,267
1350	4429,134	86124	0,84998	279,38	6,2	0,96955	1,0739	0,87668	335,073
1400	4593,176	85599	0,84479	279,05	5,9	0,96842	1,0686	0,87234	334,878
1450	4757,218	85076	0,83964	278,73	5,6	0,96729	1,0633	0,86803	334,683
1500	4921,260	84556	0,83450	278,40	5,3	0,96616	1,0581	0,86373	334,487
1550	5085,302	84038	0,82940	278,08	4,9	0,96504	1,0528	0,85945	334,292
1600	5249,344	83524	0,82431	277,75	4,6	0,96391	1,0476	0,85518	334,097

Compressibility correction

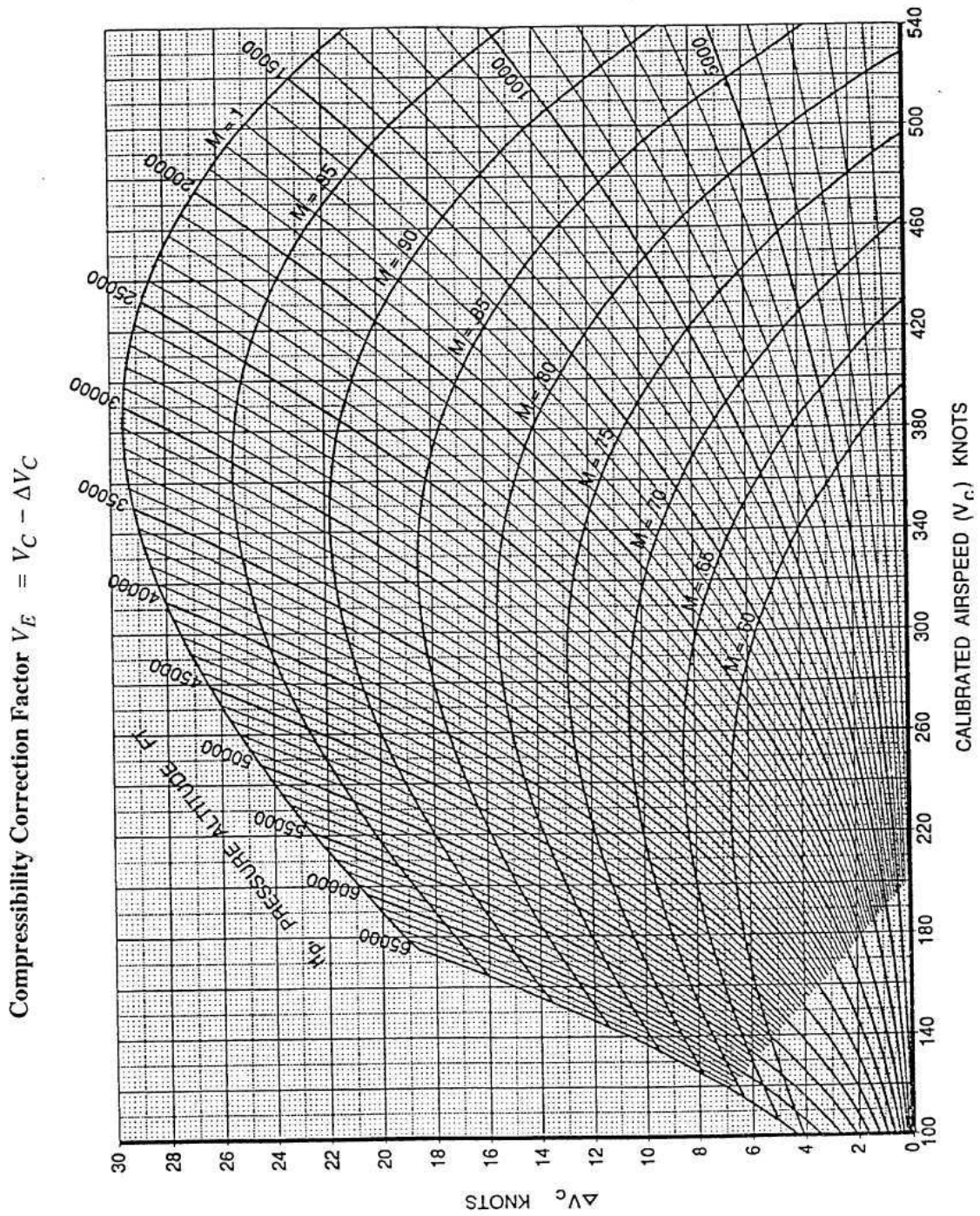


Fig. A.1 Compressibility correction factor (Young 2001)

Atmospheric air temperature determination

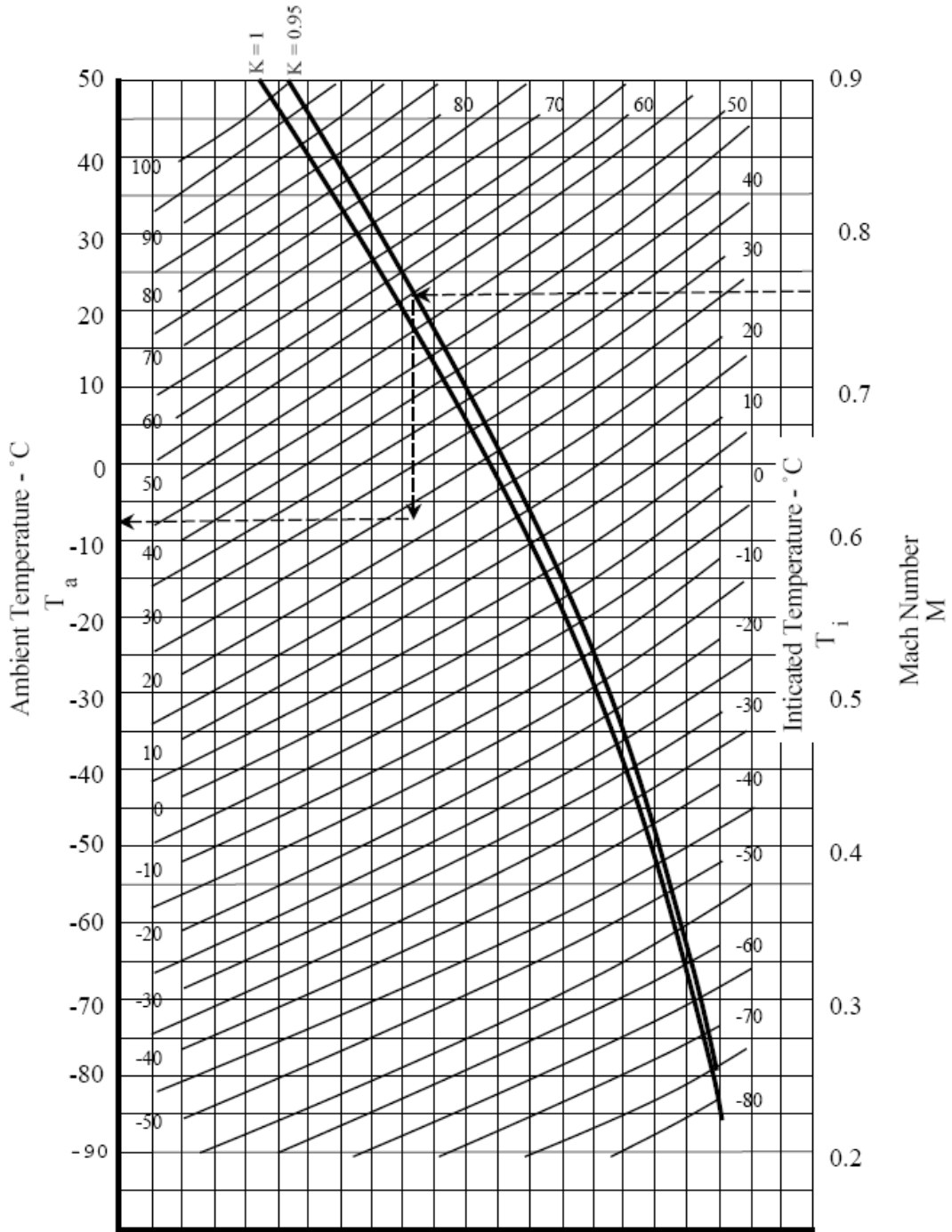


Fig. A.2 Atmospheric temperature measurement (NavAir 1992)

Appendix B

Altitude and airspeed position error

In the following an approximation relating altitude and airspeed position error is derived according to **Ward 2006a**.

The change of pressure with geopotential altitude is given by the hydrostatic equation:

$$dp = -\rho g_0 dH$$

For small errors, such as position error, dp is assumed to be Δp_p and correspondingly dH becomes the altitude static position error correction Δh_{pc} . With standard day conditions considered, the hydrostatic equation can be written as:

$$\frac{\Delta p_p}{\Delta h_{pc}} = \rho_0 \sigma_{\text{std}} g_0 \quad (\text{B.1})$$

For an isentropic flow (no errors in pressure measurement considered) the following relationship is valid:

$$\frac{p_T - p}{p} = \left(1 + \frac{\kappa - 1}{2} \cdot \frac{V^2}{a^2} \right)^{\frac{\kappa}{\kappa - 1}} - 1$$

Solving for the difference of total and static pressure given as the impact pressure q_c , and using the definition for the calibrated airspeed yields

$$q_c = p_0 \left(1 + \frac{\kappa - 1}{2} \cdot \frac{V_c^2}{a_0^2} \right)^{\frac{\kappa}{\kappa - 1}} - p_0$$

and for the instrument corrected airspeed V_{ic} , $q_{c,ic}$ replaces q_c :

$$q_{c,ic} = p_0 \left(1 + \frac{\kappa - 1}{2} \cdot \frac{V_{ic}^2}{a_0^2} \right)^{\frac{\kappa}{\kappa - 1}} - p_0$$

Differentiating this equation yields:

$$\frac{dq_{c,ic}}{dV_{ic}} = \frac{\kappa p_0 V_{ic}}{a_0^2} \left[1 + \frac{(\kappa - 1)V_{ic}^2}{2a_0^2} \right]^{\frac{1}{\kappa - 1}}$$

Since the total pressure measurement is regarded free of position error and for small errors the differentials can be approximated with finite differences, the following correlations are valid:

$$\begin{aligned} dq_{c,ic} &\approx -\Delta p_p \\ dV_{ic} &\approx -\Delta V_{pc} \end{aligned}$$

Substituting the finite differences for the differentials above yields

$$\frac{\Delta p_p}{\Delta V_{pc}} \approx \frac{\kappa p_0 V_{ic}}{a_0^2} \left[1 + \frac{(\kappa - 1)V_{ic}^2}{2a_0^2} \right]^{\frac{1}{\kappa - 1}} \quad (\text{B.2})$$

Finally, dividing equation (B.2) by (B.1) and using the formula for the speed of sound gives an approximation for the ratio of altitude and airspeed position error corrections:

$$\frac{\Delta h_{pc}}{\Delta V_{pc}} \approx \frac{V_{ic}}{\sigma_{\text{std}} g_0} \left[1 + \frac{\kappa - 1}{2} \cdot \left(\frac{V_{ic}}{a_0} \right)^2 \right]^{\frac{1}{\kappa - 1}}$$

Fig. B.1 shows a plot of this ratio as a function of instrument corrected airspeed for different altitudes up to 4000 m. The altitude dependency is given by the value of σ_{std} calculated from the ISA equations.

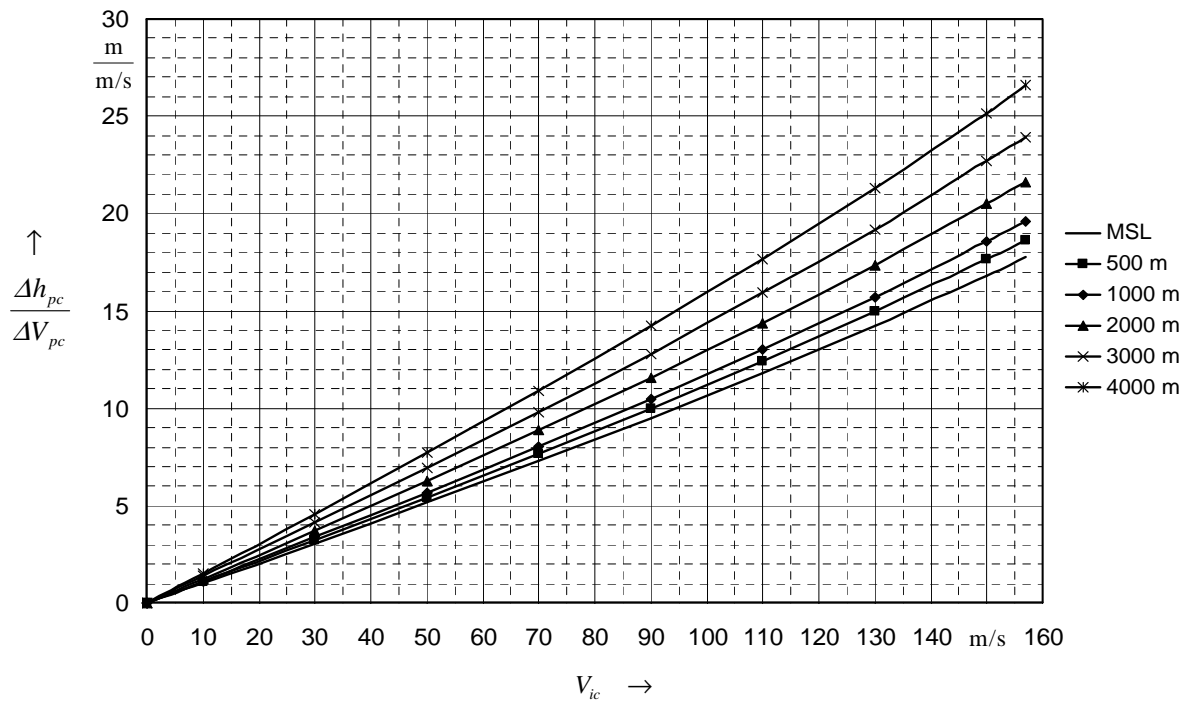


Fig. B.1 Ratio of altitude to airspeed position error correction

Appendix C

FS-70 Typhoon manufacturer data

Table C.1 FS-70 Typhoon static thrust and engine speed

Engine speed [1/min]	Static thrust [kg]	Static thrust [lbf]
50 000	0,35	0,77
60 000	0,58	1,28
70 000	0,87	1,92
80 000	1,22	2,69
90 000	1,63	3,59
100 000	2,10	4,63
110 000	2,63	5,80
120 000	3,22	7,10
130 000	3,87	8,53
140 000	4,58	10,10
150 000	5,35	11,80
160 000	6,18	13,62
170 000	7,07	15,59

* Thrust $\pm 5\%$ at 1013 mbar, 15 °C

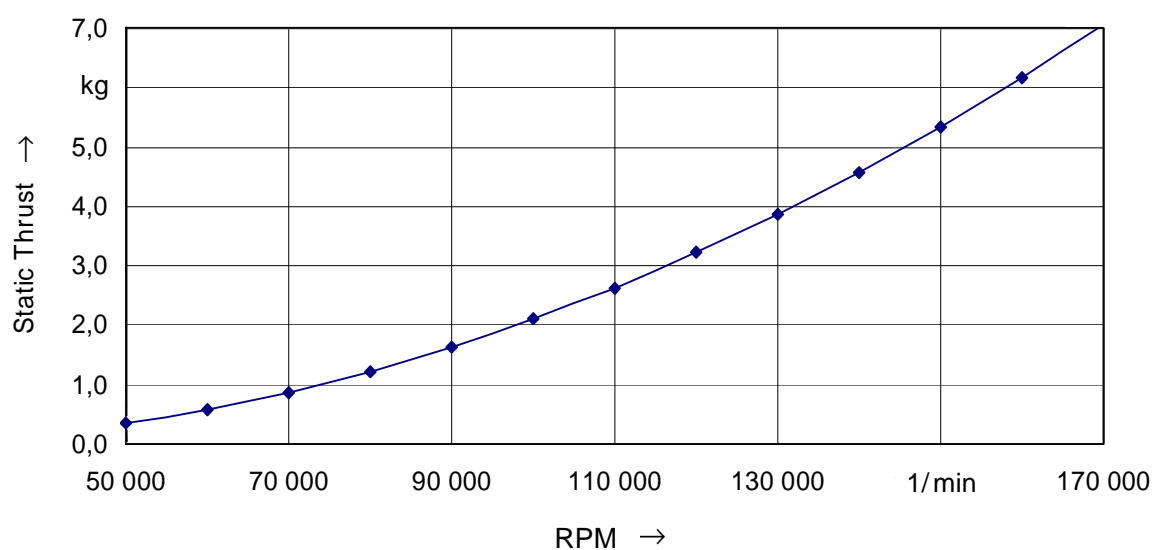


Fig. C.1 FS-70 Typhoon static thrust versus engine speed at MSL

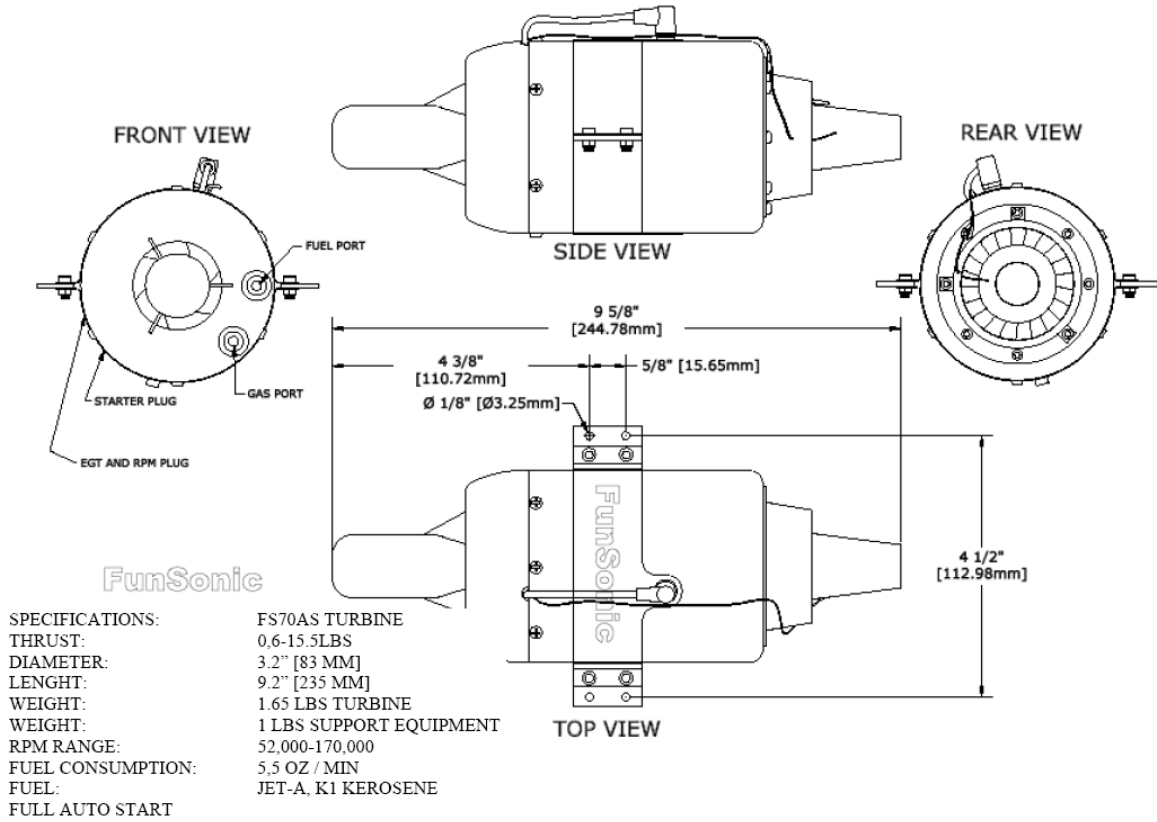


Fig. C.2 FS-70 Typhoon – three-view drawing and main parameters

Appendix D

Example of total thrust calculation

As already explained in Chapter 5, one way to utilise the thrust model for random values of airspeed, altitude and engine speed requires mathematical manipulation. The precise calculation sequence is presented here, for which the aircraft's altitude is assumed to be 400 m, its airspeed – 110 m/s, and the engine speed – 75 %. First, the total static thrust value at 75 % is determined using equation (5.1) as follows:

$$2(0,00850527 \cdot 75^2 - 0,16677 \cdot 75 + 0,981) = 72,63 \text{ N}$$

Next, using the Olympus HP read-out values, one can obtain total thrust functions with airspeed for MSL, 10 000 ft and 16 000 ft by means of linear scaling, as shown in Chapter 5. The calculated total thrust values are given in the following table for airspeed steps of 25 m/s:

Table D.1 Total thrust values for an example engine speed of 75 %

Airspeed	Total thrust at MSL		Total thrust at 10 000 ft		Total thrust at 16 000 ft	
V [m/s]	F_T [N]		F_T [N]		F_T [N]	
–	Typhoon $n = 75 \%$	Olympus HP $n = 100 \%$	Typhoon $n = 75 \%$	Olympus HP $n = 100 \%$	Typhoon $n = 75 \%$	Olympus HP $n = 100 \%$
0	72,63	458	59,47	375	52,17	329
25	69,30	437	57,72	364	50,75	320
50	67,71	427	56,14	354	49,32	311
75	66,92	422	55,82	352	49,00	309
100	66,92	422	55,82	352	49,00	309
125	67,56	426	56,30	355	49,64	313
150	69,78	440	57,88	365	50,90	321
175	72,16	455	59,94	378	52,81	333
200	75,33	475	62,64	395	55,35	349

Since the aircraft's speed of 110 m/s was intentionally chosen not to match the steps of V given above, total thrust at this airspeed should be either obtained by plotting these functions and then graphically determine F_T , or by using "Trendline" to acquire mathematical approximations and then substitute the airspeed in them. To retain the numerical nature of this example, the second method is adopted here. The equations and the appropriate values of total thrust at 110 m/s obtained this way are presented below in **Table D.2**. One can see that at 0 m/s the results of these mathematical approximations do not match precisely the values given

in the table above, however, the deviation in all cases is less than 0,5 %, therefore the calculation error can be considered negligibly small.

Table D.2 Equations relating airspeed and total thrust at 75 % engine speed

Altitude	Equation	F_T at $V = 110$ m/s
MSL	$F_T = 0,0007V^2 - 0,1254V + 72,331$	67,01 N
10 000 ft	$F_T = 0,0005V^2 - 0,0912V + 59,529$	55,55 N
16 000 ft	$F_T = 0,0005V^2 - 0,0807V + 52,276$	49,45 N

Next, using the three calculated values at 110 m/s, one can determine a function of total thrust with altitude by applying “Trendline” again. Since in this case its progression is approximately linear, a second-order polynomial expression would yield the same result as a linear function. Therefore, for this example such function is adopted and presented below:

$$F_T(H) = -0,0011H + 66,888 \quad (\text{D.1})$$

Since the value of H in equation (5.2) is not given in SI units, one should first convert the altitude of 400 m as follows:

$$\begin{aligned} H &= \frac{400}{0,3048} \text{ ft} \\ &= 1312,34 \text{ ft} \end{aligned}$$

Finally, substituting this in equation (D.1) yields the desired value of total thrust:

$$\begin{aligned} F_T(H = 1312,34 \text{ ft}) &= -0,0011 \cdot 1312,34 + 66,888 \\ &= 65,44 \text{ N} \end{aligned}$$

The above described mathematical manipulation with MS Excel offers a relative simple way to obtain total thrust from known flight test data with no need for plotting and reading-out values. The errors made by applying mathematical approximations with “Trendline” can be considered rather insignificant with the overall quality of the thrust model. The accuracy of the results can also be manipulated by changing the order of these approximations depending on the acquired functions of thrust with airspeed and altitude.